2012

Advanced materials for flexible lithium rechargeable batteries

Lukman Noerochim
University of Wollongong

ADVANCED MATERIALS FOR FLEXIBLE LITHIUM RECHARGEABLE BATTERIES

A thesis submitted in fulfilment of requirements

for the award of the degree of

DOCTOR OF PHILOSOPHY

from

UNIVERSITY OF WOLLONGONG

by

LUKMAN NOEROCHIM

B.Sc. (Hons.), M.Sc.

INSTITUTE FOR SUPERCONDUCTING AND ELECTRONIC MATERIALS

FACULTY OF ENGINEERING

September 2012

Declaration

I, Lukman Noerochim, declare that the work presented in this thesis is original and was carried out at the Institute for Superconducting and Electronic Materials, Faculty of Engineering, University of Wollongong, New South Wales, Australia. This thesis is wholly my own work and contains no work previously published or written by another person, unless otherwise acknowledged and referenced. This work is original and has not been submitted to qualify for any other degree elsewhere.

Lukman Noerochim

27 September 2012

Acknowledgements

I thank to Allah SWT for His blessing and mercy.

It is my great pleasure to acknowledge the valuable assistance that I have received from the people of the University of Wollongong, Australia, during the course of my doctoral studies.

I would like to express my deepest gratitude to my principal supervisor, Prof. Hua Kun Liu and co-supervisor, Dr. Jiazhao Wang for their encouragement, understanding, invaluable advice and constant support during my study at University of Wollongong (UOW).

I would like to express my deepest appreciation to Prof. Shi Xue Dou, director of the Institute for Superconducting and Electronic Materials (ISEM) and Prof. Gordon Wallace, director of the ARC Centre of Excellence for Electromaterials Science (ACES), for providing me with appropriate facilities and expertise during the course of my studies.

I would like to thank ISEM, ACES and the University of Wollongong, for financial support from the Australian Research Council (ARC) under an ARC centre of Excellence Program (EC 0561616) and an ARC Discovery Project (DP 0987805), by means of Matching Scholarship and International Postgraduate Tuition Award.

Technical assistance from people at UOW, such as Dr. David Wexler (TEM), Mr. Darren Attard (SEM, FE-SEM), Dr. Konstantin Konstantinov (TGA/DSC, BET), Dr. Shulei Chou (Electrochemical measurements), Mr. Ron Kinnell and Mr. Robert Morgan (mechanical assistance), A/Prof. Peter Innis (Raman, FT-IR) and Dr.

Germanas Peleckis (XRD) is also highly appreciated. My special thanks to Dr. Tania Silver for critical reading of the manuscript and thesis as well.

I would like to thank Dr. Jun Chen, Intelligent Polymer Research Institute (IPRI), University of Wollongong for his collaborative research work.

I also wish to thank Prof. Zaiping Guo, Dr. Dongqi Shi, Dr. Guodong Du, Dr. Nurul Idris, Dr. Moh. Faiz Hasan, Mr. Chao Zhong, Ms. Lu Lin, Ms. Xuanwen Gao, Ms. Yi Shi, Ms. Xin Liang, Mr. Zhijia Zhang, Ms. Yun Xiao, Mr. Jiantie Xu, Mr. Ivan Seng, Mr. Chaofeng Zhang, Mr. Moh. Ihsan, and Mr. Faiz for helping me and sharing knowledge with me during of this research.

Finally, I would like to thank my parents, my sister, my parents in law, brothers and sisters in law for their continue support and love, which translates into the strength and guidance path for me during my PhD studies. My heartiest thanks go to my wonderful wife, Mrs. Alizatul Jamilah, who is always support me even though at long distance and provides a lot of inspirations to achieve my PhD degree and all my beloved kids, Abidah Al Mughniyah, Nurul Azizah, Abidah Al Mustaniroh and Ahmad Noerochim. You all are my inspiration.

Table of Contents

Abstract

Lithium-ion batteries are essential to modern life as power sources for a wide spectrum of devices ranging from portable electronic devices to electric automobiles. There is currently an enormous ongoing research effort aimed at developing ultra-thin, flexible, and soft batteries to cater for the bendable modern devices. Although there is a high demand for flexible lithium-ion batteries, these must satisfy stringent requirements, including larger reversible capacity, smaller size, lighter weight, mechanical stability, and long cycle life. Advanced nanotechnology of materials provides the main solutions to these issues. Improved battery performance depends on the development of materials for the various battery components, with the key aspect of improving the performance of the active materials used to fabricate the anode and cathode. The use of nanostructured and conductive composite materials is designed to enhance both ion transport and electron transport by shortening the diffusion lengths of ions and increasing the conductivity within the whole electrode. In this doctoral study, several nanostructured and conductive composite materials were examined and characterized for possible application as electrodes for flexible lithium-ion batteries. With these aims, nanocrystalline SnO_2-coated multiwall carbon nanotubes, free-standing SnO_2 − single wall carbon nanotubes, polypyrrole-coated V_2O_5 nanowires, and stacked graphene with MoO_3 nanobelts were investigated.

SnO_2-coated multiwall carbon nanotube (MWCNT) nanocomposites were synthesized by a facile hydrothermal method. Field emission scanning electron microscope (FE-SEM) images show that deposition of SnO_2 onto the surfaces of the MWCNTs takes place in some selected sites, while in the composites with higher content of SnO_2, more SnO_2 particles are deposited on the surfaces of MWCNTs.

The SnO_2/MWCNT composites, when combined with carboxymethyl cellulose (CMC) as a binder, show excellent cyclic retention, with the high specific capacity of 473 mAh g^{-1} beyond 100 cycles, much greater than that of the bare SnO_2 which was also prepared by the hydrothermal method in the absence of MWCNTs. The enhanced capacity retention could be mainly attributed to good dispersion of the tin dioxide particles in the matrix of MWCNTs, which protected the particles from agglomeration during the cycling process. Furthermore, the usage of CMC as a binder is responsible for the low cost and environmental friendliness of the whole electrode fabrication process.

Free-standing single-walled carbon nanotube/SnO_2 (SWCNT/SnO_2) anode paper was prepared by vacuum filtration of SWCNT/SnO_2 hybrid material which was synthesized by the polyol method. From FE-SEM and transmission electron microscope (TEM) images, the CNTs form a three-dimensional nanoporous network, with the ultra-fine SnO_2 nanoparticles, which had crystallite sizes of less than 5 nm, distributed predominately as groups of nanoparticles on the surfaces of single walled CNT bundles. Electrochemical measurements demonstrated that the anode paper with 34 wt.% SnO_2 had excellent cyclic retention, with the high specific capacity of 454 mAh g^{-1} beyond 100 cycles at a current density of 25 mA g^{-1}, much higher than that of the corresponding pristine CNT paper. The SWCNTs could act as a flexible mechanical support for strain release, as well as offering an efficient electrically conducting channel, while the nanosized SnO_2 provides the high capacity. The SWCNT/SnO_2 flexible electrodes can be bent to extremely small radii of curvature and still function well, despite a marginal decrease in the conductivity of the cell. The electrochemical response is maintained in the initial and subsequent cycling.

Such capabilities demonstrate that this model holds great promise for applications requiring flexible and bendable Li-ion batteries.

Highly flexible, paper-like, free-standing V_2O_5 and V_2O_5-polypyrrole (PPy) films were prepared via the vacuum filtration method. The films are soft, lightweight, and mechanically robust. FE-SEM images of the pristine V_2O_5 film show straight nanowires ~80-120 nm in diameter and several microns in length, resulting in an aspect ratio of ~10^2-10^3. On the other hand, the V_2O_5-PPy film shows similar morphology to the V_2O_5 film, with the PPy uniformly deposited throughout entire lengths of nanowires in irregular or spherical shapes. The electrochemical performance of the free-standing pure V_2O_5 electrode was improved by incorporating conducting polypyrrole. A bendable cell with a novel design was fabricated, consisting of a free-standing V_2O_5-PPy cathode film, gel electrolyte, and a lithium foil anode. The cell was tested under repeated bending conditions for several cycles. The results show that the battery performance of the repeatedly bent cell was similar to that of a comparable conventional cell.

Highly flexible, binder-free, MoO_3 nanobelt/graphene film electrode was prepared by a two-step microwave hydrothermal method. Graphene is first prepared by an ultra-fast microwave hydrothermal method and then mixed with MoO_3 solution to synthesize the MoO_3 nanobelt/graphene composite, which exhibits the combination of stacked graphene sheets and uniform MoO_3 nanobelts with widths of 200-500 nm and lengths of 5-10 μm. In the charge-discharge measurements, the as-synthesized MoO_3/graphene hybrid materials demonstrated excellent rate capability, large capacity, and good cycling stability compared to the pure MoO_3 film. An initial

discharge capacity of 291 mAh g^{-1} can be obtained at 100 mA g^{-1}, with a capacity of 172 mAh g^{-1} retained after 100 cycles. The results show that the MoO_3/graphene designed in this study can be used as a free-standing cathode material in rechargeable and bendable lithium batteries.

Nomenclature

List of Abbreviations

Abbreviations	Full name
1D	One-dimensional
2D	Two-dimensional
3D	Three-dimensional
a.u.	Arbitrary unit
AB	Acetylene black
AIIM	Australian Institute for Innovative Materials
BS	Backscattered
BSE	Back-scattered electrons
CCD	Charge-coupled device
cm	Centimeter
CMC	Sodium carboxymethyl cellulose
CNT	Carbon nanotube
CPE	Constant phase-angle element
CV	Cyclic voltammetry
CVD	Chemical vapour deposition
DEC	Diethyl carbonate
DEG	Diethylene glycol
DMC	Dimethyl carbonate
DSC	Differential scanning calorimetry
EC	Ethylene carbonate
EDX/EDS	Energy dispersive X-ray spectroscopy

Abbreviations	Full name
EIS	Electrochemical impedance spectroscopy
EV	Electric vehicle
FE-SEM	Field emission scanning electron microscopy
FWHM	Full-width at half maximum
GIC	Graphite intercalation compounds
GNS	Graphene nanosheet
GPE	Gel polymer electrolyte
HEV	Hybrid electric vehicle
HRTEM	High resolution transmission electron microscopy
IPRI	Intelligent Polymer Research Institute
ISEM	Institute for Superconducting and Electronic Materials
JCPDS	Joint committee on powder diffraction standards
LIBs	Lithium-ion batteries
$LiPF_6$	Lithium hexafluorophosphate
MO	Metal oxide
MWCNT	Multi-walled carbon nanotube
SWCNT	Single-walled carbon nanotube
nm	Nanometer
NMP	1-methyl-2-pyrrolidinone
OCV	Open circuit voltage
PPy	Polypyrrole
PVDF	Polyvinylidene fluoride
RTIL	Room temperature ionic liquid
SAED	Selected area electron diffraction

Abbreviations	Full name
SBR	Styrene-butadiene rubber
SEI	Solid electrolyte interphase
SEM	Scanning electron microscopy
TEM	Transmission electron microscopy
TGA	Thermogravimetric analysis
vdW	van der Waals
XRD	X-ray diffraction

List of Symbols

Symbol	Name	Unit
2θ	Peak position of XRD	^{o}
C rate	Charge or discharge rate	mA
E	Electrode potential	V
ED	Energy density	Wh L^{-1}
F	Faraday constant = 96485	C
I	Current	mA
K	Shape factor of the average crystalline	-
L	Crystal size	nm
m	Active material weight	g
PD	Power density	W L^{-1}
Q_c	Specific charge capacity	mAh g^{-1}
Q_d	Specific discharge capacity	mAh g^{-1}
Q_{tsc}	Theoretical specific capacity	mAh g^{-1}
R_{ct}	Charge transfer resistance	Ω
$R_{Ω}$	Ohmic resistance	Ω
SE	Specific energy	Wh kg^{-1}
SP	Specific power	W kg^{-1}
t	Time	h or s
T	Temperature	K or ^{o}C
W	Warburg impedance	Ω
Z”	Imaginary part of the impedance	Ω
Z’	Real part of the impedance	Ω
ΔG	Gibbs free energy	-

Symbol	Name	Unit
η	Coulombic efficiency	%
λ	X-ray wavelength	Å
σ	Conductivity	S m^{-1}

List of Figures

List of Tables

Chapter 1

Introduction

1.1 General background

In the new era of green technology, clean and renewable energy resources have become the most important issue for industrialized countries and multinational corporations, as well as being a focus for research and development. Fossil fuels have been and still are the major energy resources for transportation in societies around the world. Fossil fuels have created a looming problem, however, because they are responsible for emissions of greenhouse gases and pollutants such as nitrogen oxides, sulphur dioxide, and particulate materials [1-2]. Research with the aim of reducing the usage of fossil fuels as energy sources was been started many years ago. Energy storage technologies are expected to offer improved high energy and power densities for sustainable energy resources. The lithium ion battery is one of the most promising candidates for energy storage and has been one of the major energy storage technologies for small electronic devices since the last century. Recently, the global automotive manufacturers have applied lithium ion batteries as the power train for full electric and hybrid electric vehicles. The current commercial lithium ion batteries are not good enough, however, to completely satisfy the public need. At present, the capacity of the state-of-the-art lithium ion battery is limited by the positive electrode, which can store only 150 mAh/g of charge compared with about 300 mAh/g for the graphite anode. The effort to design better electrodes will likely improve the energy density, but at best, by no more than a factor of two. An

interesting approach in this sense is offered by the lithium-air battery (LAB), also called the lithium-oxygen (Li/O_2) battery, which belongs to the family of metal/air devices. A typical cell design is constituted by a lithium metal anode, a porous carbon cathode, and an electrolyte (comprising a dissolved lithium salt). Theoretical values of 3505 Wh kg^{-1} and 3582 Wh kg^{-1} have been recently quoted for non-aqueous and aqueous electrolytes, respectively [3-4]. These high values make LABs particularly appealing for the automotive applications. A real breakthrough still needs to be made in this field, however, to make rechargeable Li/air batteries ready for the market. Several serious problems must be solved to assure proper cycleability and therefore rechargeability, including decomposition of the organic electrolyte at the cathode, protection of the cathode from CO_2 and H_2O by means of a proper O_2-permeable membrane, and lowering of the Li_2O_2 oxidation overpotential on charge [5].

Meanwhile, rapid advances in electronic technology, leading to wearable and roll-up devices, have given more support to the goal of achieving lithium ion batteries with higher power density, improved cycling stability, and better safety. There is currently an enormous ongoing research effort aimed at developing ultra-thin, flexible, and soft batteries to cater for the bendable modern devices. The objective is improved rate capability without a penalty in charge/discharge capacity and sufficient electrochemical cycling stability [6]. Flexible batteries are not only needed for current applications, e.g. for roll-up displays, active radio-frequency identification tags, integrated circuit smart cards, and implantable medical devices, but there is also the intention to place large flexible batteries in hollow spaces of the auto body of future hybrid and electric vehicles. It is needless to stress that high

power density and energy density are expected. Of course, the battery performance is closely related to the structural and electrochemical properties of the electrodes. Hence, the development of flexible electroactive thin film materials has become important.

The improved electrochemical performance in the flexible lithium ion battery system has to be achieved by developing all key factors related to materials for electrodes, separator, electrolytes, and battery assembly. In the case of electrode materials, they are the key factor for fundamental advances in energy conversion and storage in the lithium ion battery system, as well as being the place where electrochemical reactions take place [7]. The separator is also a critical component in liquid electrolyte batteries. It is placed between the positive electrode and the negative electrode to prevent physical contact of the electrodes, while enabling free ionic transport and isolating electronic flow [8]. It mostly is a microporous layer consisting of either a polymeric membrane or a non-woven fabric mat. Essentially, it must be chemically and electrochemically stable towards the electrolyte and electrode materials, and must be mechanically strong to withstand the high tension during the battery assembly operation. Structurally, the separator should have sufficient porosity to absorb liquid electrolyte to allow high ionic conductivity. The presence of the separator adds electrical resistance, however, and takes up limited space inside the battery, which adversely affects battery performance. Therefore, selection of an appropriate separator is critical to the battery performance, including energy density, power density, cycle life, and safety. For high energy and power densities, the separator is required to be very thin and highly porous, while still remaining mechanically strong. For battery safety, the separator should be able to shut the

battery down when overheating occurs, such as the occasional short circuit, so that thermal runaway can be avoided. The shutdown function can be obtained through a multilayer design of the separator, in which at least one layer melts to close the pores below the thermal runaway temperature and the other layer provides mechanical strength to prevent physical contact of the electrodes. In this doctoral study, separators were used in non-aqueous liquid electrolyte for conventional battery assembly, but for flexible lithium battery assembly, the function of the separator was replaced by a polymeric membrane. The advantages of using such a polymeric membrane as the electrolyte component in a lithium cell are as follows:

(i) *Suppression of dendrite growth*. Although conventional separators serve well as the ionic conducting media in rechargeable lithium cells, they unfortunately possess many sufficiently large, electrolyte-containing, interconnected pores such that continuous pathways can develop between the cathode and the anode, and thereby encourage the formation and growth of lithium dendrites during charging periods [9]. These dendrites lower the cycling efficiency and, ultimately, cause internal short-circuiting of the cells [10]. The use of continuous or non-porous polymeric membranes which provide few or no continuous free paths for the electrolyte solution in which lithium dendrites propagate has been one of several successful approaches to suppressing the problem of dendrite growth [11-12].

(ii) *Enhanced endurance to varying electrode volume during cycling.* Polymer electrolytes are more compliant than conventional inorganic glass or ceramic electrolytes. This feature enables the construction of solid-state rechargeable batteries in which the polymer conforms to the volume changes of both electrodes that occur during charge–discharge cycling.

(iii) *Reduced reactivity with liquid electrolytes*. It is generally accepted that no solvent is thermodynamically stable towards lithium [10] or even carbonaceous anodes. Polymer electrolytes, due to their solid-like nature and much lower liquid content, are expected to be less reactive than their liquid electrolyte counterparts.

(iv) *Improved safety*. Solid-state construction of a polymer electrolyte battery is more tolerant to shock, vibration, and mechanical deformation. In addition, since there is little or no liquid content within the electrolyte, cells can be packaged in an evacuated flat `plastic bag', rather than a rigid metal container which is prone to corrosion. This unique characteristic prevents build-up of internal pressure [13] and, hence, removes the possibility of explosion.

(v) *Better shape flexibility and manufacturing integrity*. Due to the need for smaller and lighter batteries, the battery shape factor has become one of the major design issues. A rectangular battery is often preferable to a conventional cylindrical battery, since it occupies space more efficiently in consumer electronics such as cellular phones and laptop computers. A film-like, polymer electrolyte battery is quite promising from this aspect [14]. Another feature associated with polymer electrolyte batteries is the manufacturing integrity; all elements, both the electrolyte and the electrodes of a cell, can be laminated automatically via well-developed coating technology [15].

To achieve these goals, considerable efforts have been devoted to synthesizing nanostructured materials and fabricating flexible cells to provide the best place for the intercalation behaviour of lithium ions to take place. Effective and detailed information regarding experimental procedures and electrochemical performance is also provided in this thesis to enable further research in the future.

1.2 Statement of problem and solution approaches

The lithium ion battery, like other battery systems, consists of three main components: the anode, the cathode, and the electrolyte, where electrical energy is generated by conversion of chemical energy via redox reactions at the anode and cathode [16]. As reactions at the anode usually take place at lower electrode potentials than at the cathode, the terms negative and positive electrode (indicated as minus and plus poles) are used. Lithium-ion batteries are closed systems, with the anode and cathode being the charge-transfer medium and taking an active role in the redox reactions as active masses. Advanced battery technology has been based on the development of different techniques and materials for the electrodes and electrolyte, and thus, on different electrochemical reactions [17].

Usually, the electronic conductivity of an electrode material is very low in the lithium ion battery system, so it is necessary to add a conductive layer into the active materials. Although the commercial lithium ion battery has been successful on the global market as the energy source for small and medium electronic devices, in the case of electric vehicles or hybrid vehicles, the performance of the lithium ion battery is not good enough for current applications which require high energy and power densities. To meet these demands, the development of rechargeable lithium ion batteries has been the focus of considerable research, and active research is still continuing on all aspects of lithium ion batteries, i.e., anodes, cathodes, electrolytes, and cell construction. In this doctoral work, anode and cathode materials have been the central focus of the study; in addition some work on gel electrolyte and cell construction for flexible batteries is reported in detail.

1.2.1 Anode materials

Among all the possible anode material reported, one-dimensional carbon-based materials (in particular carbon nanotubes) have been suggested as a viable option for flexible electrodes due to their one-dimensional structure with high length to diameter ratios, along with their high porosity and large surface area [18-20]. Many researchers and enthusiasts have claimed that carbon nanotubes (CNTs) will radically improve the performance of batteries because of their unique structure, which could especially enhance the kinetic properties of the electrodes and could result in extremely high specific charge compared with the theoretical limits of graphitic carbon [21-22]. It has been reported in the literature that multi-wall carbon nanotube (MWCNT) based electrodes have exhibited reversible charge storage capacity in the range of 100-600 mAh g^{-1}, depending on the CNT preparation method, CNT structure, and cycling procedure [23-27]. On the other hand, single-wall carbon nanotubes (SWCNTs) have been reported as having the potential to accommodate up to one lithium per every three carbons on charging, and even possibly more [28-29]. The lithium storage capacities of SWCNTs have been determined experimentally to be significantly higher than that of intercalated graphite, namely > 1000 mAh g^{-1} [30-34]. The critical challenge for the CNT electrochemical properties, however, is the high irreversible charge capacity in the first cycle [35]. Some outstanding non-electrochemical properties of CNTs, such as their high theoretical tensile strength and high electrical and thermal conductivity [23], also make CNTs potentially useful, preferentially as an additive or matrix for composite electrodes in the Li-ion battery system.

Carbonaceous materials, usually either graphite or coke, are also well known as standard anode materials for the lithium-ion battery [36]. The main advantages of choosing these materials are the low cost and the low operational voltage. The carbonaceous anode is coupled with a high voltage cathode, e.g. $LiCoO_2$, in order to obtain a battery operating in the 4 V range. Moreover, the mechanism of lithium intercalation in the anode, i.e. graphite or soft carbon, is well known. The intercalation proceeds through well-identified, reversible stages, corresponding to progressive intercalation within discrete single layers of carbon (graphene), to reach the formation of LiC_6, with a maximum theoretical capacity of 372 mAh g^{-1} [37]. The graphite anode has the disadvantages of low energy density, however, as well as safety issues related to lithium deposition and a significant irreversible loss in capacity after only one cycle [38]. Therefore, new anode materials, including Si (3579 mAh g^{-1}), Sn (992 mAh g^{-1}), and transition metal oxides (500-1000 mAh g^{-1}), with high theoretical capacity, low cost, enhanced safety, and long cycle life have been considered the most promising alternative anode materials. The main challenge for the implementation of such anodes, however, is their large volume change during lithium insertion and de-insertion. The electrode suffers cracking and crumbling, and consequent loss of interparticle contact [38-39], resulting in the loss of capacity.

1.2.2 Cathode materials

Cathodes are a requisite and fundamental part of lithium-ion batteries, so great research efforts have been devoted to exploring new cathode materials in order to decrease costs and improve safety issues [40]. Vanadium pentoxide (V_2O_5) and molybdenum trioxide (MoO_3) were two of the earliest studied oxides for cathode materials for the lithium ion battery. Vanadium pentoxide has been investigated for

30 years [41-42]. It has a layered structure with weak vanadium-oxygen bonds between the layers. Due to its layered structure, the insertion of up to ~3 mol Li^+ ions per formula unit leads to the high theoretical capacity of ~400 mAh g^{-1} [43-44]. V_2O_5 also has the advantages of low cost and abundant resources in the earth's crust. Problems such as severe capacity fading and poor rate capability, however, prevent its use in commercial lithium batteries. A variety of molybdenum oxides have been noted as possible cathode active materials in secondary lithium batteries [45-48]. Among these oxides, molybdenum trioxide (MoO_3) has a relatively high discharge capacity as cathode, but the cell voltage is not high compared with practical cathode active materials such as MnO_2 and V_2O_5 [49-50]. Also, the cell voltage on charging and the poor cycling behaviour need to be improved to facilitate the development of practical batteries. Among the other candidate cathode materials, compounds with three-dimensional structures ($LiMn_2O_4$, $LiFePO_4$) and layered structures ($LiMO_2$ with M = Co, Ni) are the most widely studied due to good insertion/de-insertion properties [51]. Although $LiCoO_2$ is still being used as a successful cathode material in most commercial lithium ion batteries, the raw materials are less available, more toxic, and more costly than for other transition metals, such as manganese, nickel, and iron. In addition, $LiCoO_2$ is not as stable as other potential electrode materials, which can lead to performance degradation or failure when overcharged [52-54]. Layered $LiNiO_2$, spinel $LiMn_2O_4$, and olivine $LiFePO_4$ have become more attractive, since Ni, Mn, and Fe are less expensive and less toxic than Co. Nevertheless, $LiNiO_2$ suffers from structural changes, thermal runaway, and difficulties in synthesizing it as an ordered material with all Ni^{3+} ions [55-56], while $LiMn_2O_4$ suffers from severe capacity fade at elevated temperatures, along with other disadvantages such as

manganese dissolution, Jahn-Teller distortion, loss of crystallinity, and development of microstrain during cycling [57-59]. Moreover, $LiMn_2O_4$ has a limited capacity, about 120 mAh g^{-1}, which less than that of $LiCoO_2$ (140 mAh g^{-1}). Olivine-like $LiFePO_4$ has come to be an interesting positive electrode material for lithium-ion batteries because of its low toxicity, low cost, long cycle life, and good cell safety. A primary problem of this material, however, which prevents it from being used in large-scale industrial applications, is its poor high-rate performance, owing to its low electronic conductivity and low ionic diffusion coefficient [60].

1.2.3 Electrolyte

Over the past two decades, commercial lithium batteries have used electrolytes containing $LiPF_6$ salt dissolved in a mixed carbonate solvent, even though they are unsafe, due to the use of flammable organic electrolyte, poor thermal stability of the cathode electrolyte interphase, and the formation of lithium dendrites [61]. $LiPF_6$ is believed to be the main cause for poor performance of lithium batteries at high temperature. Goodenough and Kim reported [62] that the ideal electrolyte should offer retention of the electrode/electrolyte interface during cycling, when the electrode particles are changing their volume, conductivity of more than 10^{-4} S cm^{-1} over the temperature range of battery operation, chemical stability over the ambient temperature range, low toxicity, and low cost.

Room-temperature ionic liquids (RTILs) have been considered as alternative electrolytes for lithium-ion batteries due to advantages such as high oxidation potential (~5.3 V vs. Li^+/Li), non-flammability, low vapour pressure, high boiling points, and high Li-salt solubility [63-65]. The high viscosity of these ionic liquids,

however, reduces the Li-ion conductivity. Solid polymer electrolytes (SPE) are considered to have a safety advantage over the organic and inorganic liquid electrolytes because of their lower reactivity with lithium and the absence of any organic solvent which can cause environmental hazards [66], although the "dry solid system" of SPE electrolytes suffers at present from poor ionic conductivity (~10^{-5} S cm^{-1} at 20 ^{o}C). Polymer gels or gel electrolytes are an alternative solution combining the advantages of liquid electrolytes and solid electrolytes. Gel electrolytes incorporating organic solvents have shown room temperature conductivities as high as 10^{-5} S cm^{-1}.

1.2.4 Design of flexible cell

To build fully flexible and robust electrochemical devices, electrodes with specific electrochemical and mechanical properties need to be explored to fulfil these requirements. The traditional Li-storage material electrodes suffer from serious cracking and poor physical properties when they are frequently bent or loaded by impact bending, which is mainly due to weak bonding between the materials and the current collector. A thin free-standing electrode film with complete mechanical flexibility during operation could solve these problems. In order to construct a flexible cell, it is necessary to fabricate all the battery components, the anode, a gel or solid electrolyte, the cathode, and the current leads into multi-layered films by suitable techniques. Nanostructured electrode materials, particularly one-dimensional (1D) nanowires/nanorods/nanobelts [67-70], are considered to be the most promising avenue towards fabricating free-standing film electrodes. The 1D nanowire, nanorod, or nanobelt morphology not only has a large electrode−electrolyte contact area and facile strain relaxation, but also efficient 1D electron transport pathways [67-68].

Usually, thin free-standing electrodes (both anode and cathode) are fabricated by the vacuum filtration method or electrochemical deposition [35, 71-74]. In some cases, chemical vapour deposition (CVD) and pulsed-laser deposition (PLD) are used [75-77]. For practical cells, a carbon based anode and metal-oxide-based cathode have been selected, as they can provide maximum specific energy, sufficient specific power, and long cycle life. The moisture and air trapped in the pouch-type cell are other dominant factors during the assembly of flexible cells. By using polymer or gel electrolyte, some flexible batteries less than 5 mm in thickness are already available [78]. Obviously, besides the material properties, the fabrication techniques for the electrodes and the cell design are also important sources of improvement.

1.2.5 Approaches for improving electrode performance

In order to improve the energy storage capacity, cycling stability, and mechanical flexibility, for the flexible lithium battery in particular, several strategies have been developed to reduce the detrimental effects of large volume variation in electrode materials and to alleviate the side reactions with electrolyte. These approaches are discussed below:

Nanoscale structured materials for electrodes

Nanostructured materials are the heart of fundamental advances in efficient energy storage and/or conversion, where surface processes and transport kinetics play important roles. Nanoscale materials are endowed with unusual mechanical, electrical, and optical properties by confining the dimensions of such materials, and the overall behaviour of nanostructured materials exhibits combinations of bulk and surface properties [79]. The lithium ion battery field is one of a number that have

benefited from the introduction of nanotechnology: the application of nanostructured materials has significantly improved and enhanced the lithium ion intercalation capability, e.g. storage capacity, intercalation rate, and cycling stability [80]. Considering the liquid-solid interface reaction characteristic of lithium ion intercalation, followed by diffusion into the electrode bulk, it is reasonable to expect that a large surface area and short lithium ion diffusion path can ensure complete Faradaic reaction at the interface and facilitate the diffusion into the bulk. Thus nanoscale electrodes which meet these requirements are highly favourable as intercalation hosts instead of bulk electrodes consisting of micrometer sized particles.

Carbon-based composites

Carbon-based materials are a major component of electrodes, due to their high electronic conductivity and robustness, and the rich functional surface chemistry of carbon. Great research interest has been dedicated to the development of electrodes with advanced architectures using nanostructured carbon materials (carbon nanotubes or nanofibers, ordered mesoporous materials, etc.), in contrast to the 'classical' carbon materials based on graphite, glassy carbon, and carbon black [81]. The beneficial effects of carbon addition or a carbon coating also have been widely observed in many studies. The improved cycling performance of carbon-based composites could be attributed to the improved electric conductivity and the buffering effect of carbon [82-84]. Carbon additives also have the advantages of good ionic conductivity, low volume expansion, tolerance to mechanical stress, and Li-storage capability [84-85]. It has also been reported that a carbon coating exerts a compressive stress on the active particles, which acts as an opposing force against

particle volume expansion during lithiation and thus limits the pulverization of the particles [86].

One or two-dimensional nanostructured materials

One of the most promising approaches is to design one or two-dimensional (1 or 2D) nanostructured materials with sufficient surface area to accommodate the large volume expansion during Li insertion and extraction [87-89]. 1D nanostructured materials have many advantages for use in electrodes for lithium-ion batteries [90], such as the large surface area, which provides a large contact area between the active materials and the electrolyte, the continuous network, which is expected to improve the electrical conductivity, a large surface area that can buffer the large volume changes caused by disintegration of the structure, and suitable 1D structures that may block the re-aggregation of the superfine particles. As a result, these materials can show improved reversible capacity, enhanced cycling performance, and elevated rate capability.

Conductive polymer coating

Conducting polymers, such as polyacetylene, polyaniline, and polypyrrole (PPy), have been studied as electrode materials for rechargeable batteries because they are electrochemically active and permit penetration of the electrolyte into the polymer mass. These polymers can be charged and discharged by a redox reaction involving lithium ions or counter anions of the electrolyte [91-92]. Among the conducting polymers, PPy is one of the most popular for use in a cathode; it has an open circuit voltage (V_{OC}) versus Li^+/Li of $2 < V_{OC} < 4$ V, with a specific energy ranging from 80 to 390 Wh kg^{-1} [92]. Thus, research efforts were essentially concentrated on the

utilization of PPy as a conducting agent for the positive electrode (cathode) in lithium batteries.

1.3 Significance of the study

The past two decades have shown that the exploration of the properties of nanomaterials can lead not only to substantially new insights regarding fundamental issues, but also to novel technological perspectives. So, it is now believed that the combination of hybrid materials science and nanotechnology could be the best way to achieve breakthroughs in the energy storage field, especially with respect to the lithium-ion battery. In this doctoral work, systematic experimental investigations were carried out to improve the performance of electrodes based on hybrid and nanostructured materials. Generally, the potential advantages of the use of hybrid and nanostructured materials as electrode can be summarized as below:

1. Nanostructured electrode materials may not only introduce innovative reaction mechanisms, but also improve the electrochemical properties over those of their bulk counterparts.
2. Nanostructured electrode materials provide a larger electrolyte contact area, which is beneficial to high current rate performance, because Li ion diffusion and electron transport are highly dependent on the transport path length and accessible sites on the surface of the active materials. On other hand, conductive composites can enhance the transfer of electrons.
3. Nanostructured electrode materials may also deliver good cycling stability. The capacity fading of lithium ion batteries upon cycling is usually caused by the large volume expansion associated with Li insertion and extraction.

Nanostructured electrodes can absorb this large volume change during insertion/extraction, preserving the integrity of the electrode, which leads to stable cycling performance. Conductive hybrid materials are also beneficial for the electrolyte diffusion into the bulk of the electrode, provide fast transport channels for the Li ions, and accommodate the volume variation more effectively, thus increasing the structural stability of the electrode.

The overall objective is to contribute to a comprehensive insight into the factors controlling lithium-ion electrode performance, from the synthesis of nanostructured and hybrid materials to the details of phase-related electrochemical behaviour. The ultimate goal is to investigate the mechanisms involved during electrochemical cycling and to understand how nanostructured and hybrid materials influence the electrochemical performance of lithium-ion batteries. Therefore, in this thesis work, many different types of electrochemical and structural characterization techniques have been adopted, in the hope of accomplishing this objective.

1.4 Research objectives

Based on previous work and published papers in international journals by other researchers, the author was initially motivated to explore synthesis techniques, structural characterization, and electrochemical performance evaluation of different types of hybrid and nanostructured materials as potential candidates for use as electrode materials in lithium-ion batteries. The following objectives have been addressed to achieve the main goals:

1. To synthesize novel conductive nanohybrid electrode materials for lithium-ion batteries.
2. To synthesize nanostructured materials for electrodes of lithium ion batteries.
3. To characterize the synthesized materials by numerous techniques in order to understand the structural, morphological, physical, and also the electrochemical behaviour.
4. To increase the practical specific capacity of the electrode materials to near their theoretical capacity with excellent rate capability and cycling stability.
5. To contribute to the next technology breakthrough in order to open up a new window for the next generation of lithium-ion batteries, especially for flexible lithium batteries.

1.5 Structure of thesis

The scope of the research which has been carried out in this doctoral work is briefly outlined below:

In this Chapter, a general background and major problems associated with lithium-ion battery electrodes are presented. Possible approaches for improving electrode performance, and the significance and objectives of this study are also discussed.

Chapter 2 presents a thorough literature review on the current state-of the art lithium ion battery, especially with respect to the role of nanostructured and hybrid material for electrodes, and their possible synthesis techniques.

Chapter 3 describes the materials, chemicals, and methods used to synthesize the nanostructured and hybrid materials, and the instrumental analysis techniques used to

characterize the electrode materials, including X-ray diffraction (XRD), thermogravimetric analysis (TGA), scanning electron microscopy (SEM), field emission scanning electron microscopy (FESEM), transmission electron microscopy (TEM), Raman spectroscopy, Fourier transform infrared spectroscopy (FTIR), tensile testing, charge-discharge testing, cyclic voltammetry (CV), and electrochemical impedance spectroscopy (EIS).

Chapter 4 and 5 present the synthesis techniques and electrochemical performance of the potential anode materials that were studied, SnO_2/MWCNT and SWCNT/SnO_2, respectively.

Chapter 6 and 7 discuss the synthesis techniques and electrochemical performance of the potential cathode materials that were studied, V_2O_5-polypyrrole and MoO_3/graphene, respectively.

Chapter 8 summarizes the results of this doctoral work and provides some outlooks for further research work related to electrode materials.

Chapter 2

Literature Review

2.1 Introduction

The industrial revolution of the past few centuries has been powered mainly by variations of the combustion reaction, the fire that marked the dawn of humanity, resulting in emissions of carbon dioxide [93]. The issue of global climate change has driven an energy economy that must be based on a cheap and sustainable energy supply. Battery devices can potentially provide a solution, especially as they can be used to store energy from sustainable sources such as the wind and solar power. Together with the enthusiasm and rapid advances in the electric automotive industry towards the development of electric vehicles (EV) and hybrid electric vehicles (HEV), these factors have combined to make the development of improved rechargeable batteries a worldwide trend. Researchers thus have the responsibility for providing the world with better and more efficient batteries. Advancement in battery technology has been relying in the development and use of different types of nanostructured materials for electrodes and electrolytes, and thus on different electrochemical reactions [17, 89]. To compare the different battery types in term of their performance, Fig. 2.1 shows the Ragone chart which plots specific energy versus specific power (the latter usually represented on a logarithmic axis), where one can compare easily the different batteries suitable for use in either battery-electric vehicles (which foremostly need energy) and hybrid vehicles (which foremostly need power) [94]. It should be noted that the areas on the chart each

represent an electrochemical couple, but that several design options are possible to optimize the battery performance for its application. Obviously, lithium-based batteries currently outperform other systems because of their high energy density and design flexibility. The current technologies for producing rechargeable lithium ion batteries, however, do not completely satisfy all requirements. In recent years, great efforts have been devoted to the development of various electrode materials and have moved closer towards reaching the requirements. Here, certain kinds of electrode materials, especially self-supported electrode for flexible lithium ion batteries, will be investigated and discussed in detail in this doctoral work.

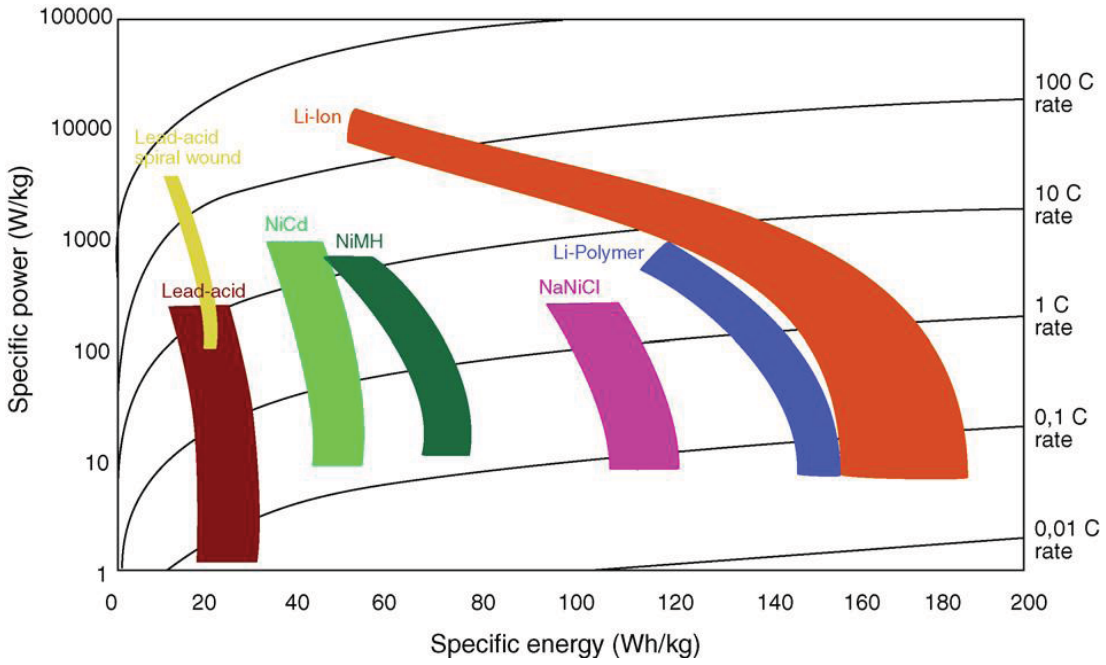

Figure 2.1 Comparison of the different battery technologies in terms of specific energy and specific power [94].

2.2 Historical developments of lithium-ion rechargeable batteries

For years, battery researchers have been fascinated with the prospect of using lithium as the anode material in batteries, because of its light weight (molar mass M = 6.94 g mol^{-1}, and density ρ = 0.53 g cm^{-3}) and extremely electropositive character (~3.04 V versus standard hydrogen electrode) [61]. The first lithium-based battery was developed in the early 1970s and was a room temperature lithium primary or non-rechargeable type, which used sulphur oxide (SO_2) dissolved in an organic solvent (along with a lithium halide electrolyte) as the active positive electrode reactant and a lithium metal negative electrode [95]. During the 1970s and 1980s, many researchers were involved in programs to develop rechargeable batteries and discovered that several inorganic compounds could react with lithium in a reversible way. This led to the development of alternative battery systems that utilized layered transition metal dichalcogenides. In 1972, Whittingham was the director of a large project using TiS_2 as the cathode electrode, Li metal as the anode electrode, and lithium perchlorate in dioxolane as the electrolyte [96]. TiS_2 was the best intercalation compound available at the time, having a very favourable layered-type structure and was the most promising candidate for the energy electrode due to its light weight [97-98]. In spite of the impeccable operation of the positive electrode, however, the system was not viable. It soon encountered the shortcomings of a Li metal/liquid electrolyte combination − uneven Li growth as the metal was replaced during each subsequent discharge-charge cycle, which led to explosion hazards. The safety issue, the low potential, and the high production cost of this material caused people to start to move to layered oxide materials [99]. Vanadium pentoxide (V_2O_5) and molybdenum trioxide (MoO_3) were two of the earliest studied oxides. MoO_3 is

of little interest due to its low rate capability [100], whereas V_2O_5 has been investigated for the past 30 years [61, 101-102]. It has a layered structure with weak vanadium-oxygen bonds between the layers and is now known to react by an intercalation mechanism. The multiphase transition and rapid capacity loss on cycling, however, makes this material unsuitable for commercial application in rechargeable batteries [101-102]. In the 1980s, Goodenough and his co-workers discovered the open framework Li_xMO_2 (M = Co, Ni or Mn) family of compounds as more suitable positive electrode materials [103-104]. They recognized that $LiCoO_2$ had a similar structure to layered structures of the dichalcogenides and showed that the Li ion could be inserted and extracted electrochemically, thus making $LiCoO_2$ a very promising cathode material. On the other hand, the introduction of carbon as an anode material in lithium-ion secondary batteries has an interesting history. Lithium insertion in graphite host lattices from conventional non-aqueous solvents was reported as early as 1976 by Besenhard [105]. Nevertheless, disintegration of the graphite host lattice during intercalation/de-intercalation has remained an unresolved issue. The search for new solvent-supporting electrolyte systems, including polymer electrolytes, to ensure reversible intercalation/de-intercalation would improve the cycle life of graphite material [106]. Sony Corporation reported that lithium insertion could also be successfully carried out in disordered carbon material [107]. This opened up many possibilities in terms of carbon material sources and the choice of solvent-supporting electrolyte systems. Following a parallel sequence of developments which resulted in the selection of $LiCoO_2$ as the cathode material, Sony introduced the first successful disordered-carbon-based[108] Li-ion batteries, which were commercialized in 1991. This type of Li-ion battery, having a potential

exceeding 3.6 V (three times that of alkaline systems) and gravimetric energy densities as high as 120-150 Wh kg^{-1} (two or three times those of the usual Ni-Cd batteries), is found in most high performance portable storage devices that have been developed in the past two decades. These lithium ion batteries had a strong impact on the battery community all over the world because of their high operating voltage. Nevertheless, the safety issue is still a serious problem related to the organic solvent used in liquid electrolyte. Reaction between the organic solutions and the electrode surface occur when the temperature of the cell increases, particularly if the solid-electrolyte interphase (SEI) is disrupted. The SEI is the contact surface between the electrolyte solution and the electrode material consisting insoluble products generated during the battery is charged for first time [109]. This interface becomes unstable when the cell temperature rises above 70-100 ^{o}C and decomposes exothermically. The rise in temperature is generated by irreversible heat linked with the internal resistance and reversible heat related to the reduction reaction that take place in the positive electrode and the heat generated at the negative electrode [110]. Thermal runaway of lithium-ion batteries has been described in three-stage process [111]:

(i) Anodic reactions start at about 90 ^{o}C. This is the rate-limiting step. As temperature rises above 120 ^{o}C, decomposition of the solid electrolyte (SEI) layer follows, leading to reduction of the electrolyte at the lithiated negative electrode.

(ii) In a second step of the thermal runaway mechanism, exothermic reactions at the positive electrode start as the temperature rises over 140 ^{o}C. Oxygen rapidly evolves at this stage.

(iii) The positive electrode decomposes and the electrolyte gets oxidised at temperature above 180 ^{o}C. This is a high-rate exothermic process with a temperature rise as high as 100 ^{o}C per min.

To circumvent the safety issues surrounding the use of organic solvent in the liquid electrolyte, several alternative approaches and strategies were pursued. The best potential approach involved replacing the liquid electrolyte by a dry polymer electrolyte, in batteries denoted as Li solid polymer electrolyte (Li-SPE) batteries [112], although this technology is limited to large systems (electric stationary or backup power systems) and is not suitable for portable devices due to their high temperature operation (up to 80 ^{o}C). To benefit from the advantages of polymer electrolyte technology without the hazards associated with the use of Li metal, some researchers tried to develop a Li hybrid polymer electrolyte (Li-HPE) battery [113]. This type of electrolyte consists of three components: a polymer matrix, which is swollen with liquid solvent, and a Li salt. However, HPE systems have never been commercialized on an industrial scale due to serious safety issues related to the growth of Li-metal dendrites. With the goal of combining the recent commercial success enjoyed by liquid Li-ion batteries with the manufacturing advantages presented by the polymer technology, Tarascon and co-workers [114] introduced polymer electrolytes into a liquid Li-ion system. They developed the first reliable and practical rechargeable Li-ion HPE battery, called the plastic Li-ion (PLiON) battery, which differs considerably from the usual coin, cylindrical or prismatic-type cell configurations (Fig. 2.2). Such thin-film battery technology, which offers shape versatility, flexibility, and lightness, has been under commercial development since 1999 and has many potential advantages in the continuing trend towards electronic

miniaturization. The next generation of integrated liquid-electrolyte Li-ion cells, derived from the plastic Li-ion concept, are finally beginning to enter the market place. These new cells use a gel-coated, microporous polyolefin separator laminated to the electrodes, rather than use the poly(vinylidenefluoride-co-hexafluoropropylene) (PVDF-HFP)-based membrane used in the plastic Li-ion cells.

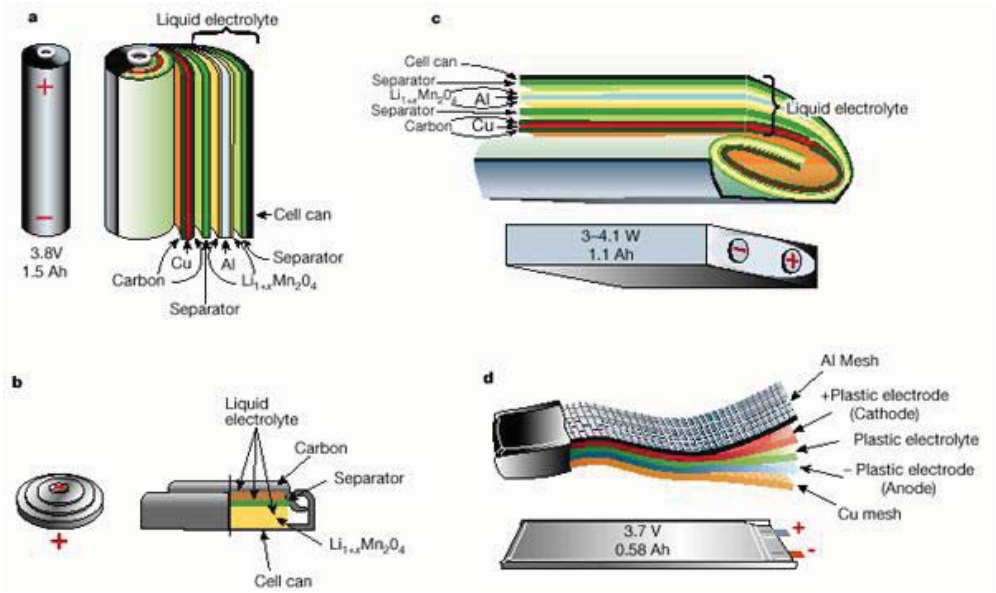

Figure 2.2 Schematic drawings of various types of Li-ion cell constructions: (a) cylindrical; (b) coin; (c) prismatic; and (d) flexible [61].

2.3 Fundamentals of electrochemistry

Electrochemistry includes the study of chemical properties and reactions involving ions either in solution or in solids. In order to study these properties, electrochemical cells are generally constructed. A typical cell consists of two solid electrodes, the cathode and the anode, in contact with an ionic conducting electrolyte. A galvanic cell is an electrochemical cell that is capable of converting chemical

energy into electrical energy. It generates electricity as a result of the spontaneous electrode reaction inside it.

2.3.1 Principle of reaction mechanism of lithium-ion battery

A typical lithium-ion battery is comprised of a positive electrode (cathode) formed normally from a layered structure, such as lithium transition metal (M) oxides e.g. $LiCoO_2$, a non-aqueous electrolyte (e.g. $LiPF_6$ in ethylene carbonate/dimethyl carbonate (EC/DMC)) with a separator and a negative electrode (anode) based on graphitic layered carbon materials, such as natural graphite and other carbonaceous materials. A non-aqueous electrolyte can be substituted by a polymer gel or solid polymer electrolyte is placed between the two electrodes for ion transfer. A schematic diagram of the charge/discharge process in a rechargeable lithium-ion battery is shown in Fig. 2.3.

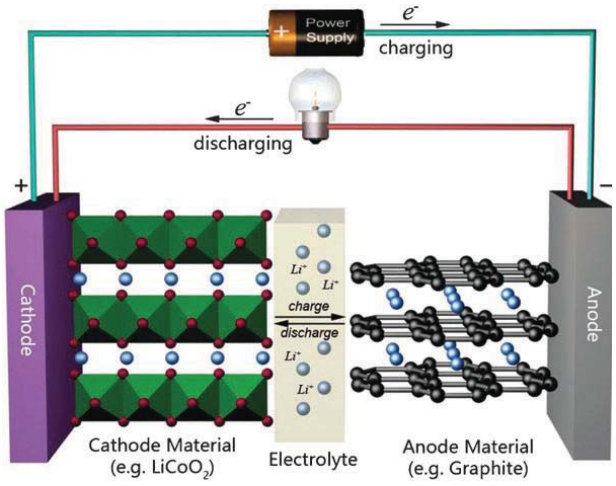

Figure 2.3 Schematic representation and operating principles of the rechargeable Li-ion battery [115].

The mechanism of the lithium-ion battery can be considered as based on the flow of lithium ions inside the battery between anode and cathode and, at the same

time, transport of electrons outside the battery (external circuit) between anode and cathode. As the lithium-ions are included in the cathode material, the cells need to be charged first to allow lithium ions to be de-intercalated from the cathode and spread throughout the electrolyte to be inserted into the negative electrode material. During the discharge process, lithium ions are extracted from the anode and are inserted into the cathode through the electrolyte. The generation of lithium ions and electrons occurs simultaneously from the reaction, $Li \rightarrow Li^+ + e^-$, where the cathode electrode is oxidized and the anode electrode is reduced during charge, respectively. The reactions involved in the charge and discharge processes are described below [116-117]:

At the positive electrode:

$$LiMO_2 \leftrightarrow Li_{1-x}MO_2 + xLi^+ + xe^- \quad (2.1)$$

At the negative electrode:

$$6C + xLi^+ + xe^- \leftrightarrow Li_xC_6 \quad (2.2)$$

Overall reaction:

$$6C + LiMO_2 \leftrightarrow Li_{1-x}MO_2 + Li_xC_6 \quad (2.3)$$

The electrode must allow for the flow of both lithium ions and electrons, however, and thus the electrode must have both good ionic conductivity and good electronic conductivity. Simply, the lithium ions move back and forth between the cathode and anode upon charging and discharging, which gives rise to a potential difference of about 4 V between the two electrodes, while the battery capacity is dependent on the amount of lithium ions that can be extracted from the cathode materials. The name "lithium ion" for the batteries originates from this simple mechanism, which is the transfer of lithium ions between the anode and cathode.

During first charge of the Li-ion battery, the electrolyte undergoes reduction at the negatively polarized anode surface. This forms a passive layer comprising inorganic and organic electrolyte decomposition products. In an ideal case, this layer prevents further electrolyte degradation by blocking the electron transport through it, while concomitantly allowing Li-ions to pass through during cycling. This essential passive layer has appropriately been named the solid electrolyte interphase (SEI) [118]. The onset potential of SEI formation is not a fixed value. The literature offers values such as 2 V [119], 1.7 V [120], or 1 V [121], but 0.8 V [122-123] is the most widely adopted practical value. SEI formation may also continue up to a few cycles. This parameter cannot be normalized, however, because it depends on a number of factors, such as the nature and composition of the electrolyte, the nature of the additives used in the electrolyte [124], sweep rates [125], etc. It is desirable to have complete SEI formation before Li-ion intercalation begins (> 0.3 V [126]). The SEI is a very complicated layer comprising inorganic components, which are normally salt degradation products, and organic components, which are partial or complete reduction products of the solvent in the electrolyte. The thickness of the SEI may vary from few Angströms to tens or hundreds of Angströms [127]. It is difficult to distinctly measure the SEI thickness, as some of the components are partially soluble in the electrolyte [128]. Because formation of a new phase between the active material and the electrolyte modifies the interphase resistance, the average thickness was estimated using electrochemical impedance spectroscopy (EIS) [129]. The picture of a real SEI inside the battery has always been a blur. Models of the SEI on graphite were proposed by Peled et al. [130], Aurbach [119, 126], and Edström et al. [123]. They all suggest that the SEI is a dense layer of inorganic components

close to the carbon, followed by a porous organic or polymeric layer close to the electrolyte phase. Crystals of LiF are also sometimes detected [131]. Every parameter and property of the SEI significantly affects battery performance. The composition, thickness, morphology, and compactness are just a few. Irreversible charge "loss" (ICL) in the first cycle occurs due to solvent reduction and SEI formation, and is hence a characteristic of the SEI [132]. Detrimental processes occurring during storage (self-discharge) also depend on the ability of the SEI to passivate the active material surface. Hence, the shelf-life of a battery also depends on the SEI [133]. As mentioned above, the SEI may also dissolve and/or evolve during cycling. Thus, an effective and stable SEI is mandatory for good cycling life of the battery [134]. It becomes even more important during cycling at high rates and at deeper depth of discharge [61]. SEI components are highly temperature sensitive. Thus, performance of the battery at high/low temperature is dependent on the SEI [135]. The most important consequence of the SEI, however, relates to the safety of the battery [136]. An ideal SEI should have minimum electronic and maximum Li^+ conductivity. SEI formation kinetics should be fast, allowing it to form completely before the onset of Li^+ intercalation. In other words, SEI formation potential should be more positive than Li^+ intercalation potential. An ideal SEI should have uniform morphology and composition. A good SEI should be a compact layer adhering well to the carbon. It should be elastic and flexible [137] to accommodate non-uniform electrochemical behaviour and active material breathing.

2.3.2 Fundamental properties

To evaluate the properties of electrodes in a secondary cell, some general concepts are introduced below:

- *Active mass*: active mass is the material that generates electrical current by means of chemical reaction within the battery.
- *Open circuit voltage (OCV)*: open circuit voltage is the voltage across the terminals of a cell or battery when no external current flows. It is usually close to the thermodynamic voltage for the system.
- *Potential*: the cell potential is determined by the difference between the chemical potential of the lithium in the anode and cathode,

  $\Delta G = -EF$ (2.4)

  where ΔG = Gibbs free energy

  F = Faraday constant (96485 C)

  E = electrode potential

  For the rechargeable lithium-ion cell, the cathode and anode are defined as the higher potential and lower potential electrodes, respectively. Typically, the electrochemistry of the total lithium cell reaction can be investigated using a half cell with lithium metal as counter and reference electrode, denoted as vs. Li^+/Li, for convenience in research. Therefore, the active materials we will discuss later are all working as cathode materials in the half cell, but what they really are is determine by the potential. Normally, the cathode materials show a potential vs. Li^+/Li higher than 2 V, while the anode materials show a potential vs. Li^+/Li lower than 2 V. Fig. 2.4 summarizes the

electrochemical potential and the typical lithium ion storage capacities of both anodic and cathodic materials.

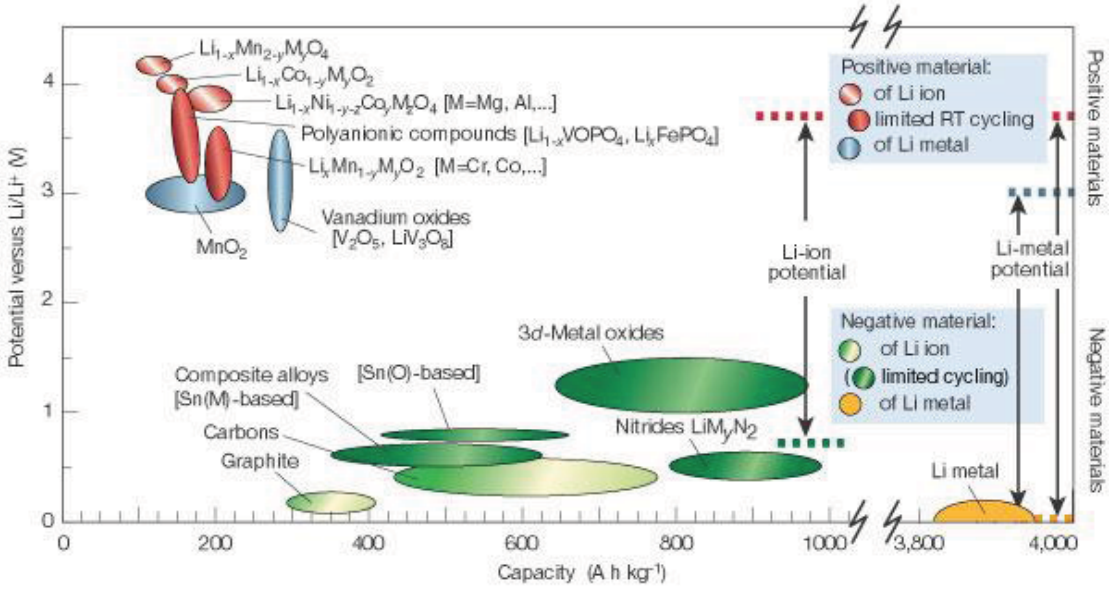

Figure 2.4 Voltage versus capacity for positive- and negative-electrode materials [61].

- *Discharging*: discharging is the operation in which a battery delivers electrical energy to an external load.
- *Charging*: charging is the operation in which the battery is restored to its original charged condition by reversal of the current flow.
- *Overcharging*: attempting to charge a battery beyond its electrical capacity can also lead to a battery explosion, leakage, or irreversible damage to the battery. It may also cause damage to the charger or device in which the overcharged battery is later used.

- *Short circuiting*: a short circuit can lead to a battery fire or explosion. It often occurs when a battery is connected to itself, creating two points on a circuit with different potentials connected with zero or near-zero resistance.
- *Memory effect*: the memory effect is a vague description of a temporary loss of capacity for the Ni-Cd battery system. The "memory effect" refers to the phenomenon where a nickel/cadmium battery loses the ability to deliver full capacity if it is utilized only partially for a prolonged period of time. In practice, every kind of temporary capacity loss is often called a "memory effect".
- *Theoretical specific capacity*: other than the potential, the specific capacity is also an important parameter to evaluate the active materials. The theoretical specific capacity (Q_{tsc}) can be calculated from the equation:

$$Q_{tsc} = \frac{n \text{ x } F}{3600.M} \tag{2.5}$$

where n is the number of moles of electron transfer in the electrochemical reaction, F is the Faraday constant (96485 C), and M is the molecular weight of the active materials.

- *Specific charge capacity/specific discharge capacity*: the specific charge capacity (Q_c) or specific discharge capacity (Q_d) is calculated based on the total amount of charge transferred:

$$Q_c \text{ or } Q_d = \frac{I \text{ x } t}{m} \tag{2.6}$$

where I is the current (mA), t is the time (h), and m is the mass of active materials (g).

The unit of Qc and Qd is mAh g^{-1}.

- *Energy*: it is usually desirable that the amount of energy stored in a given mass or volume is as high as possible. The concepts of specific energy (*SE*, Wh kg^{-1}) or energy density (*ED*, Wh L^{-1}) allow comparison of the energy content or energy density.

$$SE = \frac{E \text{ x } Q}{1000} \tag{2.7}$$

$$ED = \frac{SE \text{ x } m}{V} \tag{2.8}$$

where E is the voltage (V) of the cell, Q is the specific capacity (mAh kg^{-1}), m is the weight of the cell (kg), and V is the volume of the cell (L).

- *Power*: specific power (*SP*, W kg^{-1}) and power density (*PD*, W L^{-1}) refer to the ability of the cell to deliver power per unit mass and unit volume, respectively.

$$SP = \frac{SE}{t} \tag{2.9}$$

$$PD = \frac{ED}{t} \tag{2.10}$$

where t is the discharge time (h).

- *Rate capability*: rate capability is another parameter to evaluate electrode performance. The term charge/discharge rate or C-rate is often used to describe how fast the cell can be charged or discharged. C denotes either the theoretical charge capacity of a cell or battery (mAh) or the nominal capacity of a cell or battery, as indicated by the manufacturer.

- *Irreversible capacity loss*: it is also important to define how much capacity is lost after each cycle. The irreversible capacity can reflect the stability of cells

upon cycling. Irreversible capacity loss is therefore explained by the following equation:

For anode materials:

$$Irreversible\ capacity\ loss = \frac{nQ_d - nQ_c}{nQ_d} x\ 100\% \quad (2.11)$$

For cathode materials:

$$Irreversible\ capacity\ loss = \frac{nQ_c - nQ_d}{nQ_c} x\ 100\% \quad (2.12)$$

where n is the number of cycles for the charge-discharge test, Q_d is the specific discharge capacity and Q_c is the specific charge capacity for each cycle.

- *Capacity retention*: capacity retention is the ratio of the last cycle to the first cycle discharge capacity and is calculated as a percentage, as below:

$$Capacity\ retention = \frac{C_n}{C_1} \text{x } 100\% \quad (2.13)$$

where C is the discharge capacity, n is the number of the cycle, and C_1 is the initial discharge capacity.

- *Coulombic efficiency*: coulombic efficiency (η) is defined as the ratio of the discharge capacity to the charge capacity, expressed as a percentage.

$$\eta = \frac{nQ_d}{nQ_c} x\ 100\% \quad (2.14)$$

2.4 Materials for anodes

Since the technological breakthrough on anode materials at the end of the 1980s and in the early 1990s, resulting in the birth and commercialization of the

lithium ion battery, research on anode materials has been a focus of attention. To the best of our knowledge, however, carbonaceous based materials are the most attractive and widely investigated materials for use as anode in lithium-ion batteries so far.

2.4.1 Carbon-based materials

Carbons are used as the anode in most commercial lithium-ion batteries, because they function as suitable host structures for lithium intercalation and their structures are flexible enough to offer reversibility by allowing effortless insertion and de-insertion of lithium. They also exhibit both higher specific charges and more negative potentials than most metal oxides, chalcogenides, and polymers. Graphite can be obtained in a variety of forms, ranging from a crystalline state to a nearly amorphous state. Carbonaceous materials can be classified into three groups: graphite, graphitizable carbon, and non-graphitized carbons.

Graphite:

Graphite is a classic carbonaceous material that consists of hexagonal sheets of sp^2carbon atoms (called graphene sheets), weakly bonded together by van der Waals forces. Lithium ions and other kinds of ions and molecules can be intercalated between the graphite sheets, and the resulting complexes are called “graphite intercalation compounds” (GIC) [138]. The GICs have an essential characteristic property which is called the staging phenomenon, which governs the intercalated layers that are randomly organized in the matrix of graphite sheets. Lithium intercalation takes place through well-identified, reversible stages, corresponding to

progressive intercalation within discrete graphene layers, to finally attain the formation of LiC_6 with a maximum theoretical capacity of 372 mAh g^{-1} [139]. This process extends to the range of a few mV versus lithium, i.e. well below the decomposition limit of the most common electrolytes. Electrolyte decomposition results in the formation of a surface protective film, the solid electrolyte interphase (SEI), which allows the continuous operation of the carbonaceous anode [140-141].

Graphitizable carbons:

Graphitizable carbons are also called soft carbons. They have a structure composed of misoriented crystallites formed after heat-treatment at high temperature (2000-3000^{o}C) [142-143]. Their reversible capacities are normally lower than that of graphite because their maximum stoichiometric factor x in LiC_6 is typically ~ 0.5 to ~ 0.8 (for graphite, x = 1). The quality of sites capable of lithium accommodation strongly depends on the crytallinity, the microstructure, and the micromorphology of the carbonaceous material [85, 144]. Thus, this kind of carbon determines the current/potential characteristic of the electrochemical intercalation reaction. Their relatively low capacity is mainly due to the lower number of sites available to accommodate lithium in “wrinkled and buckled” defect structural segments.

Non-graphitized carbons:

Non-graphitized carbons are derived from low temperature treatment of organic compounds. Typically, these carbons have a highly disordered structure, a large amount of micro- or nano-porosity, and heteroatoms remaining from the precursors

[145-146]. They deliver much higher capacities than graphite (e.g. 1000 mAh g^{-1} for a coke-type material) [147], but have very high irreversible capacities in the first cycle, with a large hysteresis in the potential profile.

In addition to structural modification of elements, carbon has many different forms or allotropes. The oldest carbon allotropes are amorphous carbon, graphite, and diamond. Later, scientists synthesized new allotropes, including carbon nanotubes (CNTs), fullerenes, and graphene, all of which have had a significant scientific and technological impact. Carbonaceous nanomaterials share the same bonding configuration as macroscopic carbon structures, however, their properties and morphology are controlled by the stability of particular resonance structures rather than their crystalline forms in the bulk [148].

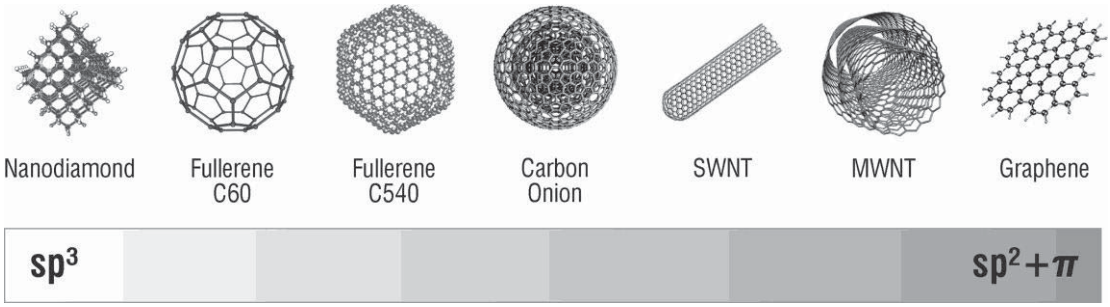

Figure 2.5 Carbon allotropes [148].

Graphite nanosheets are as thermodynamically stable as three-dimensional structures on the nanoscale. The curvature of this planar graphite will generate strain energy, which is compensated by the reduction of unfavourable dangling bonds [149]. Therefore, fullerenes and nanotubes share many of the properties of graphite, but exhibit a distinct and tunable set of properties due to quantum effects on the

nanoscale, enhanced sp^3 character of the bonds, and quantum confinement of wave functions in one or more dimensions [150]. Novoselov et al. [151] discovered the allotrope of carbon which was called graphene in 2004. They used adhesive tape to detach a single layer of atoms from graphite to produce the new allotrope. Graphene consists of a single layer of graphite (Fig. 2.5) with a thickness of one atom and is a good electrical and thermal conductor. Due to the high quality of its sp^2 carbon lattice, electrons were found to move ballistically in a graphene layer, even at ambient temperature [152]. Owing to its large surface-volume ratio and highly conductive nature, graphene may have properties that make it suitable for reversible lithium storage in lithium-ion batteries. This is because lithium ions could be bound on both sides of graphene sheets, as well as on the edges and covalent sites in the graphene. Therefore, it is expected that graphene can overtake its graphite counterpart for enhanced lithium storage. It has been proposed that lithium ions can be absorbed on both side of a graphene sheet, leading to two layers of lithium for each graphene sheet, with theoretical capacity of 744 mAh g^{-1} through the formation of Li_2C_6 [153-154]. Nevertheless, large irreversibility, the absence of a voltage plateau during discharge, and large hysteresis in voltage between charge and discharge currently limit the usage of graphene-based anode materials.

2.4.2 Lithium alloys

The replacement of metallic lithium by lithium alloys has been under investigation since Dey [155] demonstrated the feasibility of the electrochemical formation of lithium alloys in liquid organic electrolytes in 1971. The reaction

usually proceeds reversibly according to the general scheme shown in the equation below:

$$Li_xM \leftrightarrow x\ Li^+ + x\ e^- + M \qquad (2.15)$$

With only a few exceptions (such as hard metals, M = Ti, Ni, Mo, Nb), Li alloys are formed at ambient temperature by polarizing the metal M sufficiently negatively in a Li^+ containing electrolyte. In most cases, even the binary Li-M systems are very complex. Sequences of stoichiometric intermetallic compounds and Li_xM phases with considerable phase ranges are usually formed during lithiation of the metal M, which is characterized by several steps and slopes in the charge-discharge curves. The formation of Li-M phases is in many cases reversible, so that subsequent steps and slopes can also be observed during discharge. Lithium alloys are of great interest, however, due to their high theoretical capacities and also their similar potential range to graphite materials, but unfortunately, the main problem encountered with these alloys is the huge volume change when lithium is either incorporated or removed [156]. As a result, mechanical stress and cracks occur during cycling, which leads to electrochemically inactive particles and thus quite poor cycling stabilities.

Today, the use of lithium alloys as anodic materials in lithium-ion batteries is an interesting field of research, on account of the promising results provided by silicon-based and tin-based compounds. Among all the anode materials, silicon is the most promising candidate, owing to its high natural abundance, low discharge potential, and high theoretical capacity (3579 mAh g^{-1}) [157-158]. The large volume changes (up to 270% for the $Li_{3.75}Si$ phase), however, and the loss of electrical contact during lithium insertion and extraction results in capacity fading [159]. In

recent years, several methods have been examined to attempt to achieve Si anodes with higher reversible capacity with respect to graphite and better capacity retention for practical commercial applications. Reducing the Si particle size to the nanoscale [160-161] or dispersing the electroactive particles in a carbon matrix are the most promising approaches [162-163]. It is believed that carbon based materials buffer the volume changes and improve the electronic and ionic conductivities. However, the initial coulombic efficiency (< 80%) and the capacity retention are still quite low, which hinders commercial application in lithium-ion batteries.

On the other hand, Sn-based materials with high theoretical specific capacity (992 mAh g^{-1}) have been proposed as another type of promising candidate, due to their high theoretical capacity, high packing density, and safe thermodynamic potentials compared to carbonaceous materials for lithium secondary batteries [164-165]. They usually undergo severe structural and volume change, however, during the process of Li uptake and removal, which results in mechanical disintegration of the electrode and consequent capacity fade, greatly limiting the potential for commercialization [165-167]. Much research work has been focused on alleviating the volumetric changes in alloy composite anodes, including the use of intermetallic alloys containing an active or inactive host matrix, such as SnNi [168-169] and SnCu [170-171]. The active metal element can provide the high capacity, while the inactive element is able to buffer the volume change, release the mechanical stress, and thus increase the cycling stability of the electrode. On the other hand, surface-coated/composite SnO_2 has shown better electrochemical performance than the bare material due to the improved solid electrolyte interphase (SEI) layer and/or buffered volume change. Among the buffer materials, carbon has to be considered as the best

choice because of its cheap, light, and conductive nature. To date, carbon coated onto or added into the SnO_2 has been prepared by spray pyrolysis, polymer coating, and afterwards, carbonization and hydrothermal/solvothermal methods. Although the electrochemical performance of these Sn-based alloy composites has been significantly improved, the relatively low cycling stability and the high fabrication cost still make them inadequate for practical use [171-173].

2.4.3 Transition Metal Oxides

Recently, Poizot et al. [174] reported that nanosized 3d transition metal oxides (M_xO_y, where M is Fe, Co, Ni, Cu, or Mn) which are inactive towards Li could be a new class of anode materials for lithium ion batteries. These transition-metal oxides have demonstrated electrochemical capacities over 700 mAh g^{-1} and excellent cycling performances. These oxides with the rock-salt structure have no sites for insertion/de-insertion of Li ions. There is a new mechanism which can be written as:

$$M_xO_y + 2yLi \leftrightarrow yLi_2O + xM \qquad (2.16)$$

During the discharge, the M_xO_y particle is completely disintegrated into highly dispersed metallic nanoparticles (< 10 nm) and a Li_2O matrix, but the global shape of the starting particle is preserved. During the subsequent charge, the Li_2O matrix decomposes, and the M nanoparticles are converted back to M_xO_y nanograins. The existence of this thermodynamically infeasible reaction is attributed to the highly active metallic nanoparticles [61]. An SEI will also be formed during the discharge process, but it can be partially decomposed during the subsequent charge process,

which is attributed to the catalytic activity of metallic nanoparticles [175]. The partially reversible formation/decomposition of the SEI will lead to extra capacity.

2.5 Materials for the cathode

The choice of the cathode material depends on whether we are dealing with rechargeable Li-metal or Li-ion batteries. For rechargeable Li batteries, owing to the use of metallic Li as the anode, the cathode does not need to be lithiated before cell assembly. In contrast, for Li-ion batteries, because the carbon anode is empty (no Li), the cathode must be the source of Li, thus requiring use of air-stable Li based intercalation compounds to facilitate the cell assembly [99]. There is a wide range of materials that can be used as positive electrodes. The best ones are those with little or no structural modification during cycling. Typical insertion or intercalation compounds are therefore preferred candidates. The key criteria for screening potential cathode materials are as follows [176]:

- High free energy of reaction with lithium
- Wide range of amount of lithium ion insertion
- Little structural change upon reaction
- Highly reversible reaction
- Rapid diffusion of lithium within the host lattice
- Good electronic conductivity
- No solubility in electrolyte
- Readily available or easily synthesized from low cost reactants

Here, an overview is provided on selected developments in the area of cathode electrode materials for both Li-ion and Li batteries in the past decade, and

particularly in the past few years. Two major structures of cathode materials reviewed here are the layered structure oxides and the olivines.

2.5.1 Layered structure oxides

Vanadium pentoxide (V_2O_5), one of the most promising cathode materials in lithium metal batteries for many years, offers the advantages of low cost and high theoretical capacity (437 mAh g^{-1}) compared with the commercial cathode material, $LiCoO_2$ (~140 mAh g^{-1}) [38]. Recently, V_2O_5 nanostructures, including nanofibers [177], nanotubes [178-180], nanobelts [70, 181-182], nanorods [183], and nanowires [184-186], has been extensively investigated to improve its electrochemical properties. The aim is to simultaneously reduce the diffusion length for Li^+, enhance the contact surface area between the active materials and the electrolyte, and improve flexibility to accommodate volume change caused by Li^+ insertion/extraction [89]. Limited cycling stability is the major problem in most reports, however, due to the decomposition of electrolyte due to the dissolution of active materials during the charge-discharge cycling process. Although some doping studies have shown improved cycling stability, this will decrease the capacity [187].

Among the known cathode materials for Li battery applications, molybdenum trioxide (MoO_3) is one of the most important energy storage candidates, with high discharge capacity around 300 mAh g^{-1} [188-192]. MoO_3 is also a promising material in gas sensors [193] and as a catalyst for selective partial oxidation in modern industry [194-195]. MoO_3 has three basic polymorphs, i.e., orthorhombic MoO_3, monoclinic MoO_3, and hexagonal MoO_3. As cathode for the Li

battery, orthorhombic MoO_3 has been selected as a strong candidate because this phase is thermodynamically stable [190, 196].

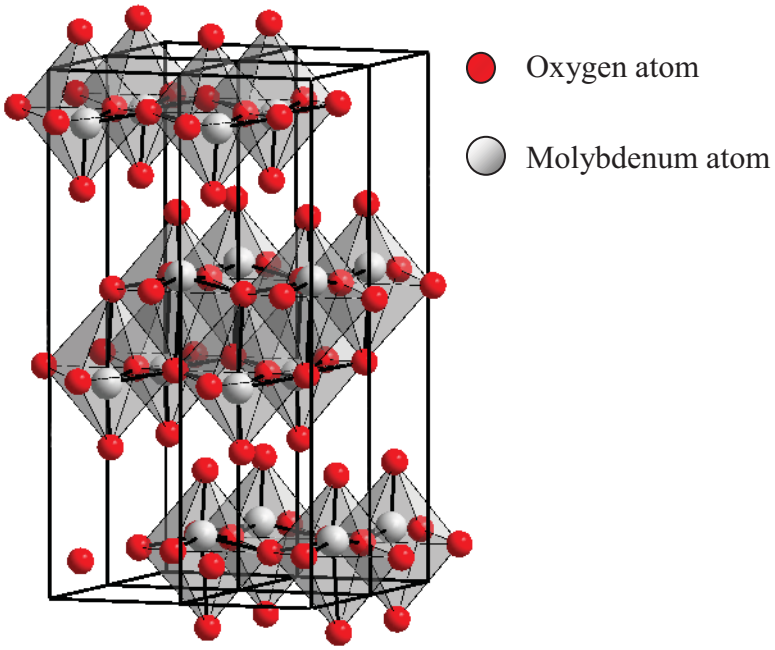

Figure 2.6 3D structure model of MoO_3 in the orthorhombic phase [197].

The orthorhombic MoO_3 phase possesses a unique layered structure: each layer is composed of two sublayers, which are formed by corner-sharing [MoO_6] octahedra along the [001] and [100] directions, and the two sublayers are stacked together by sharing the edges of the octahedra along the [001] direction (Fig. 2.6). The stacking of these layers along the [010] direction by the van der Waals interaction leads to the formation of MoO_3 with a two-dimensional structure, which allows guest atoms and ions (such as Li^+) to be introduced between the layers through intercalation [197]. In terms of practical use in the Li battery, MoO_3 has poor ionic and electronic conductivity [198]. To improve the conductivity of MoO_3, carbon nanotubes [199-

200], graphene [76], or conducting polymer [201-202] could be the best choices of conductive fillers.

2.5.2 Lithium transition-metal oxides

The layered structure lithium transition metal oxides with the general formula $LiMO_2$, with M = V, Co, Mn and Ni, adopt the α-$NaFeO_2$-type structure, which can be regarded as a distorted rock salt superstructure [203-206]. In a cubic close-packed oxygen array, the lithium and transition-metal atoms are distributed in the octahedral interstitial sites, in such a way that MO_2 layers are formed, consisting of edge-sharing [MO_6] ocatahedra. In between these layers, lithium resides in ocatahedral [LiO_6] coordination, leading to alternating (111) planes of the cubic rock salt structure. The layered framework provides a two dimensional path, which allows for relatively facile extraction and insertion of lithium ions. Fig. 2.7 shows the layered structure of $LiCoO_2$, $LiNiO_2$ and $LiMnO_2$. $LiCoO_2$ is the most popular cathode materials, owing to the convenience and simplicity of preparation [207]. The Li_xCoO_2 ($1 > x > 0.5$) system has been studied extensively and exhibits excellent cyclability at room temperature. The specific capacity of $LiCoO_2$ is limited to the range of 137 to 140 mAh g^{-1}, although the theoretical capacity is 273 mAh g^{-1} [208]. Despite the commercial success of $LiCoO_2$, it has several drawbacks than other transition metals [52-53].

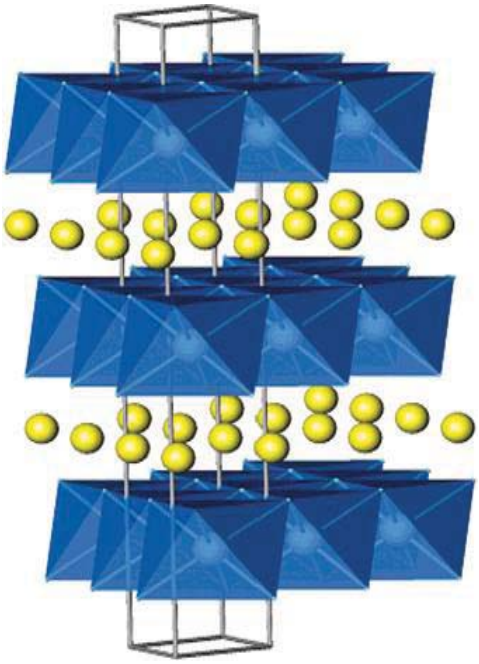

Figure 2.7 Layered structure of $LiCoO_2$, $LiNiO_2$, and $LiMnO_2$, showing the lithium ions between the transition-metal oxide sheets [209].

$LiNiO_2$ was first proposed by Dahn et al.[210] as an alternative to $LiCoO_2$ because of its lower cost, higher reversible capacity (~200 mAh g^{-1}), and lower toxicity, but $LiNiO_2$ suffers from structural changes, thermal runaway and difficulties in synthesizing it [55-56]. From an environmental point of view, layered $LiMnO_2$ is a very attractive material for cathode; however, layered $LiMnO_2$ is a metastable phase. Therefore, it is not possible to synthesize it via the conventional solid-state method used to make its layered Co or Ni analogues. Some research groups [211-212] have reported the preparation of layered $LiMnO_2$ via ion exchange, but layered $Li_{0.5}MnO_2$ is converted into the $LiMn_2O_4$ spinel structure during cycling, resulting in poor electrochemical properties.

2.5.3 Olivines

Iron-based compounds that contain compact tetrahedral "polyanion" structural units, $(XO_4)^{n-}$ (X = S, P, As, W, or Mo), have been investigated intensively as potential cathode materials for lithium ion batteries. Among the various polyanion compounds, the olivine structure has the most extensive interconnections of octahedra, with the cations that occupy the M2 site (Fe site in $LiFePO_4$) forming a corner-sharing network of octahedra in the (0 1 0) plane, with the cations on the M1 (Li) site forming edge-sharing chains of octahedra in the [100] direction (Fig. 2.8) [213].

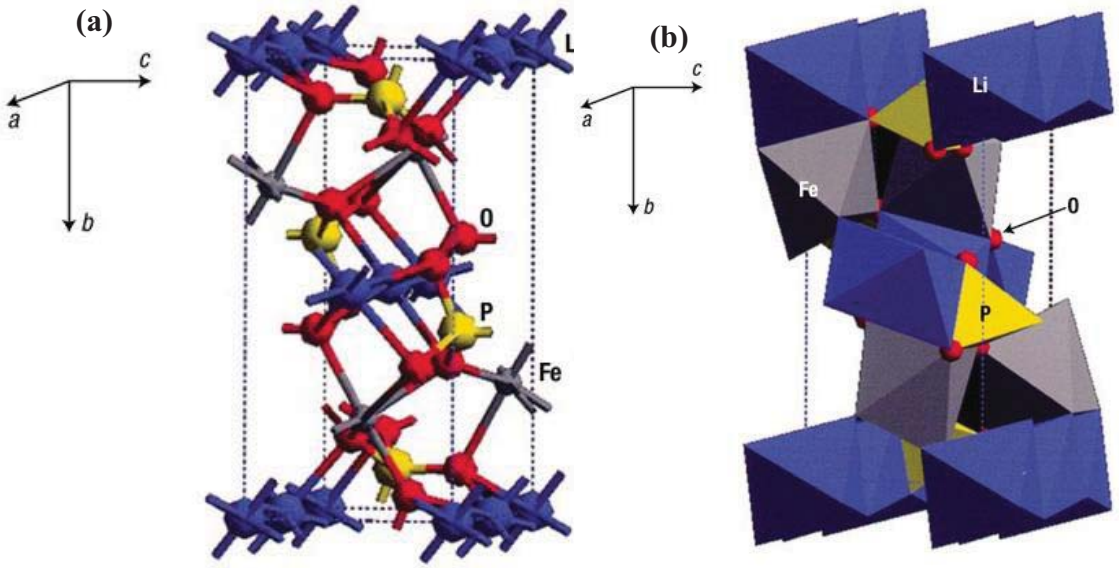

Figure 2.8 Ball-stick model of ordered-olivine structure of $LiFePO_4$ (a); model of polyhedral connectivity, depicting the corner-sharing network and edge-sharing chains of octahedra (b) [179].

$LiFePO_4$ has become the object of great interest as an active material for storage cathodes in rechargeable lithium batteries because of its high energy density, the low cost of its raw materials, its environmental friendliness, its high thermal stability in the fully charged state, and its greater safety compared to conventional materials [99]. $LiFePO_4$ has a high lithium intercalation voltage (~3.5 V relative to lithium metal) and no obvious capacity fading, even after several hundred cycles. Its capacity approaches 170 mAh g^{-1}, which is higher than the 140 mAh g^{-1} of $LiCoO_2$. In practice, the full capacity of the material cannot be obtained due to its low electrical conductivity (10^{-9} to 10^{-10} S cm^{-1}). $LiFePO_4$ electrodes are actually composed of two separate phases, $LiFePO_4$ and $FePO_4$, which are both poor electronic conductors because they each contain Fe cations with just one oxidation state (2^+ or 3^+, respectively); as a result, this material has been largely ignored. Therefore, in order to obtain acceptable energy and power from the lithium cells, it is necessary to use small $LiFePO_4$ particles, coated or in intimate contact with electronically conductive carbon [60]. This simultaneously reduces the distance for Li^+ transport and increases the electronic contact between the particles. Procedures of this kind have led to a greatly improved electrochemical response, and the full capacity of the material is now accessible. The long term cycling stability at high current rate is still a great challenge for this material, however, as it is a compulsory requirement for lithium ion batteries to have long cycle life for EV/HEV application. Apart from carbon, conducting polymer (polypyrrole) was also proposed as a good conductive matrix for $LiFePO_4$ particles, and it also showed excellent mechanical properties [214]. Olivine $LiMnPO_4$, on other hand, which is isostructural with $LiFePO_4$, has a similar theoretical electrochemical capacity (170 mAh g^{-1}) and shows a higher voltage of 4.1

vs. Li^+/Li[215]. To date, a few promising reports on the electrochemistry of this compound have been published. Unfortunately, $LiMnPO_4$ has low intrinsic electronic and ionic conductivity and hence a poor discharge rate capability. The electrochemical performance is especially poor at high current density, which is attributed to the slow lithium diffusion kinetics within the grain and the low intrinsic electronic conductivity [216]. Thus far, several researchers have made efforts to enhance its electrochemical properties by particle-size reduction [217], cation doping [218] and carbon coated $LiMnPO_4$ [219].

2.6 Polymer-based solid and gel electrolytes

Polymer electrolytes or ion-conducting polymers have attracted many researchers due to their vast applications in the development of ionic devices in the solid state. These kinds of materials have useful chemical and mechanical properties that allow ease of fabrication in thin film form at desired sizes. They also have the ability to form proper electrode-electrolyte contact [220]. Various type of polymer films have been developed using various methods, such as casting from a polymer solution [221], evaporation methods [222], and in situ plasma polymerization techniques [223]. The electrolyte materials must show high ionic conductivity and be dimensionally stable, since the electrolyte will also act as the separator in the battery system. A polymer electrolyte with a high cationic transport number is also important because a concentration gradient caused by the mobility of both cations and anions in the electrolyte arises during discharging, which may result in premature battery failure [224]. Basically, polymer electrolytes can be classified into the following categories [66, 220].

- *Solid polymer electrolytes (SPEs)*

In SPEs, the polymer host itself is used as a solid solvent along with an Li salt and does not contain any organic liquids. The SPEs suffer from poor ionic conductivities (10^{-5} S cm^{-1} at 20^{o}C), but are safer due to the absence of any organic solvent which can cause environmental hazards. SPE films can be prepared either using the solution cast technique [225-227] or the hot-press technique [228-229].

- *Plasticized solid polymer electrolytes*

This polymer is modified from the SPE type by adding plasticizers such as ethylene carbonate (EC), propylene carbonate (PC), poly(ethylene glycol) (PEG), and dibutyl phthalate (DBP). Such an addition not only decreases the degree of crystallinity, but also increases the segmental motion of the polymer chain. Such electrolytes also support ion dissociation, resulting in greater numbers of migrating ions for charge transport.

- *Gel polymer electrolytes (GPEs)*

GPEs are also known as hybrid polymer electrolytes, which are formed by trapping liquid electrolytes in a polymer matrix. The advantage of this type of electrolyte is that higher ionic conductivity can be obtained as compared with SPEs. The ion conduction in these electrolytes takes place through the liquid electrolyte, with the host polymer mostly providing the structural support. Unfortunately, a loss of mechanical properties is observed in GPEs, and liquid electrolytes tend to provoke undesired interfacial reactions of the GPEs with electrodes during cell operation

[230-231]. This may induce vigorous proliferation of a resistive layer on the electrodes, which hinders ionic transport at the interface of the GPEs and the liquid electrolyte.

- *Composite polymer electrolytes (CPEs)*

More attention has been focused on CPEs, wherein nanosized fillers are added to the SPEs. It has been reported that the addition of nanosize fillers, such as zeolites, super-acid sulfonated zirconia, alumina (Al_2O_3), silica (SiO_2), and titania (TiO_2), not only improve the transport properties, but also the mechanical and electrochemical properties of the SPEs [232-233].

There are numerous polymers that have been developed, such as poly(ethylene oxide) (PEO) [234-236], poly(acrylonitrile) (PAN) [237-238], poly(vinylchloride) (PVC) [239-240], poly(methyl methacrylate) (PMMA) [241-242], and poly(vinylidenedifluoride) (PVDF) [243-244].

PVDF as a host has drawn the attention of many researchers due to its excellent mechanical properties, high chemical resistance, good thermal stability, and high piezoelectric and pyroelectric coefficients [245]. PVDF also exhibits high anodic stability and a high dielectric constant (ε_r = 8.4), which promotes greater ionization of lithium salts [246], and strongly electron-withdrawing fluorine atoms (-C-F). Watanabe et al. [247] have reported that PVDF can form homogeneous SPE films with a lithium salt, along with EC and/or PC, in the proper compositions. In later studies, Chiang et al. [248] revealed that the ionic conductivity of PVDF/$LiPF_6$ gel polymer electrolyte was enhanced by three orders of magnitude by plasticization

with EC/PC solution, when compared with PVDF solid polymer electrolyte. Such an improvement in ionic conductivity can be explained by the conduction mechanism in PVDF gel polymer electrolyte, which is associated with swollen polymer network chains via EC/PC molecules, which also form a solid amorphous polymer region.

Although PVDF-type polymers are already being used as solid/gel polymer electrolytes, their poor electrolyte uptake is still a major problem for practical application due to their high crystallinity [114]. The crystallinity of semi-crystalline polymers can be readily controlled by varying the type and content of co-monomers. The presence of ~12% hexafluoropropylene (HFP) in PVDF solution increased their electrolyte uptake up to 60% , which helps to maintain good mechanical/elastic properties and high ionic conductivity [249]. Several PVDF copolymers have been identified as possible candidates for solvent casting of self-supporting electrode and separator films, thereby bypassing the need for cross-linking agents.

2.7 Flexible lithium ion batteries

Recently, the trends in modern electronic devices have led them to become smaller, thinner, and more flexible. The current liquid-electrolyte Li-ion technology is not compatible with these requirements. To ensure a long-lasting success for the Li-ion technology, its evolution from liquid to solid/plastic must be achieved [114]. Rechargeable polymer Li batteries could provide shape flexibility. Such a thin, flexible battery technology, which offers shape versatility, flexibility, and lightness, has many potential advantages in the continuing trend towards electronic miniaturization [250]. Various techniques to fabricate and prepare flexible lithium battery have been developed. A key factor or enabling element in this type of battery

is the substrate/matrix used in both the electrodes and the separator. There has been extensive research on the physical and electrochemical properties of gel polymer as a candidate for the substrate, but comparatively little research on practical polymer batteries actually using gel polymer. In 1996, Tarascon and his group in Bellcore introduced the first practical flexible/plastic lithium battery [114]. The concept of this flexible lithium battery is that polymer/plastic is used as the matrix or substrate for both electrodes and as the separator. The flexible/plastic Li-ion cell consists of five components: a copper current collector, a carbon-based negative electrode laminate, a plastic electrolyte/separator, a positive electrode laminate containing $LiMn_2O_4$ powders, and an aluminium current collector. Both electrodes and the separator were prepared by solvent casting and contain the same copolymer (PVDF-HFP), plus dibutyl phthalate (DBP) as a constituent. The performance of such a flexible battery compares favourably in terms of gravimetric or volumetric energy density and cycle life, as well as power rate and self-discharge, with its liquid counterparts, while having enhanced safety characteristics, higher shape flexibility, and greater scalability. With a view to smart textile application, a flexible and stretchable Li-ion battery was analogously produced based on a mixing and drying process using a strain-free $LiFePO_4$ cathode, a $Li_4Ti_5O_{12}$ anode, and a solid polyethylene oxide (PEO) electrolyte as the matrix for both electrodes and as a separator layer [251]. Due to solid thermoplastic electrolyte (PEO) as a key enabling element, this battery is potentially extrudable or drawable into fibres or thin stripes which are directly compatible with the weaving process used in smart textile fabrication. In light of the fact that commercial cathode materials are fabricated at high temperature, however, polymers do not offer facile electrode fabrication, since

they rapidly degrade at relatively low temperature. Also, poor adhesion with oxide materials would be problematic during long-term battery cycling.

Flexible Li-ion batteries based on nanoporous cellulose paper embedded with aligned carbon nanotube electrode as cathode and a thin evaporated Li-metal layer as anode, with Al foil on both sides as current collectors [75], could offer an alternative approach to the design of flexible lithium batteries where aqueous 1 M $LiPF_6$ in ethylene carbonate and dimethyl carbonate (1:1 vol/vol) is used as the electrolyte (Fig. 2.9 (a)). Despite a large irreversible capacity (~430 mAh g^{-1}) in the initial charge-discharge cycle, the flexible lithium battery device can be operated with full mechanical flexibility and delivers a reversible capacity of 110 mAh g^{-1}. To meet the great challenge in the design of flexible storage device, researchers have proposed a new structure for a thin and flexible Li-ion battery, using paper as the separator and free-standing carbon nanotube thin films for both current collectors [252] (Fig. 2.9(b)). The current collectors and Li-ion battery materials are integrated onto a single sheet of paper through a lamination process. The rechargeable Li-ion paper battery, despite being thin (~300 μm), exhibits both robust mechanical flexibility (capable of bending down to < 6 mm) and high energy density (108 mWh g^{-1}). It is still a great challenge, however, to fabricate flexible/bendable energy storage devices due to the lack of reliable electrode materials that combine both superior electronic conductivity and mechanical flexibility, but also possess high stability in electrochemical environments.

Flexible Li-ion rechargeable batteries based on free-standing carbon nanotube (CNT) composite [77, 253-254] electrode and graphene composite paper [255-256] electrode have been proposed.

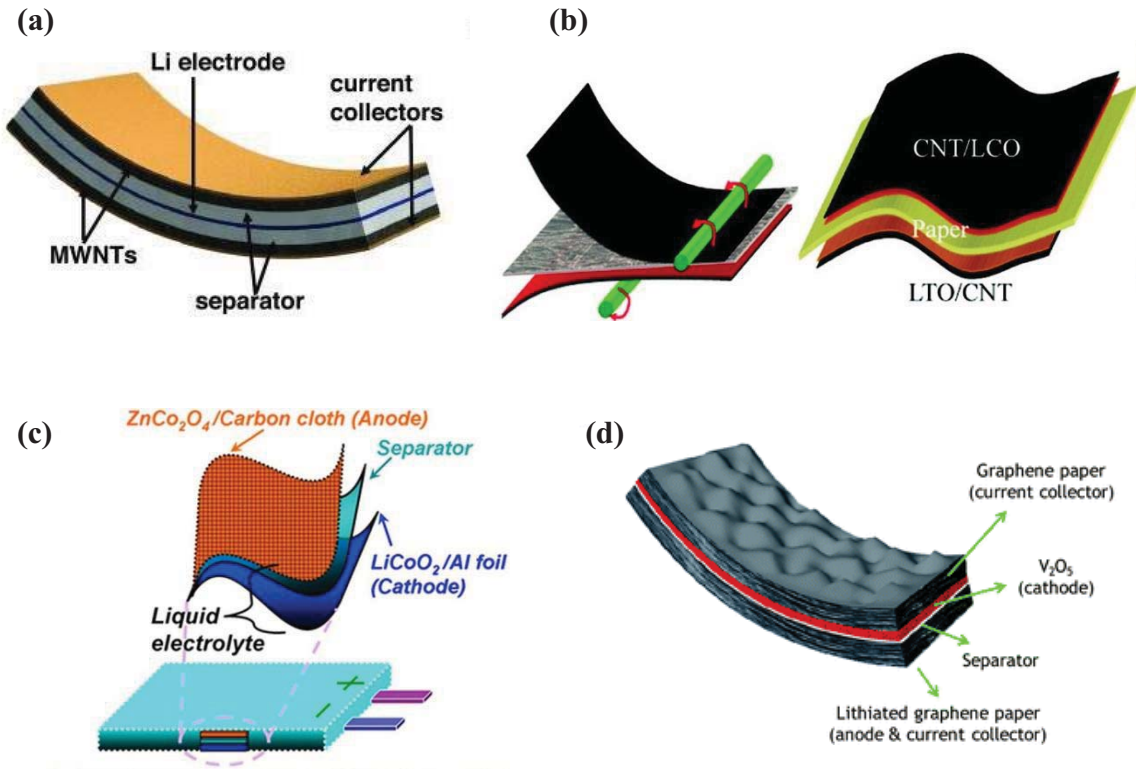

Figure 2.9 Schematic of cell construction and fabrication process for flexible Li-ion battery: (a) Three-terminal hybrid energy device with CNTs embedded in cellulose paper as separator and solid electrolyte [75]. (b) Lamination process where the free-standing film is laminated on paper with a rod and the final paper Li-ion battery device with both $LiCoO_2$ (LCO)/CNT and $Li_4Ti_5O_{12}$ (LTO)/CNT laminated on both sides of the paper substrate [252]. (c) Structure of a flexible Li-ion battery composed of hierarchical 3D $ZnCo_2O_4$ nanowires/carbon cloth/liquid electrolyte/$LiCoO_2$ [257]. (d) Flexible Li battery based on graphene paper [76].

CNTs and graphene paper are functional materials, which do not only act as conducting agents, but also as a current collectors, so that CNT or graphene-based

flexible electrode can be applied to both the cathode and the anode. For the anode, silicon [77, 256, 258], CuO_2 [259], Fe_2O_3 [260], or $ZnCo_2O_4$ [257] (Fig. 2.9(c)) may be chosen to be deposited or combined with CNTs or carbon-based flexible materials. For the cathode, V_2O_5 is generally selected as the active material to interpenetrate the network structure of CNTs [200, 261] and because it can also be deposited onto the surface of graphene paper by employing the pulsed laser deposition (PLD) technique [76] (Fig. 2.9(d)). Direct growth of $LiMn_2O_4$/CNT [262] via the *in situ* hydrothermal method also has been reported to have good reversible capability and cycling stability as a candidate for the flexible cathode material.

All the reports on CNT and graphene-based flexible electrode very nicely show that the use of CNT and graphene composite paper can result in a significant improvement on the device level. The energy density of this type of carbon-based charge storage system would be of great interest for applications where other devices cannot be used, e.g. due to the demands for flexibility, conformability, and environmental friendliness.

Chapter 3

Experiment

3.1 Experimental procedures

Overall experimental procedures during this PhD research work can be classified into three major parts: the first part is the preparation of nanostructures/composite materials and their physical characterization using different instrumental analysis techniques; the second part is the fabrication of free-standing electrode film and assembly techniques for flexible and bendable cells, and the third part is electrochemical characterization involving the application of active nanostructured/composite materials as electrode for use in lithium-ion batteries. All these experimental procedures for the PhD research work are shown in Fig. 3.1.

3.2 Synthesis of nanostructured/composite materials

The electrochemically active nanostructure/composite materials used in this study were prepared via different methods and techniques. In this section, the methods and procedures used in preparing the electrochemically active materials are discussed in detail.

3.2.1 Hydrothermal method

The hydrothermal method is categorized as a low temperature method and includes the various techniques of crystallizing substances from high-temperature aqueous solutions at high vapor pressures. Hydrothermal synthesis can be defined as a method for synthesis of minerals in hot water under high pressure.

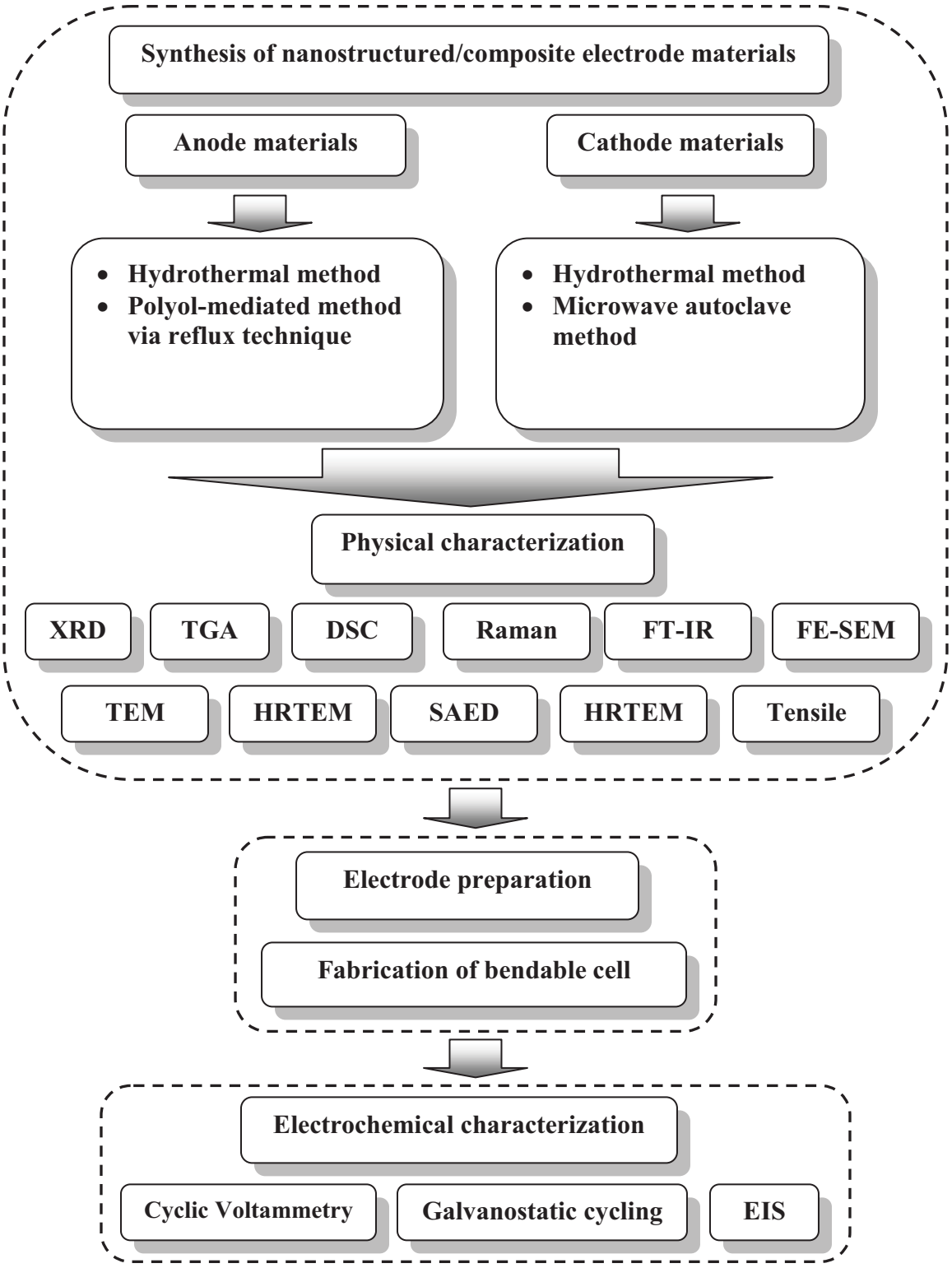

Figure 3.1 Overview of experimental procedures.

The hydrothermal autoclaves used in this PhD work are 4748 acid digestion bombs with 125 ml capacity from the Parr Instrument company as shown in Fig. 3.2. The outer parts are made of stainless steel with six cap screws to seal the polytetrafluoroethylene (PTFE) cup. An expandable spring disk maintains continuous pressure on the seal during the cooling cycle, when the PTFE cup might relax and leak. The temperature can reach up to 250^{o}C and the pressure up to 1900 psi. In a typical experiment, the precursor solution was transferred to the PTFE cup, filling it up to 60% of the whole volume, and the autoclave was then kept in a conventional oven for the preset time and temperature. This hydrothermal technique has been extensively used in crystal growth and nanomaterials synthesis. The factors affecting the product in terms of composition, morphology, and crystal structure mainly include the volume of the solvent, which is related to the pressure, the concentration of the precursor, the temperature, and the use of a surfactant. To achieve desired materials with desired morphology and crystal structure, all the parameters need to be further investigated.

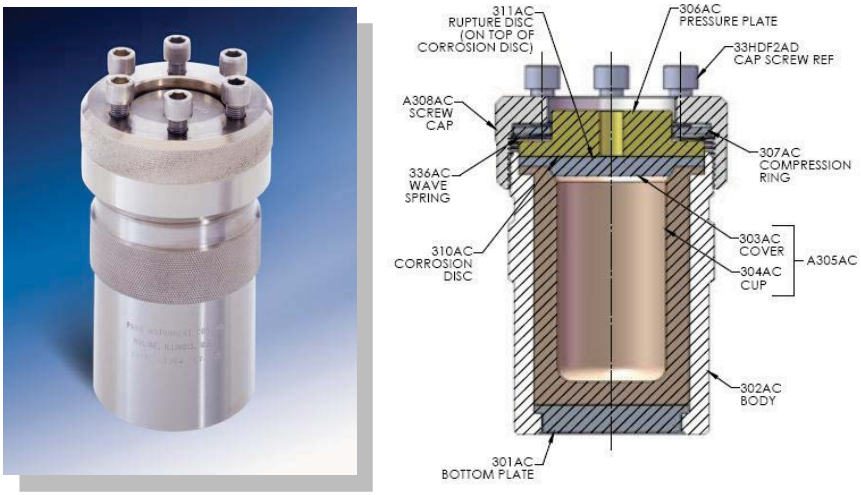

Figure 3.2 Acid digestion bomb 4748 from Parr Instruments (left) with a cross-sectional view (right).

3.2.2 Microwave hydrothermal method

The fundamental procedures of the microwave hydrothermal method are similar to those of the conventional hydrothermal method. In the microwave hydrothermal method, however, microwave irradiation is applied as the source of heat, while the conventional hydrothermal method uses heat from an electric oven. Microwaves act as high frequency electric fields and will generally heat any material containing mobile electric charges, such as polar molecules in a solvent or conducting ions in a solid [263]. Polar solvents are heated as their component molecules are forced to rotate with the field and lose energy in collisions. Semiconducting and conducting samples are heated when ions or electrons within them form an electric current and energy is lost due to the electrical resistance of the material [264]. Microwave heating in the laboratory began to gain wide acceptance following the publication of related papers in 1986 [265], although the use of microwave heating in chemical modification can be traced back to the 1950s. Microwave heating makes it possible to heat the target compounds without heating the entire furnace or oil bath, which saves time and energy. It is also able to heat sufficiently thin objects throughout their volume (instead of through their outer surface), in theory, producing more uniform heating. The microwave oven used in this PhD work is a MicroSYNTH microwave system (Milestone) controlled by a Labthermal 800 controller. It has a frequency of 2.45 GHz and the maximum power reaches up to 500 Watt, as shown in Fig. 3.3. The microwave oven is equipped with a 45 mL PTFE vessel where reactions can take place at temperatures up to 250^{o}C and pressures up to 40 bar. The vessel is housed in a safety shield which features built-in-pressure control through a preloaded spring with a vent and resealing mechanism. In

typical procedure, the precursor solution was transferred into the PTFE lined digestion vessel and fitted with a pressure and temperature probe. The sealed vessels were placed inside the microwave oven at preset power, time, and temperature.

Figure 3.3 MicroSYNTH microwave system (Milestone) with a frequency of 2.45 GHz controlled by a Labthermal 800 controller.

3.2.3 Polyol-mediated method

The basis of this method is the precipitation of a solid while heating sufficient precursors in a multivalent and high-boiling point alcohol (e.g., diethylene glycol (DEG), boiling point ~246 ^{o}C) [266]. The alcohol itself acts as a stabilizer, limiting particle growth and preventing agglomeration. Due to the high temperatures that can be applied (> 150 °C), often highly crystalline oxides are yielded. Moreover, the synthesis is easy to perform and can be scaled up accordingly. Beside oxides, a variety of materials, including sulfides, phosphates, and elemental metals have been

produced under very similar experimental conditions [267]. In a typical procedure for the polyol-mediated method, the solution is dissolved in high-boiling point alcohol, and the solution is placed in a round-bottomed flask (Fig. 3.4). The solution is then heated in an oil bath at > 150 °C for 3-5 h under continuous reflux in air. Magnetic stirring is applied throughout the entire synthesis. The reaction can be easily followed through its distinctive color changes. During cooling in air, the magnetic stirring is stopped. The solution is then diluted with acetone (up to 5 times by volume) to remove the excess solvent. The solution is then washed and centrifuged in order to recover most of the precipitate.

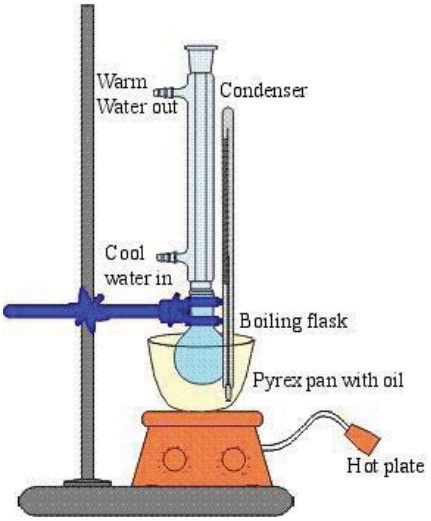

Figure 3.4 Reflux equipment for polyol-mediated process[268].

3.3 Physical and structural characterization of nanostructured/composite materials

Physical and structural investigation of the synthesized nanotructured/composite electrode materials was conducted using the techniques

described below. The equipment belongs to both our institutes, the Institute for Superconducting and Electronic Materials (ISEM) and the Intelligent Polymer Research Institute (IPRI) under the Australian Institute for Innovative Materials (AIIM).

3.3.1 X-ray Diffraction (XRD)

X-ray diffraction (XRD) is a non-destructive testing method used to characterize the crystallographic structure, crystallite size (grain size), and preferred orientation in polycrystalline or powdered solid samples. The samples can be reused for other tests after XRD measurements. The X-rays are scattered by each set of lattice planes at a characteristic angle, and the scattered intensity is a function of the arrangement of atoms in the crystal. The scattering from all the different sets of planes results in a pattern, which is unique to the crystal structure of a given compound. The X-rays are generated in X-ray tubes when the anode material (usually copper) is irradiated with a beam of high-energy electrons that are accelerated by a high voltage electric field to a very high speed. In addition, photons with energies characteristic of the target materials are emitted. A monochromator is used that preferentially suppresses photons with other energies from the desired characteristic one. The X-rays produced are directed to the sample being studied, and X-rays with a wavelength in the range of 10 to 0.01 nanometers, which is on the order of the lattice spacing, are elastically diffracted from the atomic planes in the crystalline material. Re-emitted X-rays interfere, giving constructive or destructive interference. Bragg's law (Eq. 3.1) describes the diffraction condition from planes with spacing, *d*:

$$n\lambda = 2d\sin\theta \quad (3.1)$$

where d is the distance between atomic layers in a crystal, λ is the wavelength of the incident X-ray beam, n is an integer, and θ is the angle of incidence experienced by the X-ray beam reflection from the faces of the crystal. Fig. 3.3 illustrates the interference between waves scattered from two adjacent planes of atoms in a crystal. In this PhD study, only X-ray powder diffraction was used. The powder sample is loaded into a small disc-shaped sample holder with a flattened surface. The sample holder is put on one axis of the diffractometer and tilted by an angle θ, while a detector rotates around it on an arm at a 2θ angle. This configuration is known under the name Bragg-Brentano. Each crystalline solid produces a distinctive diffraction pattern. Both the positions (corresponding to lattice spacings) and the relative intensities of the lines act to characterize the "fingerprint" for the material. In addition to identifying crystalline phases, X-ray diffraction can also be used to determine the crystal size. This can be obtained from the broadening of the peaks according to the Scherrer formula (Eq. 3.2):

$$\beta(2\theta) = \frac{K\lambda}{Lcos\theta} \quad (3.2)$$

where L is the crystal size (nm), λ is the X-ray wavelength (Å), K is the shape factor of the average crystallite (with a typical shape factor around 0.9), β is the full width at half maximum (FWHM) in radians, and θ is the peak position (^{o}). XRD patterns

were collected in a 2θ configuration using a GBC MMA 017 diffractometer (Cu Kα radiation, λ = 1.5418 Å).

3.3.2 Thermogravimetric analysis (TGA)

Thermogravimetric analysis or thermal gravimetric analysis (TGA) is a type of investigation performed on samples that determines changes in weight in relation to changes in temperature. In this doctoral work, TGA was used to determine the amount of amorphous carbon and multiwall carbon nanotubes (MWCNTs) in the composite materials. A Mettler-Toledo thermogravimetric analysis/differential scanning calorimetry (TGA/DSC) 1 star^{e} system was employed. Samples could be heated up to 1000 ^{o}C in air or high purity argon, with a typical heating rate of 5-10 ^{o}C per min. The container for the sample is made of alumin,a and the loading mass of a sample is generally 2-20 mg, depending on the density of the sample.

3.3.3 Raman spectroscopy

Raman spectroscopy is a spectroscopy technique based on inelastic scattering of monochromatic light, usually from a laser source. Inelastic scattering means that the frequency of photons in monochromatic light changes upon interaction with a sample. Photons of the laser light are absorbed by the sample and then re-emitted. The frequency of the re-emitted photons is shifted up or down in comparison with the original monochromatic frequency, which is called the Raman effect. This shift provides information about vibrational, rotational, and other low frequency transitions in molecules. Typically, a Raman system consists of four components,

including the excitation source (laser), the sample illumination system and light collection optics, the wavelength selector filter (filter or spectrophotometer), and the detector, a photodiode array, charge-coupled device (CCD), or photomultiplier tube (PMT). A sample is normally illuminated with a laser beam in the ultraviolet (UV), visible (Vis), or near infrared (NIR) range. Scattered light is collected with a lens and delivered through an interference filter to yield the Raman spectrum of a sample. Here, Raman spectra were recorded using a JOBIN Yvon Horiba Raman spectrometer model HR 800 from Horiba Ltd, France, employing a 10 mW helium/neon laser at 623.8 nm with diode laser excitation on a 300 lines mm^{-1} grating, which was filtered by a neutral density filter to reduce the laser intensity, and a charge-coupled detector (CCD). This Raman system was provided by the Intelligent Polymer Research Institute (IPRI), and spectroscopy was performed with the kind collaboration of Chong Zhao, a PhD student from ISEM.

3.3.4 Fourier transform infrared (FTIR) spectroscopy

Fourier transforms infrared (FTIR) spectroscopy is the preferred method for identifying types of chemical bonds in a molecule by producing an infrared (IR) absorption spectrum that is like a molecular fingerprint. In FTIR spectroscopy, IR radiation is passed through a sample. Some of the infrared radiation is absorbed by the sample, and some of it is passed through (transmitted). The resulting spectrum represents a pattern of molecular absorption and transmission, which is characteristic of the chemical bonds in the sample. By interpreting the infrared absorption, the chemical bonds in the molecule can be determined. There are two common forms of sample preparation for FTIR measurements. In the first, a fine powder is dispersed in

a liquid such as mineral oil (Nujol) to form a paste. In the second, the fine powder is mixed with potassium bromide (KBr), transferred to a die that has a barrel and pressed. For the second method, the ratio between sample and the KBr should be high enough to obtain a good and correct spectrum. In this PhD work, the FTIR spectroscopy analysis was carried out using a Shimadzu IRPrestige-21 model.

3.3.5 Tensile testing

Tensile testing, also known as tension testing, is a fundamental materials science test in which a sample is subjected to uniaxial tension until failure [269]. The results from the test are commonly used to select a material for an application, for quality control, and to predict how a material will react under other types of forces. Properties that are directly measured via a tensile test are ultimate tensile strength, maximum elongation, and reduction in area [270]. From these measurements the following properties can also be determined: Young's modulus, Poisson's ratio, yield strength, and strain-hardening characteristics. The mechanical properties of the free-standing films were investigated with a Shimadzu EZ-S Universal Testing Machine. Tensile tests were conducted under a fixed stretching speed of 1 mm min^{-1} for all specimens. The specimens were 5 mm in width and 30 mm in length.

3.3.6 Scanning electron microscopy (SEM) and energy-dispersive X-ray (EDX) spectroscopy

Scanning electron microscopy (SEM) is used primarily to observe the morphology of powder samples or an electrodes's surface topography. During the

SEM measurements, the sample is bombarded with a scanning beam of electrons. The electrons interact with the atoms that make up the sample, producing signals that contain information about topography, composition, and other properties of the sample surface, such as electrical conductivity. The types of signals produced by SEM include those from secondary electrons, back-scattered electrons (BSE), characteristic X-rays, specimen currents, and transmitted electrons. Secondary electron detectors are common in all SEM systems. The signals result from interactions of the electron beam with atoms at or near the surface of the sample. Secondary electron imaging (SEI) allows one to observe the surface of a sample. Field-emission scanning electron microscopy (FE-SEM, JEOL JSM-7500FA, 15 kV) was used to observe the morphology of the materials or electrodes. X-rays, which are produced by the interaction of electrons with the sample, can also be detected in an SEM equipped with an energy-dispersive X-ray (EDX) spectrometer to obtain the elemental composition of a sample. The powder sample was either dispersed in ethanol or directly loaded onto an aluminum holder using carbon conductive tape for SEM observation. A sample for EDX was loaded onto a piece of indium metal to eliminate contamination from the sample holder and the carbon tape. All FE-SEM measurements were carried out at ISEM.

3.3.7 Transmission electron microscopy (TEM)

Transmission electron microscopy (TEM) is a microscopy technique whereby a beam of electrons is transmitted through an ultra-thin specimen, interacting with the specimen as is passes through. An image is formed from the interaction of the electrons transmitted through the specimen; the image is magnified and focused onto

an imaging device, such as a fluorescent screen, a layer of photographic film, or a sensor such as charge-coupled device (CCD) camera. TEM is capable of imaging at a significantly higher resolution than light microscopes, owing to the small de Broglie wavelength of electrons. TEM can be used to observe morphology, crystal structure, and electronic structure. Selected area electron diffraction (SAED) is a crystallographic experimental technique that can be performed inside a transmission electron microscope. A thin crystalline specimen is subjected to a parallel beam of high-energy electrons. As the electrons pass through the sample, electrons behave in a wave-like, rather than a particle-like manner. Because the wavelength of high-energy electrons is a fraction of a nanometer and the spacings between atoms in a solid are only slightly larger, the atoms act as a diffraction grating for the electrons. That is, some fraction of the electrons will be scattered to particular angles, as determined by the crystal structure of the sample, while others continue to pass through the sample without deflection. As a result, the image on the screen of the TEM will be a series of spots, with each spot corresponding to a satisfied diffraction condition of the sample's crystal structure. If the sample is tilted, the same crystal will stay under illumination, but different diffraction conditions will be activated and different diffraction spots will appear or disappear. TEM investigations were performed using a 200 kV JEOL 2011 instrument, with a JEOL-Energy dispersive X-ray spectroscopy (EDS) detector and a JEOL EDS software analysis system. TEM samples were prepared by deposition of ground particles onto holey/lacey carbon support films. Most of the TEM measurements in this research work were performed with the kind collaboration of Dr. David Wexler from the Faculty of Engineering, University of Wollongong.

3.4 Electrode preparation and cell assembly technique

3.4.1 Electrode preparation of powder samples

The working electrodes for lithium-ion batteries were prepared by mixing nanostructured/composite active materials with 10-20 wt.% acetylene black (AB) and 5-10 wt.% polyvinylidene fluoride (PVDF) or sodium carboxymethyl cellulose (CMC) in a solvent, consisting of either N-methyl-2-pyrrolidone (99.5%, Aldrich) or water, respectively. The slurry was uniformly pasted onto pieces of Cu (anode) or Al (cathode) foil with an area of 1 cm^2. The typical active mass loading of the electrodes was 1-3 mg cm^{-2}, depending on the density of the electrochemically active samples. Subsequently, the coated electrodes (average thickness of ~ 50 μm) were dried in a vacuum oven at 90-120^oC for 24 hrs. The electrode was then either pressed under a pressure of approximately 3000 kg cm^{-2} for 10 s to enhance the contact between the electrochemically active materials and the conductive carbon black, or used without pressing, depending on the materials.

3.4.2 Electrode preparation of film or paper-like samples

In this PhD work, a modified vacuum filtration technique was adopted [271] to make uniform films or papers as working electrodes, in which a 300 ml filter funnel (Glasco) was used. The most important factor in this procedure is the morphology of the active materials. Nanowire, nanobelt, and nanotube structures with a high ratio between diameter or thickness and the length of the nanostructured materials are mostly preferred and considered in preparing this type of electrode. In a typical procedure, 2 mg/ml of nanostructure material was dispersed into 50 ml of

distilled water. Then, the as-prepared suspension was poured into the funnel and filtered through a porous polyvinylidene fluoride (PVDF) membrane (Millipore, 0.22 μm pore size, 47 mm in diameter) by positive pressure from a vacuum pump (Fig. 3.5). Since the solvent can pass through the pores of membrane, the nanostructure material is trapped on the membrane surface, forming a mat. The resultant mat with its PVDF membrane was then dried in an oven for 2 hours and was peeled off from the PVDF membrane.

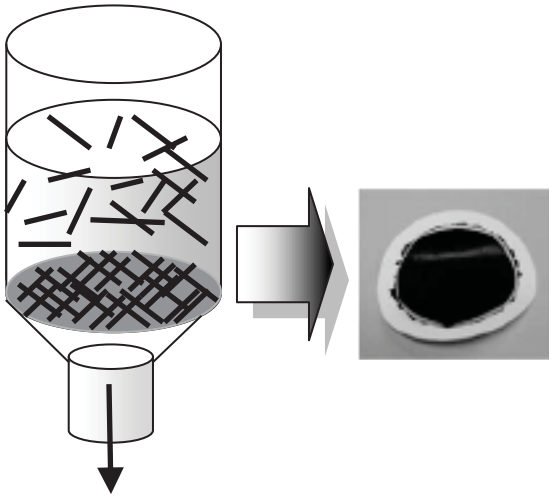

Figure 3.5 Vacuum filtration process for fabrication of paper-like electrode.

3.4.3 Coin cell assembly

The electrochemical cells (CR 2032 coin type cell) contained active materials on Cu or Al foil as the working electrode, Li foil as the counter electrode and reference electrode, a porous polypropylene film as separator, and 1 M LiPF6 in a 50:50 (v/v) mixture of ethylene carbonate (EC) and dimethyl carbonate (DMC) as the electrolyte. The cells were assembled in an Ar-filled glove box (Mbraun, Unilab, Germany) with O_2 and H_2O levels less than 1 ppm. The specific capacity has been

calculated based on the mass of active materials in the electrode. A schematic diagram of the coin-type cell used in ISEM is shown in Fig. 3.6.

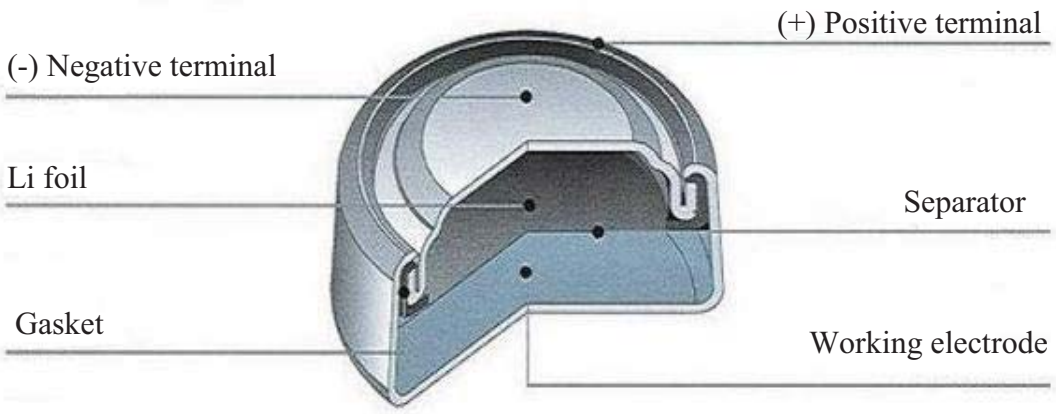

Figure 3.6 Schematic diagram of the coin-test cell (CR 2032) structures.

3.4.4 Flexible cell assembly

Soft aluminium laminated sheets (provided by DLG Battery Co., Ltd, Shanghai, China) were used to fabricate pouch-type cells for testing for flexible and bendable batteries. The pouch-type cells were assembled in an Ar-filled glove box (Mbraun, Unilab, Germany) by stacking a gel electrolyte between film electrodes and a lithium foil counter electrode. The gel electrolyte was prepared by the liquid–liquid extraction process [272] and consisted of poly(vinylidenefluoride-co-hexafluoropropylene) P(VDF-HFP), *N*-methylpyrrolidinone (NMP), and nanoscale Al_2O_3 powders with an average particle size of 30 nm, with all chemicals obtained from Sigma-Aldrich. 1 M $LiPF_6$ solution in ethylene carbonate (EC) – dimethyl

carbonate (DMC) was purchased from Merck Co. and used without any treatment. A certain amount of P(VDF-HFP) was dissolved in NMP at 50 °C. Then, the nanoscale Al_2O_3 particles were added to the viscous solution and agitated with an ultrasonic stirrer. The resulting slurry was cast onto a glass plate or directly onto the surface of the film electrode and dried under vacuum at 80 °C for 8 h. After evaporation of the NMP, the electrode with gel electrolyte precursor was soaked in a 1 mol/L solution of $LiPF_6$/EC–DMC (volume 1:1) for 1 h. The surface of the electrode with gel electrolyte was wiped clean with filter paper, and then the electrode with its gel electrolyte was fabricated into flexible bendable cells with lithium foil as the counter electrode. Fig. 3.7 contains a schematic diagram of a typical flexible and bendable cell for bending-state electrochemical testing.

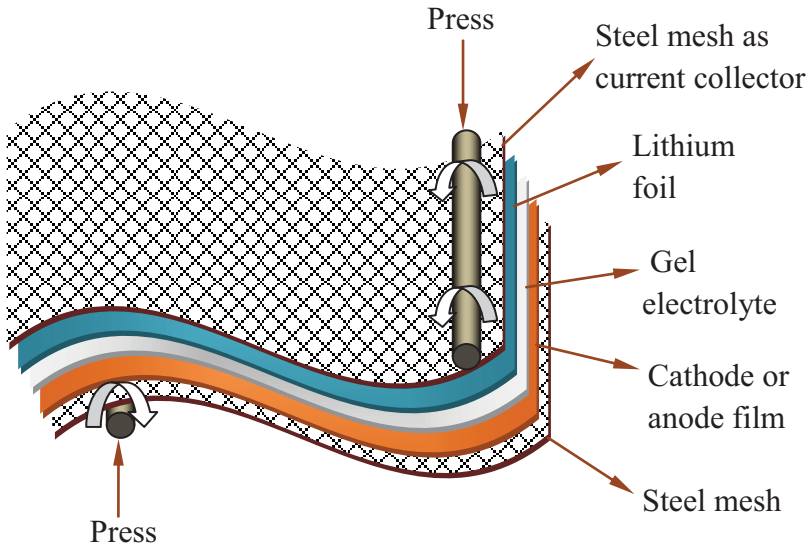

Figure 3.7 Schematic diagram of flexible and bendable test cell's structure.

3.5 Electrochemical characterization

When an electrochemical system is subjected to the passage of current between the two electrodes, it is then out of equilibrium. Usually we are interested in

investigating the electrode process at one electrode, which is the working electrode. The other electrode, the counter electrode, is used to complete the external circuit. Occasionally a third electrode is employed, the reference electrode. When this is the case, the electrode potential is monitored with respect to the reference electrode. Electrochemical measurements, including cyclic voltammetry, charge-discharge testing, and electrochemical impedance spectroscopy, were used to characterize the performance of the electrodes in a lithium-ion battery system.

3.5.1 Cyclic voltammetry (CV)

Cyclic voltammetry (CV) is perhaps the most effective and versatile electroanalytical technique available for lithium-ion batteries, especially for the determination of the thermodynamics and kinetics of electron transfer at the electrode-electrolyte interface. It enables the electrode potential to be rapidly scanned in search of redox couples. It is used most often as a diagnostic tool for elucidating electrode mechanisms. The important parameters are the maximum and minimum points of the potential range, which define the potential window. The choice of this potential window must take into account the stability range of the chosen electrolyte, to thereby avoid its decomposition. The cell is cycled in the potential window, where the potential applied on the working electrode is scanned at a constant rate. The change in potential as a function of time is called the scan rate. By measuring the current change over a whole cycle (cathodic and anodic scan), one can tell that a particular electrochemical reaction takes place and is associated with the observation of a current peak. A positive sweep rate causes the oxidation of the working electrode and the resulting current has a positive sign. With a negative sweep rate,

the reduction of the working electrode causes a negative current. Cyclic voltammetry (CV) measurements were conducted via a CHI 660 electrochemical workstation (CH Instrument, Cordova, TN) at ISEM.

3.5.2 Charge and discharge

The charge-discharge tests were conducted at a constant current density. The capacity (Q) can be calculated based on the charge or discharge time using the formula Q = I x t, where I is the current density and t is the time. The instrument used here to obtain the data was a Land battery tester (China) at ISEM.

3.5.3 Electrochemical impedance spectroscopy (EIS)

AC impedance spectroscopy is a powerful technique to determine the kinetic parameters of the electrode process, including those in the electrolyte, passivation layers, charge transfer, and Li^+ diffusion. Charge-transfer resistance (R_{ct}) is one of the most important parameters for quantitatively characterizing the speed of an electrode reaction. Normally, a large charge-transfer resistance indicates a slow electrochemical reaction. The R_{ct} can be calculated from electrochemical impedance spectroscopy (EIS), with the value being equal to the diameter of the compressed semicircle in the medium-frequency region, as shown in Fig. 3.8. Typically, the impedance curves of a lithium-ion battery show one compressed semicircle in the medium-frequency region, which could be assigned to the charge-transfer resistance (R_{ct}) and an inclined line at approximately 45^o in the low frequency range, which could be considered as Warburg impedance. The AC impedance spectroscopy measurements were carried out at ISEM using a CHI 660 electrochemical

workstation system (CH Instrument, Cordova, TN) by applying a sine wave of 10 mV amplitude over a frequency range of 100.00 kHz to 0.01 Hz. In addition, this technique has been used to determine the ionic conductivity of electrolytes consisting of thin films of polymers. The ionic conductivity (σ) of the sample was calculated from Equation (3.4) below:

$$\sigma = \frac{t}{R_b A} \tag{3.4}$$

where A is the area of film-electrode contact, t is the thickness of the film and R_b is the bulk resistance of the film in Ohms obtained from the complex impedance measurements.

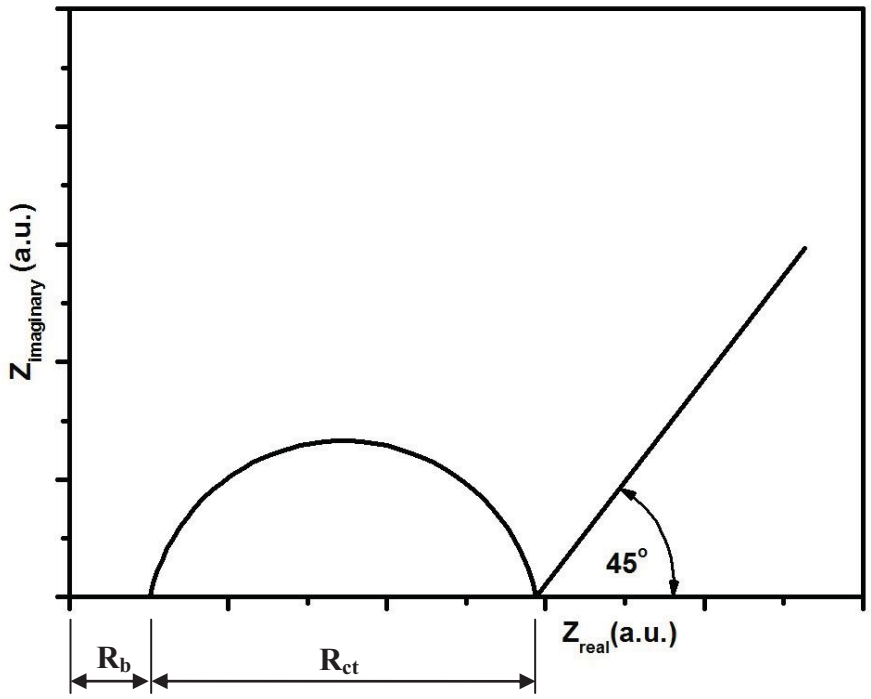

Figure 3.8 Typical electrochemical impedance curve of lithium ion battery.

3.6 Chemicals and materials

All the chemicals and materials used during the PhD work for synthesis, characterization, and electrochemical testing are listed in Table 3.1. The details of purity and the suppliers are also provided for reference.

Table 3.1 List of chemicals and materials used in this thesis.

Materials/chemicals	Formula	Purity (%)	Supplier
1-methyl-2-pyrrolidinone (NMP)	C_5H_9NO	99.5	Sigma Aldrich, Australia
Acetone	CH_3-CO-CH_3	99.9	Ajax, Australia
Acetylene carbon black	C	N/A	Cabot Australasia Pty. Ltd.
Aluminum laminated pouch cell	N/A	N/A	DLG, China
Aluminum(III) oxide	Al_2O_3	99	Sigma Aldrich, Australia
Citric acid	$C_6H_8O_7$	99.5	Sigma Aldrich, Australia
Copper foil	Cu	N/A	DLG, China

Materials/chemicals	Formula	Purity (%)	Supplier
CR 2032 type coin cells	N/A	N/A	DLG, China
Diethyl carbonate	$C_5H_{10}O_3$	> 99	Sigma Aldrich, Australia
Diethylene glycol	$(HOCH_2CH_2)_2O$	99	Sigma Aldrich, Australia
Ethanol	C_2H_5OH	reagent	Ajax, Australia
Ethylene carbonate	$C_3H_4O_3$	99	Sigma Aldrich, Australia
Graphite	C		Fluka, Australia
Hydrazine	$H_4N_2 \cdot H_2O$	99	Sigma Aldrich, Australia
Hydrogen peroxide	H_2O_2	35	Sigma Aldrich, Australia
Lithium hexafluorophosphate	$LiPF_6$	> 99.99 (battery	Sigma Aldrich,

Materials/chemicals	Formula	Purity (%)	Supplier
		grade)	Australia
Lithium hydroxide monohydrate	$LiOH.H_2O$	98	Sigma Aldrich, Australia
Lithium metal	Li	99.9	Sigma Aldrich, Australia
Milli-Q water	H_2O	5 ppb (TOC)	Millipore, USA
Molybdenum(III) oxide	MoO_3	98	Sigma Aldrich, Australia
Multiwall carbon nanotube	C	> 90	Sigma Aldrich, Australia
Poly(vinylidenefluoride-co-hexafluoropropylene)	$(-CH_2CF_2-)_x$ $[-CF_2CF(CF_3)-]_y$	N/A	Sigma Aldrich, Australia
Polypropylene separator	$(C_3H_6)n$	Celgard 2500	Hoechst Celanese Corporation, USA

Materials/chemicals	Formula	Purity (%)	Supplier
Polyvinylidene fluoride (PVDF)	$(CH_2CF_2)n$	N/A	Sigma Aldrich, Australia
Potassium permanganate	$KMnO_4$	99	Sigma Aldrich, Australia
Pyrrole	C_4H_5N	99	Sigma Aldrich, Australia
Single wall carbon nanotube	C	> 90	CNI, USA
Sodium carboxymethyl cellulose	$C_{28}H_{30}Na_8O_{27}$	N/A	Sigma Aldrich, Australia
Sodium hydroxide	NaOH	99	Sigma Aldrich, Australia
Tetrabutylammonium hexafluorophosphate	$(CH_3CH_2CH_2CH_2)_4N(PF_6)$	99	Sigma Aldrich, Australia
Tin(II) chloride dihydrate	$SnCl_2 \cdot 2H_2O$	98	Sigma Aldrich,

Materials/chemicals	Formula	Purity (%)	Supplier
			Australia
Tin(IV) chloride pentahydrate	$SnCl_4 \cdot 5H_2O$	98	Sigma Aldrich, Australia
Vanadium pentoxide	V_2O_5	99.5	Riedel-de Haën, Germany

Chapter 4

SnO_2-Coated Multiwall Carbon Nanotube Composite Anode Materials for Rechargeable Lithium-Ion Batteries

4.1 Introduction

Recently, there has been great demand for a new generation of electrode materials for lithium ion batteries with higher energy density and better rate capability for applications such as portable electronic devices and electric vehicles [250, 273]. Graphite is currently the commercial anode material, but it has a low theoretical capacity of around 372 mAh g^{-1} [274]. Tin dioxide has been proposed as a promising alternative anode material due to its high theoretical capacity (781 $mAhg^{-1}$) [275-276] and the environmental friendliness of its raw material processing [277]. Nevertheless, the higher magnitude of volume expansion and the agglomeration of tin dioxide particles during the alloying and de-alloying cycles with Li^+ ions are the greatest problems in the cycling process [278]. In order to overcome the volume changes and agglomeration, two main methods have been applied. The first method is to fabricate SnO_2 into specific nanostructures, such as hollow spheres [279-280], nanotubes [281-284], nanowires [285-287], nanorods [288-289], and mesoporous structures [290]. The second is to prepare nanostructured carbon composites by loading nanometer-sized SnO_2 particles onto a carbon-based matrix [291-292]. It is well known that carbon nanotubes can provide a desirable electronic matrix for

anode materials due to their high theoretical electrical conductivity, high aspect ratio, remarkable thermal conductivity, and good mechanical properties [293-294].

To date, composites of tin dioxide coated onto surfaces of carbon nanotubes have been prepared by the chemical solution route [295], the diffusion method [296], chemical vapour deposition [297], the supercritical fluid method [298], and the hydrothermal/solvothermal method [299]. For example, Xu, Sun, and Gao coated MWCNTs with SnO_2 by a one-step chemical solution method in which a lengthy acid-treatment for MWCNTs was needed [300]. Du et al. synthesized SnO_2 nanotubes on carbon nanotubes by a layer-by-layer technique followed by heat-treatment [301]. Zhu et al. reported multiwalled carbon nanotube/SnO_2 core-shell structures produced by a double coating process in a wet chemical route [302]. All those techniques, however, are time-consuming, expensive, and only show relatively low capacity retention. Therefore, it is still necessary to explore simple synthesis techniques for the formation and preparation of SnO_2-coated carbon nanocomposite materials.

In this Chapter, SnO_2 was coated on multiwall carbon nanotubes (MWCNTs) by a simple hydrothermal method involving the use of hydrogen peroxide, but without any subsequent heat–treatment of precipitates at high temperatures. In addition, carboxymethyl cellulose (CMC), which was used as a binder, is water soluble and an inexpensive material compared to the conventional binder, polyvinylidene difluoride (PVDF).Therefore, the usage of CMC makes the whole fabrication of the electrode low in cost and environmentally friendly.

4.2 Experimental

4.2.1 Preparation of SnO2-coated CNT nanocomposites

SnO_2/MWCNT nanocomposites were synthesized by dissolving 0.05 M $SnCl_4 \cdot 5H_2O$ (98%, Sigma-Aldrich) in 30 ml de-ionized water with 5 ml 35% hydrogen peroxide and then adding acid-treated MWCNTs (Sigma-Aldrich, carbon > 90%, trace metal basis). Two composites were prepared with weight ratios of $SnCl_4 \cdot 5H_2O$ to MWCNTs of 50 : 50 and 70 : 30, respectively. Each solution was further dispersed by ultrasonication for 1 hour and then transferred into a Teflon lined autoclave and kept at 150°C for 24 hours. Bare SnO_2 nanopowders were prepared by the same method in the absence of MWCNTs and hydrogen peroxide. The resulting products were washed with deionized water several times and collected by centrifugation. The samples were dried at 60°C overnight in a vacuum oven. A schematic diagram of this process is presented in Fig. 4.1.

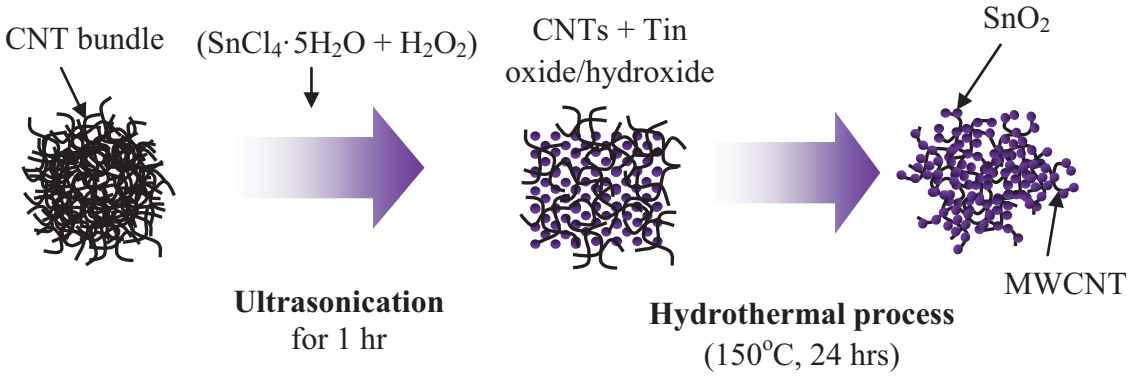

Figure 4.1 Schematic diagram of the synthesis process for SnO_2/MWCNT nanocomposites.

4.2.2 Sample characterization

Phase analysis was carried out by powder X-ray diffraction (XRD) using a GBC MMA X-ray generator and diffractometer with Cu Kα radiation. The

morphologies of the SnO_2/MWCNT nanocomposite powders were investigated by field emission scanning electron microscopy (FE-SEM, JEOL 7500) and transmission electron microscopy (TEM, JEOL EM 2010), as well as by thermogravimetric analysis (TGA) (Mettler Toledo TGA/DSC 1) for determination of the MWCNT content.

4.2.3 Electrochemical measurements

To test the electrochemical performance, MWCNTs, bare SnO_2, and the nanocomposite samples designated 50SnO_2/50CNT and 70SnO_2/30CNT from the corresponding weight ratios were respectively mixed with acetylene black (AB) and a binder, carboxymethyl cellulose (CMC, average Mw: ~250,000, Aldrich) in a weight ratio of 70:20:10 in a solvent consisting of de-ionized water. The slurry was uniformly pasted onto pieces of Cu foil with an area of 1 cm^2. These prepared electrode sheets were dried at 100 °C in a vacuum oven overnight and pressed under a pressure of approximately 3000 kg cm^{-2} for 10 s. Electrochemical measurements, including charge-discharge in the voltage range of 0.05 - 2 V at constant current density of 100 mA g^{-1} and cyclic voltammetry (CV) at a scan rate of 0.1 mV s^{-1}, were performed using a Neware battery tester and a CHI 660b electrochemistry workstation, respectively. The electrochemical cells (CR 2032 coin-type cells), which contained the active materials on Cu foil as the working electrode, Li foil as the counter and reference electrode, and a porous polypropylene film as the separator, were assembled in an argon gas-filled glove box (Mbraun, Germany). The electrolyte was 1 M $LiPF_6$ in a 1:2 (v/v) mixture of ethylene carbonate (EC) and diethyl carbonate (DEC).

4.3 Results and discussion

The diffraction peaks of the XRD patterns for the bare SnO_2 nanopowders could be indexed as tin dioxide, with all peaks corresponding well to standard crystallographic data (JCPDS No. 41-1445), which belongs to space group (SG) $P4_2/mnm$, as shown in Fig. 4.2(a). The crystal structure is tetragonal with lattice parameters a = 4.72 (Å) and c = 3.17 (Å). The X-ray diffraction peaks for both SnO_2/MWCNT nanocomposite powders at 26.7°, 33.9°, 38.0°, and 39° correspond to peaks of SnO_2 nanopowders, while the peaks at 26° are for the MWCNTs. All peaks of the bare SnO_2 and SnO_2/MWCNT nanocomposite samples are broad, indicating their nanocrystalline nature. It was found that the average crystal size of the SnO_2 powders was 15 nm by using the Debye-Scherrer formula for the (1 1 0) peak.

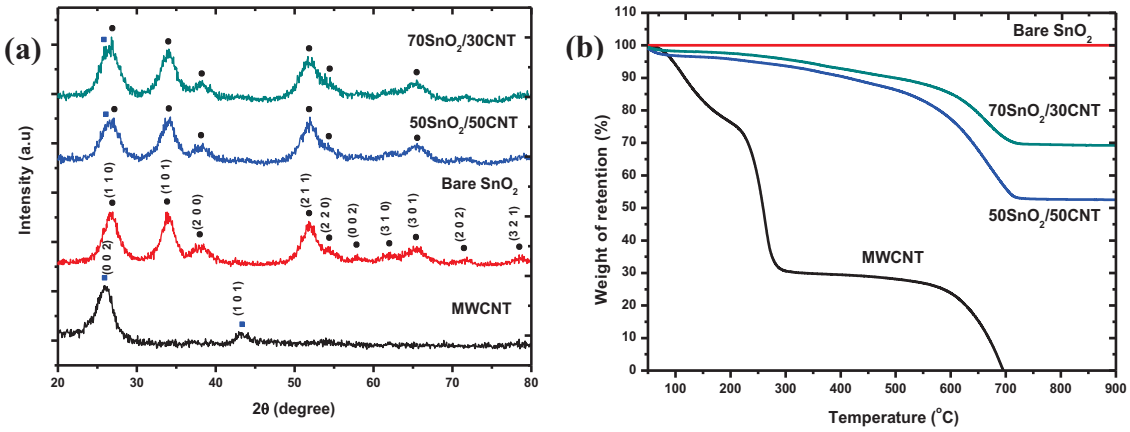

Figure 4.2 XRD patterns (a) and TGA curves (b) of the MWCNTs, bare SnO_2, and $50SnO_2$/50CNT and $70SnO_2$/30CNT nanocomposite powders.

The weight percentage of MWCNTs was obtained by means of thermogravimetric analysis (TGA), as shown in Fig. 4.2(b). The TGA was carried out from 30 to 900 °C, with a heating rate of 10 °C min^{-1} in an air environment. Due to the thermal stability of SnO_2, the bare SnO_2 remains stable during the heating

process. The main weight loss, which resulted from the decomposition of MWCNT-based materials, was obtained from 80 to 700 ^{o}C. The MWCNT contents of 50SnO_2/50CNT and 70SnO_2/30CNT can be estimated to be approximately 47 % and 31 %.

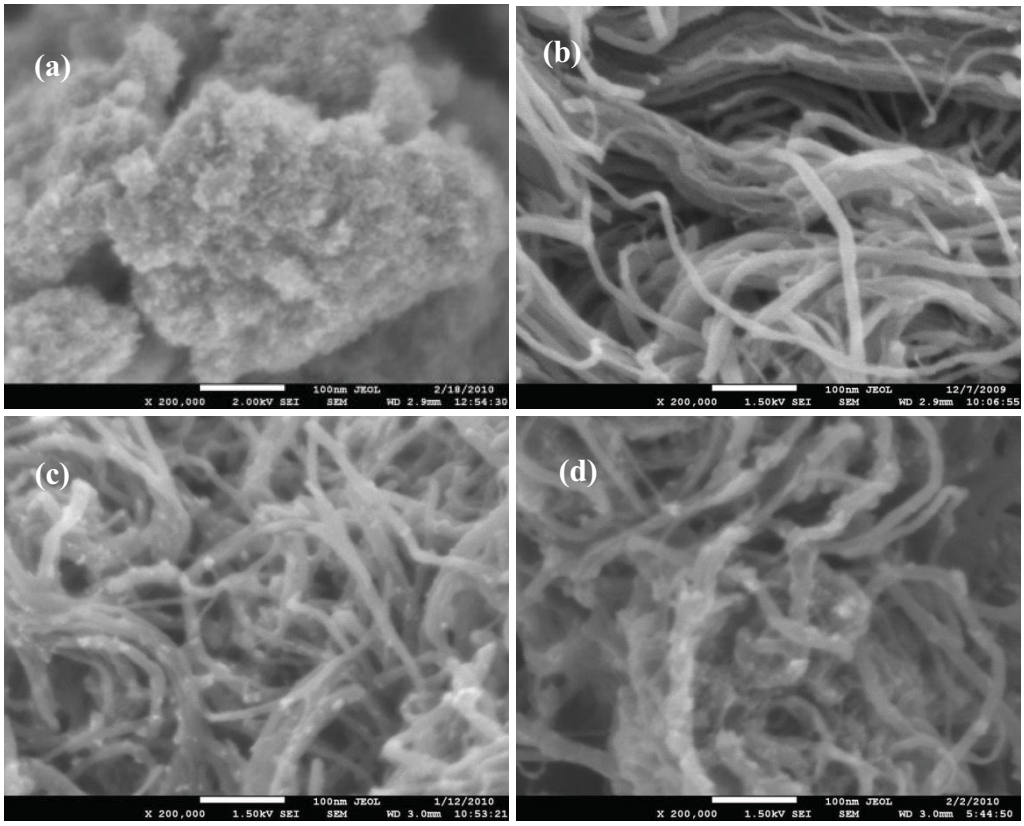

Figure 4.3 FE-SEM images of (a) bare SnO_2, (b) MWCNTs, and nanocomposite powders: (c) 50SnO_2/50CNT, and (d) 70SnO_2/30CNT.

In Fig. 4.3, SEM images provide general information on the SnO_2/MWCNT nanocomposites compared with the MWCNT and bare SnO_2 powders. The bare SnO_2 powders with particle size of about 10 nm are mostly in agglomerated form, as shown in Fig. 4.3(a). Fig 4.3(b) shows the smooth outer surface of the MWCNTs, which have diameters around 10 – 15 nm and are several micrometres in length. The SEM image of 50SnO_2/50CNT presented in Fig. 4.3(c) shows that deposition of

SnO_2 particles onto the surfaces of MWCNTs takes place in some selected sites, while in the $70SnO_2/30CNT$ sample, more SnO_2 particles are deposited on the surfaces of MWCNTs, as shown in Fig. 4.3(d). For further investigation of the morphology and distribution of SnO_2 particles on the surfaces of MWCNTs, Fig. 4.4 shows TEM images of the $70SnO_2/30CNT$ sample. In the lower magnification image in Fig. 4.4(a), the SnO_2 nanoparticles are well dispersed on the CNT bundle. The SnO_2 nanoparticles are highly crystalline, and the particles are between 4 and 5 nm in diameter. It is also observed that SnO_2 nanoparticles are attached onto the surfaces of the MWCNTs, appearing as defects of the MWCNTs. The aligned lattice fringes of the nanoparticles and MWCNTs are clearly visible in the high-resolution TEM (HRTEM) image in Fig 4.4(b), with adjacent fringe spacing of about 0.32 nm corresponding to the (1 1 0) plane of SnO_2 and the carbon layer separation of 0.34 nm assigned to a MWCNT.

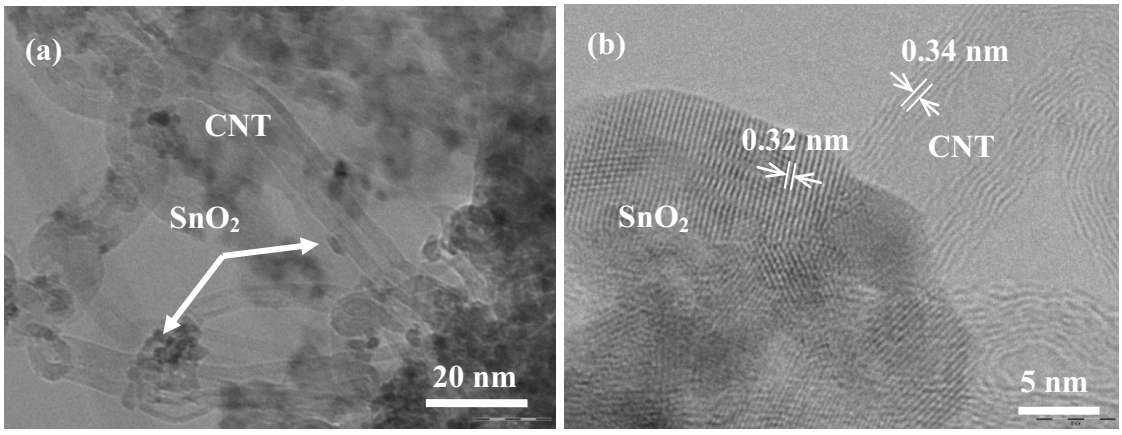

Figure 4.4 TEM images of the$70SnO_2/30CNT$ nanocomposite powders: (a) low resolution image of the composite, (b) high resolution image of the composite lattice spacing.

Fig. 4.5 shows the results of cyclic voltammetry (CV) of the four samples. There is a strong peak at about 0.7 V for the MWCNTs during the first discharge process (Fig. 4.5(a)), due to the formation of the solid electrolyte interphase (SEI) layer [303]. During the first scan of the bare SnO_2 powder electrode shown in Fig. 4.5(b), characteristic peaks at about 0.72 V and 0.10 V appear in the cathodic sweep process. The peak at 0.72 V corresponds to both SEI layer formation and the decomposition of SnO_2 to Sn as in Equation (1) [304]:

$$SnO_2 + 4Li^+ + 4e^- \rightarrow 2Li_2O + Sn \qquad (4.1)$$

and the peak at 0.10 V corresponds to alloying of Sn with Li, as described in Equation (2) :

$$Sn + xLi^+ + xe^- \rightarrow Li_xSn \ (0 \leq x \leq 4.4) \qquad (4.2)$$

while two peaks at about 0.56 V and 1.26 V appear in the anodic sweep process. The peak at 0.56 V represents the de-alloying process of Li^+ ions as described in Equation (3):

$$Li_xSn \rightarrow Sn + xLi^+ + xe^- \ (0 \leq x \leq 4.4) \qquad (4.3)$$

and the following peak at 1.26 V may be from the transfer of electrons during the de-alloying process [291].

There is an increase in the anodic peak at 0.56 V in the second and subsequent cycles, indicating an activation process in the material, as shown in Fig 4.5(b). The cathodic peaks at 0.42 V that appear in the second cycle are due to the formation of β phase tin during the reaction process [299].

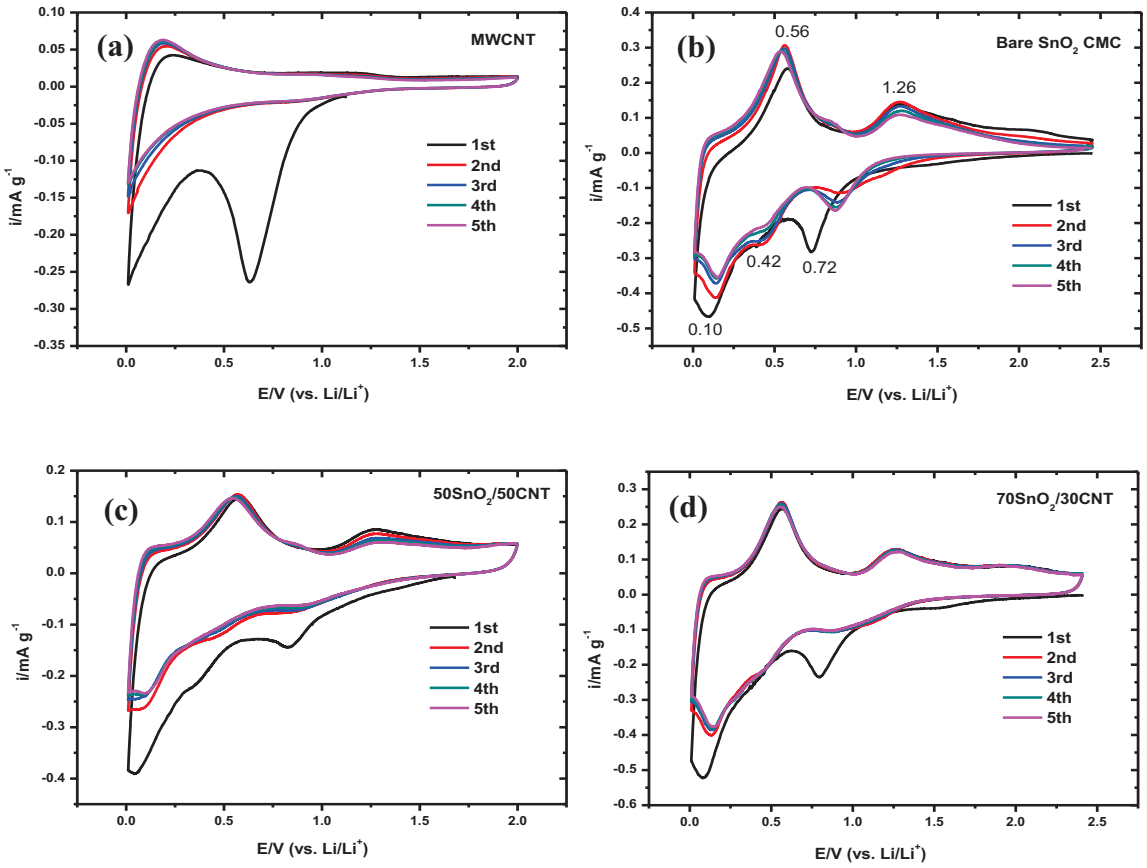

Figure 4.5 Cyclic voltammograms for the first 5 cycles of the MWCNT (a), bare SnO_2 (b), $50SnO_2/50CNT$ (c), and $70SnO_2/30CNT$ (d) electrodes, all at a scan rate of 0.1 mV s^{-1}.

For both the $50SnO_2/50CNT$ and the $70SnO_2/30CNT$electrodes in Fig. 4.5(c) and (d), there are still characteristic peaks at 0.83 V and 0.79 V, corresponding to SEI layer formation and the alloying process, which also respectively correspond to the reaction of lithium with the SnO_2 and the MWCNTs in the first discharge process. The 0.79 V peak intensity of the $70SnO_2/30CNT$ sample, however, is higher than that of the 0.83 V peak of the $50SnO_2/50CNT$ sample because of the large amount of deposited SnO_2. Both samples show well repeated curves in the following cycles, revealing the good cycling stability. In addition, the anodic peaks at 0.56 V of both

samples are different from that of the bare SnO_2 sample. The intensity of the 0.56 V peaks for both composites decreases with cycling, indicating that there is no activation process. This is probably because the SnO_2 nanoparticles are dispersed well on the MWCNT matrix and all the active materials are involved in the reaction from the first cycle [299].

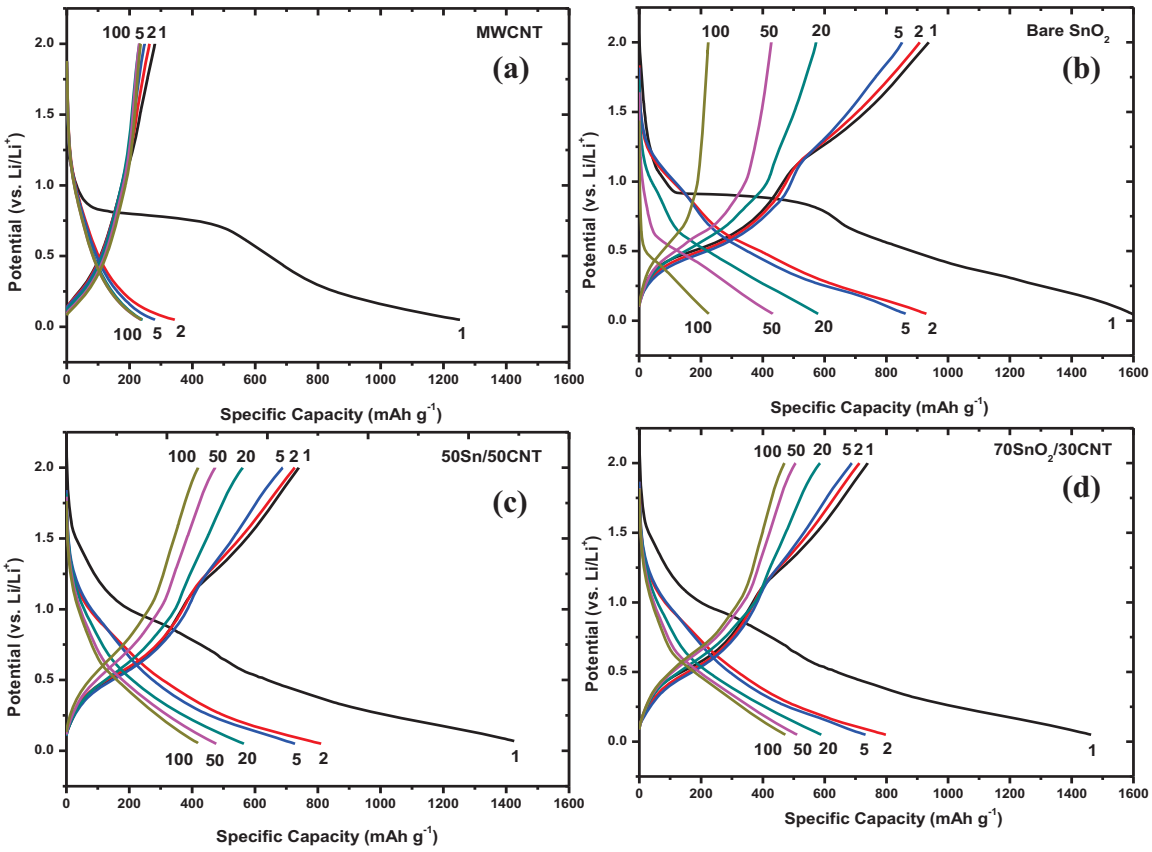

Figure 4.6 Typical discharge-charge curves for selected cycles of the MWCNT (a), bare SnO_2 (b), $50SnO_2/50CNT$ (c), and $70SnO_2/30CNT$ (d) electrodes at constant current density of 100 mA g^{-1}.

Typical charge-discharge curves of the cells with MWCNTs and SnO_2/MWCNT composites at current density of 100 mA g^{-1} are shown in Fig. 4.6. A single plateau for initial discharge was observed for the MWCNT sample around 0.7 V, which is related to the formation of the solid electrolyte interphase (SEI) layer on the surfaces of MWCNTs, as presented in Fig. 4.6(a). The plateau disappears in the following cycles and leaves a large initial irreversible capacity (1252 mAh g^{-1}). The first discharge capacities for the bare SnO_2, 50SnO_2/50CNT, and 70SnO_2/30CNT electrodes are 1601, 1421, and 1463 mAh g^{-1}, respectively, within the potential range from 0.01 V to 2.0 V. The bare SnO_2 (Fig. 4.6(b)) and SnO_2/MWCNT samples show higher capacities in their first discharge than the theoretical specific capacity of SnO_2 (782 mA g^{-1}). The large initial irreversibility of the first discharge capacities is due to the following two reasons: the irreversible trapping of two Li^+ ions per oxygen atom in the formation of Li_2O and the formation of an SEI film on the surfaces of MWCNTs and nascent Sn [305-306]. In addition to the large first discharge capacity of bare SnO_2, the second cycle reversible capacity of bare SnO_2 of 900 mAh/g is larger than the theoretical discharge capacity of SnO_2. This phenomenon was also reported for SnO_2 hollow spheres that exhibited higher reversible capacity than their theoretical value in the first few cycles [88, 307]. It is also found that the nanosized SnO_2 is more favourable for stable cycling properties [307]. Here in this thesis, for bare SnO_2, the smaller nanosize dimensions of the SnO_2 (5 nm) provide more reaction sites for alloying and de-alloying processes with lithium ions. In addition, such an over-capacity contribution can also be found in other reports [308-309], and it is ascribed to the formation of a gel-like organic layer on the surface of the hollow nanostructures.

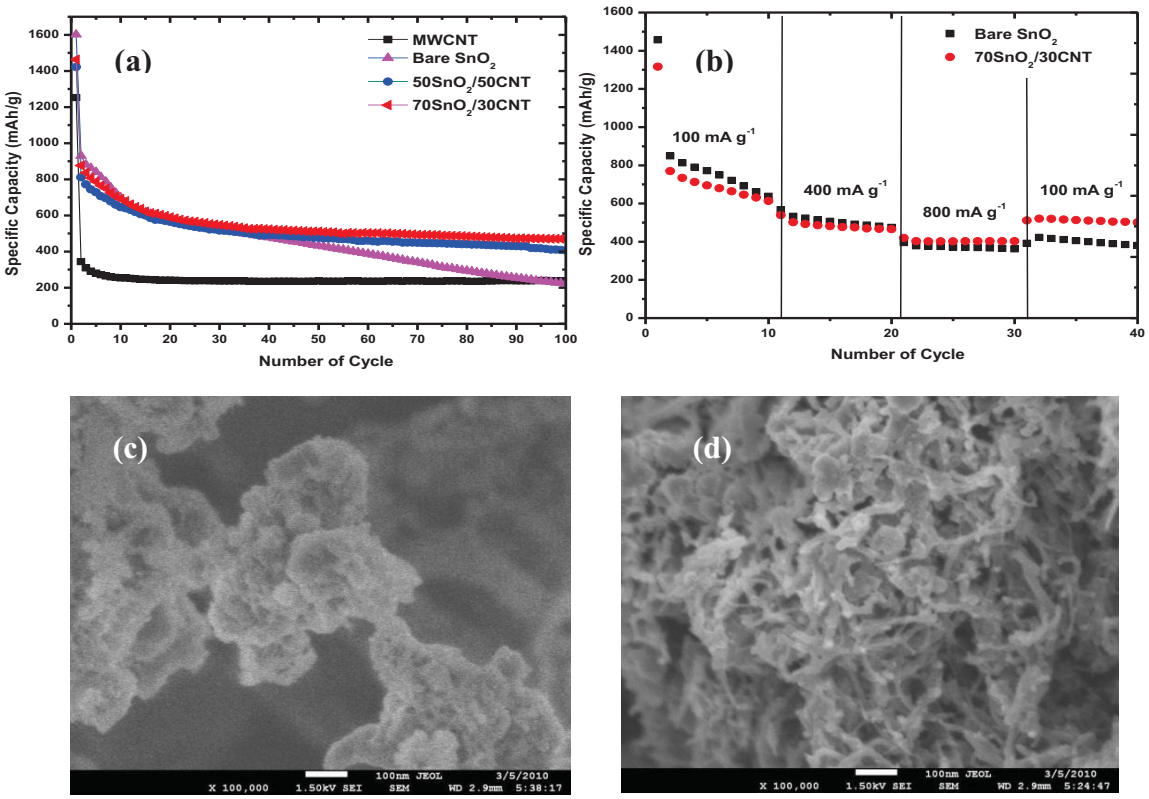

Figure 4.7 The cycling stability of MWCNTs, bare SnO_2, and $50SnO_2$/50CNT and $70SnO_2$/30CNT nanocomposites at constant current density of 100 mA g^{-1} (a); rate capability of bare SnO_2 and $70SnO_2$/30CNT (b); and FE-SEM images of bare SnO_2 (c) and $70SnO_2$/30CNT (d) electrodes after 100 cycles.

Fig. 4.7(a) displays the cycling stability of the bare SnO_2, $50SnO_2$/50CNT, $70SnO_2$/30CNT, and MWCNT electrodes at current density of 100 mA g^{-1} between 0.01 and 2 V. The capacity retention for the first 10 cycles is maintained at 75 %, 79 %, 78 %, and 73 % of reversible discharge capacity (second discharge capacity) for the bare SnO_2, $50SnO_2$/50CNT, $70SnO_2$/30CNT, and MWCNT electrodes, respectively. Beyond 100 cycles, the discharge capacities are still 222 mAh g^{-1}, 406 mAh g^{-1}, 473 mAh g^{-1}, and 238 mAh g^{-1} for the bare SnO_2,

$50SnO_2/50CNT$,$70SnO_2/30CNT$, and MWCNT electrodes, respectively. In terms of the ratio of the specific capacity retained after 100 cycles to the second discharge capacity, the capacity retention for the bare SnO_2, $50SnO_2/50CNT$, $70SnO_2/30CNT$, and MWCNT samples is 23 %, 53 %, 50 %, and 69 %, respectively. These results show that the cycling stability of the MWCNT electrode is the best of all the samples, but it is accompanied by very low discharge specific capacity. For both composites, the capacity retention of the $50SnO_2/50CNT$ electrode is better than that of $70SnO_2/30CNT$, but the specific capacity is lower due to the low content of SnO_2. This phenomenon demonstrates that MWCNTs can prevent the agglomeration of tin particles and improve the cycling stability for both composites, especially for the $50SnO_2/50CNT$ sample. In the case of the $70SnO_2/30CNT$ sample, however, the high content and the good distribution of the SnO_2 particles on the surfaces of the MWCNTs enhance both the electrochemical performance and the structural stability during cycling of the composite, as shown in the FE-SEM images of Fig. 4.7(c) and (d). These images show that the tin particles of the bare SnO_2 sample are mainly in the form of large agglomerations after 100 cycles, in contrast to the dispersed Tin particles in the $70SnO_2/30CNT$ sample. In order to compare the electrochemical performance with the literature, a summary of the specific capacities for different SnO_2/MWCNT composite samples is given in Table 4.1. It can be seen that the $70SnO_2/30CNT$ sample in the present work shows better performance than those of H-SnO_2/CNT (402 mAh g^{-1} after 100 cycles) with 54 % SnO_2 [299], MWCNTs filled with and coated by SnO_2 nanoparticles (S2; 372 mAh g^{-1} after 40 cycles) with 34.9 % SnO_2 [300], and SnO_2 nanotubes on carbon nanotube template (435 mAh g^{-1} after 40 cycles) with 49.76 % SnO_2 [301].

Rate capability test results are shown in Fig. 4.7(b), where the bare SnO_2 sample shows a higher specific capacity in the initial cycle than the $70SnO_2/30CNT$ sample, but after the cycle testing reaches a current density of 800 mA g^{-1}, the $70SnO_2/30CNT$ sample shows larger capacity compared to the bare SnO_2.

Table 4.1 Comparison with references in the literature of the specific capacities for different SnO_2/CNT composites.

Material	**Capacity (mAh g^{-1})**	**Cycle number**	**Current density (mA g^{-1})**	**Reference**
$70SnO_2/30CNT$	473	100	100	Present work
H-SnO_2/CNT	402	100	100	[28]
MWCNTs filled with and coated by SnO_2 nanoparticles	372	40	70	[300]
SnO_2 nanotubes on carbon nanotube template	435	40	200	[301]

This is because the MWCNTs contribute to maintaining the electronic conduction, as well as preventing tin particles from aggregating and accommodating the volume variation [310]. When the current density changes back to 100 mA g^{-1}, the

$70SnO_2/30CNT$ sample delivers a specific capacity above 500 mAh g^{-1}, which is much higher than that of the bare SnO_2 powder electrode.

In order to verify the effect of MWCNTs on the electronic conductivity of the nanocomposite, electrochemical impedance spectroscopy (EIS) measurements were carried out on the bare SnO_2 and $70SnO_2/30CNT$ samples using a sine wave of 5 mV amplitude over a frequency range of 100 kHz – 0.01 Hz. To achieve stable SEI formation and the percolation of electrolyte through the electrode materials, the impedance measurement was performed after running 5 charge-discharge cycles. Impedance was also measured after 100 cycles for the samples. Fig. 4.8 shows the Nyquist plots obtained from the bare SnO_2 and the $70SnO_2/30CNT$ samples after the 5^{th} and 100^{th} cycle tests. The intercept at the Z_{real} axis at high frequency corresponds to the ohmic resistance (R_Ω), which represents the total resistance of the electrolyte, separator, and electrical contacts. The depressed semicircle in the middle frequency range relates to the charge transfer resistance (R_{ct}). CPE is the constant phase-angle element, involving double layer capacitance. The inclined line at lower frequency represents the Warburg impedance (W), which is associated with Li-ion diffusion in the SnO_2 particles. An equivalent circuit model was constructed to analyze the impedance spectra, as shown in the inset to Fig. 4.8(a). Table 4.2 shows parameters of the equivalent circuit for the bare SnO_2 and the $70SnO_2/30CNT$ samples after fitting the diameter of the semicircular curve. It is found that the size of the depressed semicircle in the middle frequency range for the $70SnO_2/30CNT$ sample after 5 cycles and 100 cycles is smaller compared to the bare SnO_2 sample, revealing the lower charge transfer resistance of the $70SnO_2/30CNT$ sample. This indicates

that the electronic conductivity of the 70SnO_2/30CNT sample was improved due to the good electrical conductivity of the MWCNTs in the composite material, where they served as both an active material and a conductor in the anode composite.

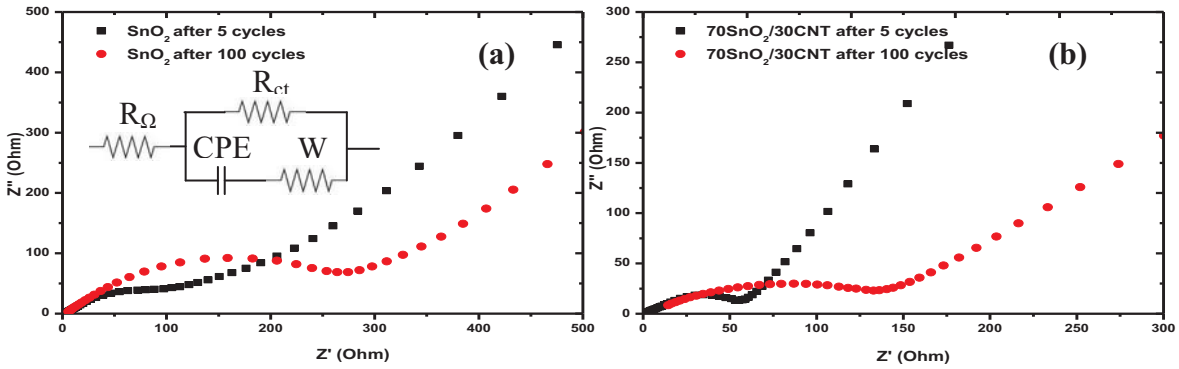

Figure 4.8 Nyquist plots of the cells containing (a) the bare SnO_2 and (b) the 70SnO_2/30CNT nanocomposite electrodes after 5 and 100 charge-discharge cycles. The inset in (a) shows the equivalent circuit model.

Table 4.2 Impedance parameters calculated from equivalent circuit model.

Electrode Materials	**Cycles**	**R_Ω (Ω)**	**R_{ct} (Ω)**
SnO_2	5	4.62	123.72
	100	5.89	321.86
70SnO_2/30CNT	5	2.77	61.12
	100	11.68	131.38

4.4 Conclusions

SnO_2/MWCNT nanocomposites have been synthesized by a simple hydrothermal method without any subsequent calcining process. The SEM image of $50SnO_2/50CNT$ shows that deposition of the SnO_2 particles onto the surfaces of the MWCNTs takes place in some selected sites, while in the $70SnO_2/30CNT$ sample, more SnO_2 particles are deposited on the surfaces of MWCNTs. The $70SnO_2/30CNT$ composite sample shows very stable cycling stability up to 100 cycles, with discharge capacity as much as 473 mAh g^{-1} compared to the $50SnO_2/50CNT$ sample (406 mAh g^{-1}), because the SnO_2 nanoparticles in the $70SnO_2/30CNT$ composite sample are well dispersed in the MWCNT matrix, protecting them from agglomeration. The capacity retention of the $50SnO_2/50CNT$ electrode is better than that of $70SnO_2/30CNT$, but the specific capacity is lower due to the low content of SnO_2. The EIS results show that the electronic conductivity of the $70SnO_2/30CNT$ sample was improved due to the good electrical conductivity of the MWCNTs in the composite material, where they served as both an active material and a conductor in the anode composite.

Chapter 5

Free-Standing Single-Walled Carbon Nanotube/SnO_2 Anode Paper for Flexible Lithium-Ion Batteries

5.1 Introduction

There has been more interest recently in flexible and bendable energy storage devices, especially in the field of lithium ion batteries [311-313]. Recent advanced technology in various types of soft portable electronic equipment, such as roll-up displays, wearable devices, and implanted medical devices, requires development of flexible batteries as their power sources. Active radio-frequency identification tags and integrated circuit smart cards also require bendable or flexible batteries for operation in daily use [6, 314]. Typically, lithium batteries consist of a positive electrode and a negative electrode spaced by a separator, which is soaked in an electrolyte solution [73]. Each electrode is formed from a metal substrate that is coated with a mixture of an active material, an electrical conductor, a binder, and a solvent. This type of electrode is not suitable for flexible or bendable batteries, because a metal substrate is used to support the active materials. The active material layer will be damaged or peeled off from the substrate if it is bent. Therefore, the development of free-standing flexible electrode materials is important for flexible and bendable energy storage devices. Recent reports show that paper-like material could be adopted as a key element for application in a flexible lithium rechargeable battery, by embedding it with aligned carbon nanotube (CNT) electrode or integrating it with CNT film into a single sheet of paper through a lamination process

[252, 315]. Flexible electrode based on free-standing graphene paper also has been reported by Gwon et al. [255].

Single wall carbon nanotubes (SWCNT) are a promising option for lithium ion batteries due to their one-dimensional structure with high length-to-diameter ratio, combined with high porosity and high surface area [19-20]. In addition, the outstanding physical properties of SWCNTs, such as high theoretical tensile strength, high electrical conductivity, and high flexibility, make SWCNTs potentially useful for producing flexible and bendable free-standing electrodes [316-317]. Although SWCNTs have several advantages, their practical capacity as free-standing electrode materials is still low, less than 200 mAh g^{-1} after 100 cycles [35, 318]. SWCNTs are formed when a graphene sheet is folded to form a cylinder. These cylinders usually aggregate into bundles, which consist of SWCNTs held together by van der Waals forces [319]. These bundles are expected to display a higher capability for intercalating lithium atoms and consequently higher energy storage capacity. In the ideal case, this gives enhanced anode stoichiometry in the form of LiC_2 [320]. The superior battery performance of SWCNTs depends on the ability of lithium ions to enter and leave the nanotube interior at a reasonable rate. This rate can be improved if the lithium ions reach the interior through topological defects on the side walls and open ends. As a matter of fact, in the experiments carried out by Gao et al. [321], the intercalation density was improved up to $Li_{2.6}C_6$ after ball milling, suggesting that the ball-milling process creates defects and breaks the nanotubes, allowing the lithium ions to intercalate inside the nanotubes. In this Chapter, however, we have tried to improve the practical capacity of SWCNTs by depositing an electrochemically active

second phase with higher capacity on the surface of the SWCNTs by the reflux process to create a hybrid composite.

Tin dioxide is one of the most promising candidates as a second electrochemically active phase to incorporate into carbon-based free-standing electrode for higher specific capacity, due to its own higher specific capacity (781 mAh g^{-1}) [275-276] and the environmental friendliness of its raw material processing [322]. Anodes of such high capacity, however, usually suffer severe capacity fading, stemming from both the quick aggregation of tin particles and the huge volume change (over 300%) during Li^+ insertion/extraction cycles, which causes pulverization of the anode and electrical detachment of active materials [323-324]. Reducing the material's size down to the nanoscale and dispersing the material into a conductive matrix has proved to be very effective for solving these problems in similar systems [325-327]. There have already been some reports of applying inorganic – CNT composites as high-capacity anodes for lithium-ion batteries (LIBs), but all of these composites were prepared using CNTs as collectors for sediments, so carbon black and polymer binders had to be used to lower the resistance and hold the electrodes together [325, 328-329]. In contrast, self-supported SWCNT films have been demonstrated to be very attractive candidates for free-standing (not needing any current collectors) and binder-free anodes in LIBs. These will not only significantly improve the specific mass capacity of practical LIBs, but also lower the manufacturing costs. In addition, the conductive matrix of a free-standing SWCNT film should be able to effectively accommodate huge volume changes, thereby significantly improving the cycling performance of high-capacity electrodes. Zhang's group has reported binder-free, cross-stacked carbon nanotube

sheets with uniformly loaded SnO_2 nanoparticles [330]. Although the composite sheets showed high electrochemical performance with 100 % capacity retention for at least 65 cycles, the synthesis method is quite complicated and time consuming.

In this Chapter, free-standing SWCNT/SnO_2 anode paper was prepared by a two-step fabrication method. The anode paper shows several advantages. First, SWCNTs can act as a flexible and highly conductive matrix, which can not only accommodate the large volume changes that accompany charge/discharge in tin dioxide, but also provides good contact for the SnO_2-based materials. Second, the deposited SnO_2 can improve the total specific capacity of the SWCNT paper. Finally, the binder-free nature of the anode paper also contributes to the low cost and environmental friendliness of the whole electrode fabrication process.

5.2 Experimental

5.2.1 Preparation of SWCNT/ SnO_2 hybrid material

The SWCNT/SnO_2 hybrid material was prepared in the molar ratio of Sn : C = 0.3 : 1. $SnCl_2 \cdot 2H_2O$ (98 %, Sigma-Aldrich) was first dissolved in 50 ml of diethylene glycol (DEG, Fluka), and then mixed with SWCNTs (Carbon Nanotechnologies Incorporated (CNI), USA, carbon > 90 %, trace metal basis) by ultrasonication for 1 hour. Subsequently, the solution was placed in a round-bottomed flask. The solution was heated and kept under reflux conditions at 195 ^{o}C for 4 hours with vigorous stirring in air. During the natural cooling process, the magnetic stirring was continued. The resulting products then were washed with acetone several times and collected by centrifuge at 4400 rpm. Finally, the samples were dried at 80 ^{o}C overnight in a vacuum oven.

5.2.2 Preparation of free-standing SWCNT/ SnO_2 paper

To make a uniform paper, a vacuum filtration technique was adopted [271] with some modifications [35, 318], such as using a 3-piece filter funnel (Whatman). In a typical procedure, 20 mg of SWCNT/SnO_2 hybrid material was dispersed into 1 wt% Triton X-100 surfactant (Sigma-Aldrich) in 50 mL of distilled water. The suspension was then ultrasonically agitated using a probe sonicator for 30 min. The as-prepared suspension was poured into the funnel and filtered through a porous polyvinylidene fluoride (PVDF) membrane (Millipore, 0.22 μm pore size, 47 mm in diameter) by positive pressure from a vacuum pump. Since the solvent could pass through the pores of the membrane, the SWCNT/SnO_2 hybrid was trapped on the membrane surface, forming a dark mat. The resultant mat was then washed twice using distilled water, followed by ethanol to remove any remaining surfactant. The mat was allowed to dry overnight at room temperature. Finally, the mat was peeled off from the PVDF membrane, and SWCNT/SnO_2 paper was obtained. To obtain highly crystalline SnO_2, the paper was heated at 300 ^oC for 30 minutes in air. For comparison, pure free-standing SWCNT paper was also prepared using the same method.

5.2.3 Physical characterization

Phase analysis was carried out by powder X-ray diffraction (XRD) using a GBC MMA X-ray generator and diffractometer with Cu K_α radiation at a scanning rate of $5^o\,min^{-1}$ over the 2θ angle range from 10^o to 80^o. The morphology of the free-standing SWCNT/SnO_2 electrode was investigated by field emission scanning electron microscopy (FE-SEM, JEOL 7500, operated at an acceleration voltage of

1.5 kV), transmission electron microscopy (TEM, JEOL EM 2010), and thermogravimetric analysis (TGA, Mettler Toledo TGA/DSC 1) for determination of the SnO_2 content. TEM samples of the anode paper were prepared by removing a small piece of the paper and mounting it on a folding copper mesh oyster grid.

5.2.4 Electrochemical measurements

Square model electrodes were cut off from the obtained free-standing paper. The electrodes were then dried at 120 ^oC overnight in a vacuum oven. To test the electrochemical performance, charge-discharge in the voltage range of 0.01 - 2 V at constant current density of 25 mA g^{-1} and cyclic voltammetry (CV) at the scan rate of 0.05 mV s^{-1} were conducted using a Land battery tester and a CHI 660b electrochemistry workstation, respectively. Electrochemical impedance spectroscopy (EIS) measurements were carried out on the samples with a PARSTAT 2273, using a sine wave of 10 mV amplitude over a frequency range of 100 kHz – 0.01 Hz. The electrochemical cells (CR 2032 coin-type cells and flexible bendable cells), containing SWCNT/SnO_2 as the working electrode, Li foil as the counter electrode and reference electrode, and a porous polypropylene film as separator, were assembled in an argon gas filled glove box (Mbraun, Germany). The electrolyte was 1 M $LiPF_6$ in a 1 : 2 (v/v) mixture of ethylene carbonate (EC) and diethyl carbonate (DEC).

In the case of flexible cells, the cells were prepared by first making a gel electrolyte containing poly(vinylidenefluoride-co-hexafluorpropylene) (P(VDF-HFP)), which was obtained as received from Sigma-Aldrich. *N*-methylpyrrolidinone (NMP) and nanoscale Al_2O_3 powders with average particle size of 30 nm were

obtained from Sigma-Aldrich. 1 M $LiPF_6$ solution in ethylene carbonate (EC) and diethyl carbonate (DEC) in a 1 : 2 ratio (v/v) was used as purchased from Merck Co. without any treatment. The porous electrolyte film was prepared by the liquid–liquid extraction process [331]. A certain amount of P(VDF-HFP) was dissolved in NMP at 50 °C. Then, nanoscale Al_2O_3 particles were added to the viscous solution and agitated with an ultrasonic stirrer. The resulting slurry was cast on the surface of the SWCNT/SnO_2 anode paper and dried under vacuum at 80 °C for 8 h. After evaporation of the NMP, the electrode was left to cool to room temperature in situ. It was then soaked in the 1 mol/L solution of $LiPF_6$/EC–DEC (volume 1:1) for 1 h to make the porous polymer electrolyte. After the excess solution at the surface of the electrode was absorbed with filler paper, a flexible cell was fabricated from the SWCNT/SnO_2 anode with the gel electrolyte, lithium foil as counter and reference electrode, and a porous polypropylene film as separator, using an aluminium laminated pouch as the casing.

5.3 Results and discussion

Fig. 5.1(a) shows the XRD patterns for the SWCNTs purchased from CNI, Inc., USA and the SWCNT/SnO_2 paper synthesized by the polyol method. The diffraction peaks of the SWCNT/SnO_2 are consistent with the tetragonal cassiterite phase of SnO_2 (JCPDS- No 41-1445), which belongs to space group (SG) $P4_2/mnm$; the individual sets of planes are indexed in the figure. The additional diffraction lines at 2θ of 23^o and 44^o correspond to the characteristic peaks of SWCNTs. The broad peak of the (0 0 2) diffraction of SWCNT indicates the typical random arrangement of carbon nanotubes, with $d_{0\,0\,2}$ of 0.38 nm calculated according to Bragg's equation. The peaks of the SWCNT/SnO_2 samples are broad as well, indicating their

nanocrystalline nature. The approximate crystallite size of SnO_2 phase in the hybrid was estimated to be around 1.7 nm, using the Debye-Scherrer equation applied to the (1 1 0) peak in Traces software, where the Si standard (2 2 0) peak is used as the full-width half-maximum (FWHM) standard.

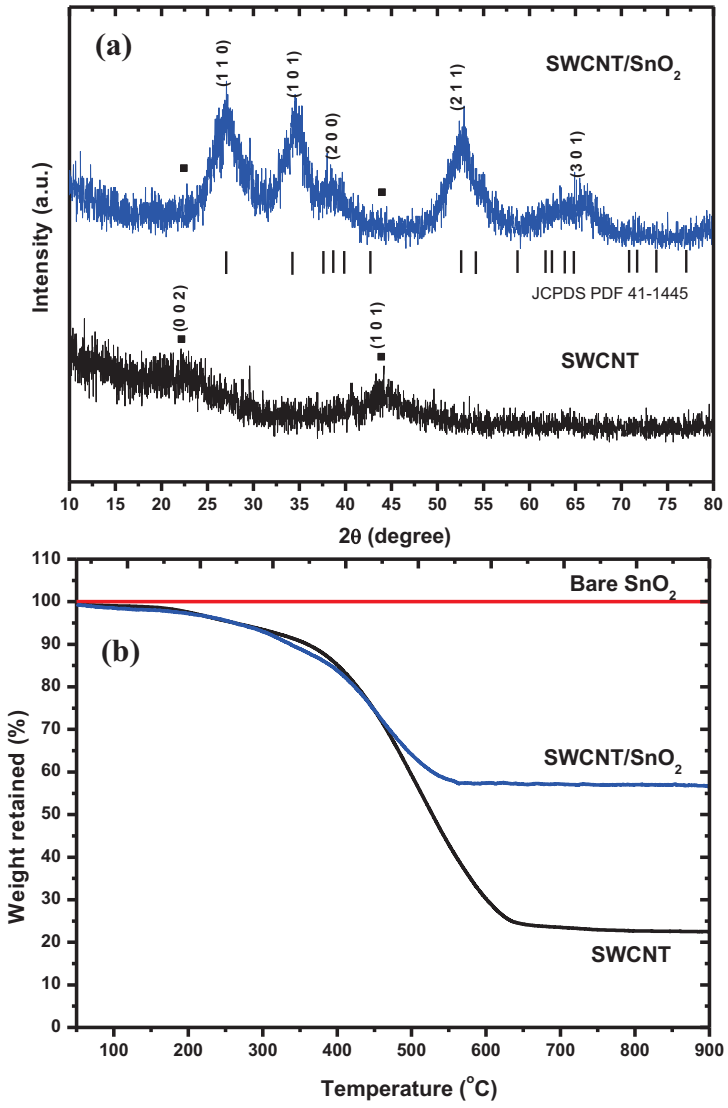

Figure 5.1 (a) XRD patterns and (b) TGA curves of the pristine SWCNTs, bare SnO_2, and SWCNT/SnO_2.

For quantifying the amount of SnO_2 in the hybrid, TGA was carried out in air. The sample was heated from 25 to 900 ^oC at a rate of 10 ^oC min^{-1}. Fig. 5.1(b)

shows the TGA curve for the SWCNT/SnO_2 hybrid along with those of the SnO_2 and SWCNT powders. It can be seen that the bare SnO_2 powder remains thermally stable, while the SWCNT/SnO_2 hybrid starts to decompose slowly in air at temperatures above 100 ^oC, with the SWCNTs finally burning out at about 600 ^oC. Since the bare SnO_2 powder remains stable in this temperature range, any weight change corresponds to the oxidation of SWCNTs. Therefore, the change in weight before and after the oxidation of SWCNTs can be translated into the amount of SnO_2 in the SWCNT/SnO_2 hybrid. With the use of this method, the approximate amount of SnO_2 can be estimated by first subtracting the residual amount of impurities contained in the as-purchased SWCNTs. Therefore, the final amount of SnO_2 is approximately 34 wt%.

SWCNTs are typically synthesized using metal catalysts. In this Chapter, the raw SWCNTs, purchased from Carbon Nanotechnologies Incorporated (CNI), USA, were prepared by the high pressure CO disproportionation (HiPco) method and contain residual Fe catalyst, as confirmed by the energy dispersive spectroscopy (EDS) results (Fig. 5.2(b)). A typical TGA plot of a sample of as-received SWCNTs is shown in Fig. 5.2(a), with the heating rate 10 $^oC\ min^{-1}$ in air. The initial curve shows a gradual initiation of the transition (starting from 50 ^oC) because the nanotubes were contaminated with amorphous carbon and other types of carbonaceous impurities that oxidize at temperatures lower than that of the nanotubes [1]. The curve indicates the start of slow decomposition in air at temperatures above 100 ^oC, with the SWCNTs finally burning out at about 650 ^oC. To determine the mass of iron catalyst impurity in the SWCNTs, the residual mass must be calculated. From this TGA diagram, it can be seen that 78 % of the total mass is lost at 650 °C.

This mass loss is attributed to the removal of carbon. The residual mass is 22 %. The TGA data in Fig. 5.2(a) indicates that the oxidation temperature (T_o) is 502 ^oC. The sample exhibited only one exothermal event. The overall thermal stability is low and consistent with a large amount of iron particles. This result is similar what was reported by Arepalli and co-workers [2].

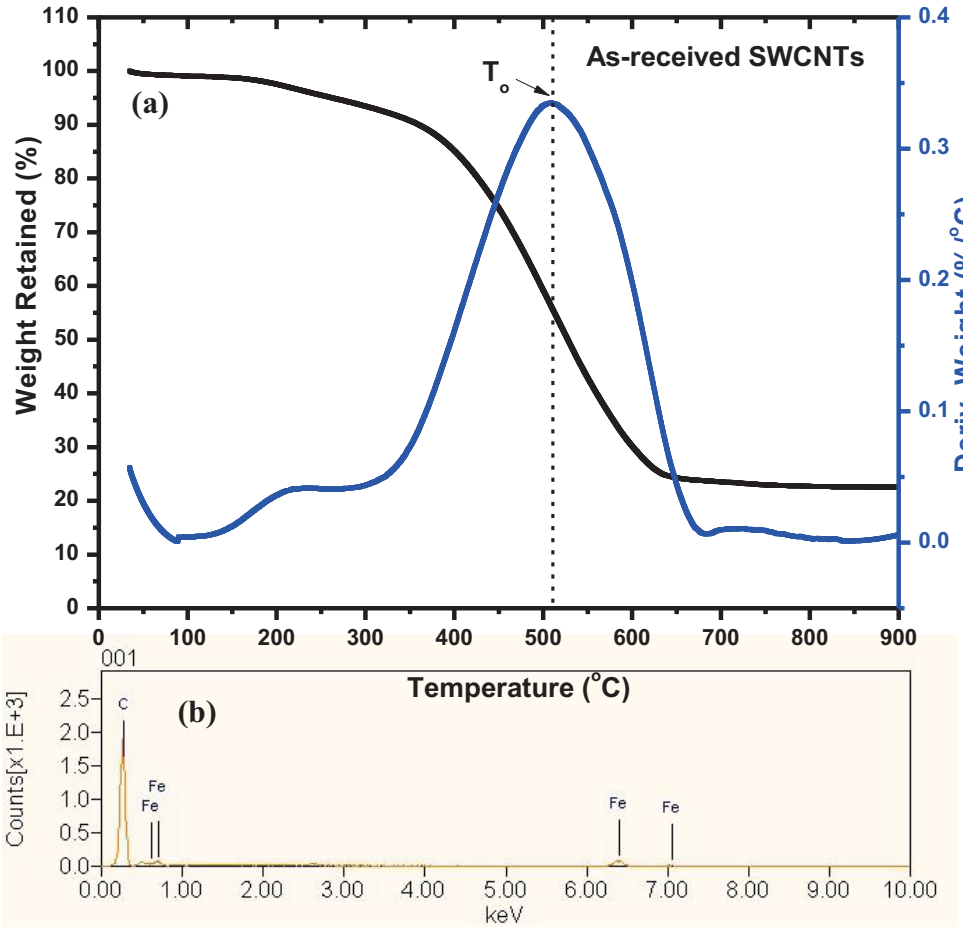

Figure 5.2 TGA curve of as-received SWCNTs with 10 °C min^{-1} heating rate in air (a) and the corresponding EDS spectrum (b).

FE-SEM images showing cross-sectional and top views of the SWCNTs and SWCNT/SnO_2 paper are presented in Fig. 5.3. The top-view FE-SEM image reveals that the SWCNTs and SWCNT/SnO_2 paper appear as webs of curved nanotubes, forming strong intertwined entanglements with a three-dimensional (3D) network structure.

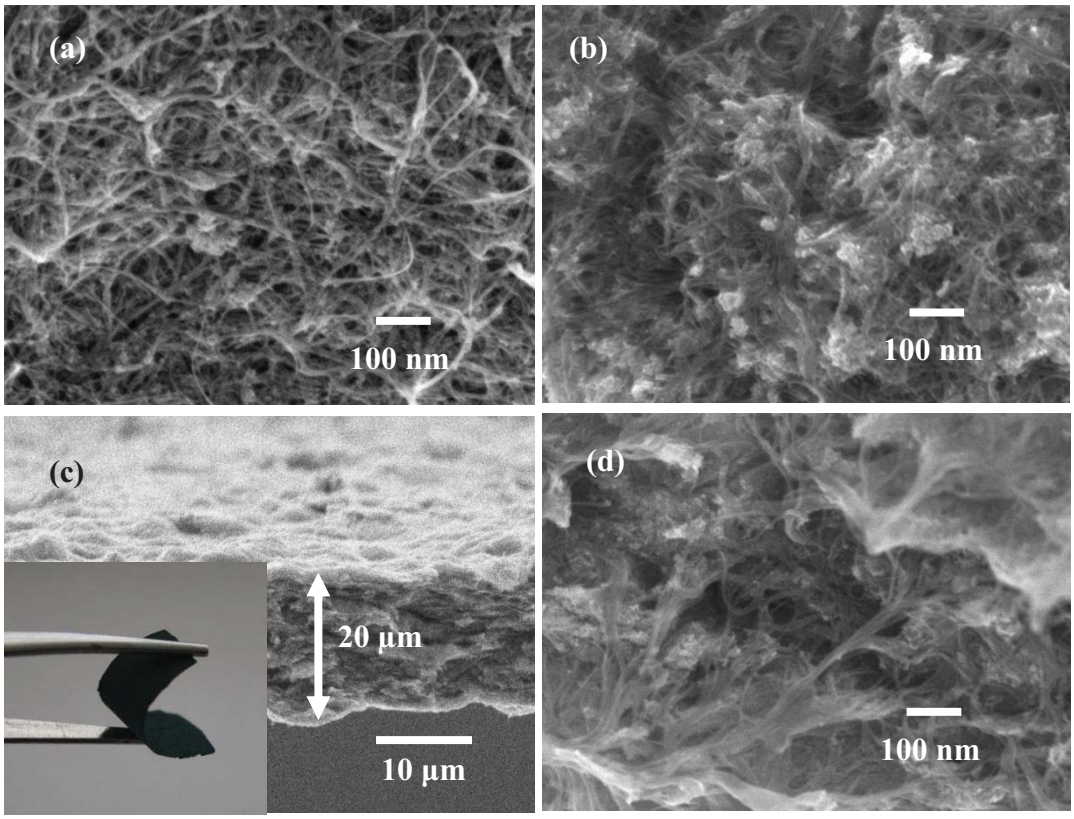

Figure 5.3 FESEM images: top views of free-standing SWCNTs (a) and SWCNT/SnO_2 anode paper (b); cross-sectional views of free-standing SWCNT/SnO_2 anode paper at low magnification (c) and at high magnification (d). Inset of (c) is a photograph of the SWCNT/SnO_2 anode paper.

Fig. 5.3(a) shows single and bundled SWCNTs, which have diameters around 10 – 15 nm and are several micrometres in length. The image of the SWCNT/SnO_2 paper shows that some SnO_2 particles are deposited onto the surface of the SWCNTs in selected sites, with particle sizes in the range of 1 - 5 nm, as shown in Fig. 5.3(b). The cross-sectional FE-SEM images of the SWCNT/SnO_2 paper in Fig. 5.3(c) and (d) demonstrate that the CNTs form a 3D network with webs of curved nanotubes in dense and well packed layers and that the total thickness of the paper is around 20 μm. The SnO_2 nanoparticles are clearly visible and attached to the SWCNT matrix in selected areas. The inset of Fig. 5.3(c) shows a photograph of the SWCNT/SnO_2 paper held by tweezers, indicating the good flexibility.

In the case of the SWCNT/SnO_2 sample, the polyol method can typically produce nanosize SnO_2 particles [266]. In order to confirm the presence of SnO_2 nanoparticles in the anode paper, TEM samples were prepared by removing a small piece of the anode paper and mounting it onto a folding copper mesh oyster grid. Fig. 5.4 shows TEM images of the SWCNT/SnO_2 sample. Low magnification TEM imaging (Fig. 5.4(a)) revealed clumps of small particles coating the surfaces of the carbon nanotubes bundles, with the ultra-fine particle size and tetragonal SnO_2 crystal structure confirmed by the indexed fine spotty ring in the selected area electron diffraction pattern (inset of Fig. 5.4(a)). Higher magnification imaging (Fig. 5.4(b) - (d)) revealed that the crystallite sizes of most SnO_2 crystals were slightly less than 5 nm. The SWCNTs are commonly grouped together into bundles with the SnO_2 particles attached to the outside. Both individual SWCNTs and tangled CNTs are commonly wrapped around the surfaces of these bundles, as shown in Fig. 5.4(c).

High resolution TEM (HRTEM) imaging (Fig. 5.4(d) inset) confirmed that nearly all the SnO_2 particles were attached to each other and to the surfaces of the nanotubes.

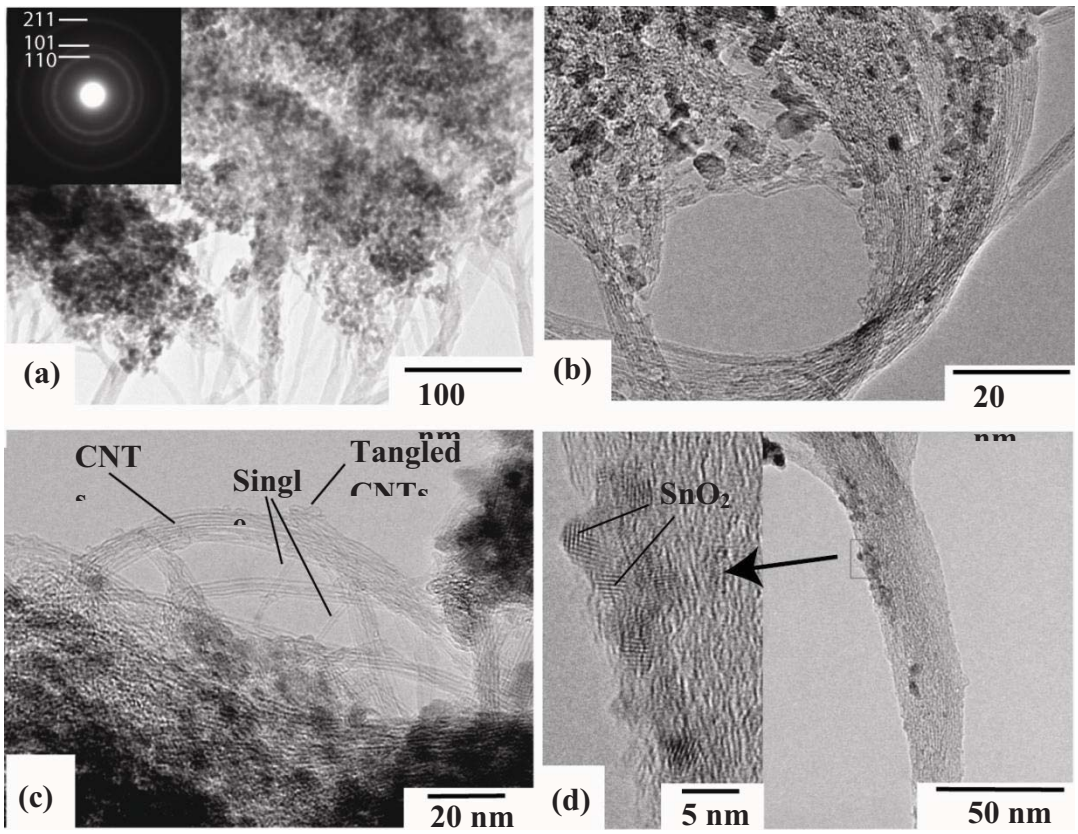

Figure 5.4 Morphological and microstructural features of the SWCNT/SnO_2 sample from TEM images: (a) low magnification image and selected area electron diffraction pattern indexed according to tetrahedral SnO_2 (inset); (b) distribution of SnO_2 along bundles of SWCNTs; (c) SWCNT bundles plus isolated and tangled SWCNTs; (d) SnO_2 particles attached to a tangled bundle of SWCNTs with high resolution image of indicated area in inset

Cyclic voltammetry (CV) measurements were performed to examine the electrochemical properties of the SWCNTs and the SWCNT/SnO_2 paper during the charge-discharge process. The alloying and de-alloying processes of lithium with SnO_2 and SWCNTs were carried out over the potential range of 2.0 – 0.01 V versus Li/Li^+ at a scanning rate of 0.05 mV s^{-1}, as shown in Fig. 5.5. The SWCNT reduction process shows that the peak at 0.65 V vs. Li/Li^+ is attributable to the formation of the solid electrolyte interphase (SEI) layer [332], as shown in Fig. 5.5(a). The SWCNT sample exhibits a broad SEI formation peak, indicating that the kinetics of the SEI formation is low. An extra peak at 1.2 V is clearly observed for the SWCNT sample and is attributed to the reduction of surface species containing oxygen [30, 35]. The CV curves for the SWCNT/SnO_2 paper clearly indicate an irreversible reaction during the first discharge, with a reduction peak in the range of 1.1 - 1.2 V, as shown in Fig. 5.5(b) and (c). Courtney et al. [333] reported that tin dioxide reacts with lithium in a two-step process, as follows:

$$SnO_2 + 4Li^+ + 4e^- \rightarrow Sn + 2Li_2O \qquad (5.1)$$

$$Sn + xLi^+ + xe^- \leftrightarrow Li_xSn, (0 \leq x \leq 4.4) \qquad (5.2)$$

The reduction peak in the range of 0.9 - 1.0 V can be ascribed to the formation of Sn metal in the Li_2O matrix (Eq. 5.1), which only happens in the first discharge cycle [323, 334-336]. The sharp negative-going peak at 0.65 V vs. Li/Li^+ is attributed to Li ion intercalation into the graphitic-type layer, as in the CV curves of the pristine SWCNTs. Further cycling led to very sharp and almost identical reduction peaks below 0.5 V and an oxidation peak at 0.5 V. These peaks correspond to the reversible formation of Li_xSn alloys ($0 \leq x \leq 4.4$) (Eq. 5.2) [323, 334-336]. The cycling stability

after 5 cycles of the SWCNT/SnO_2 paper seems to be fairly stable, because the high content of SWCNTs in the sample provides a good conductive matrix for SnO_2 and can also alleviate the volume changes in SnO_2 during alloying and de-alloying processes.

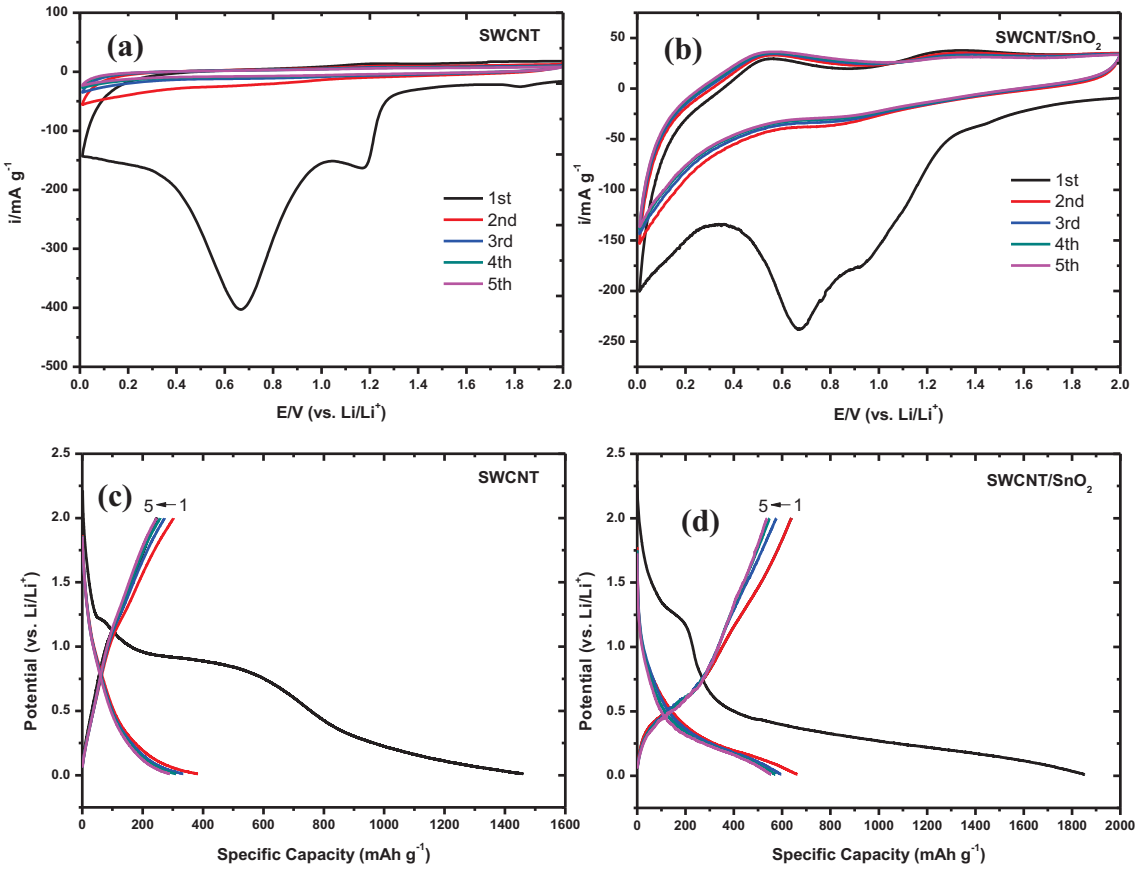

Figure 5.5 Cyclic voltammograms for the first 5 cycles: (a) SWCNTs, (b) SWCNT/SnO_2 anode paper, all at a scan rate of 0.05 mV s^{-1}; and charge-discharge voltage profiles for selected cycles: (c) SWCNTs and (d) SWCNT/SnO_2 anode paper at constant current density of 25 mA g^{-1}.

Fig. 5.5(c) and (d) shows the charge and discharge voltage profiles for the SWCNTs and SWCNT/SnO_2 paper, respectively. The voltage for the SWCNT

sample dropped rapidly and formed a plateau at about 0.75 V during the first discharge process, which was attributed to the decomposition of the electrolyte (the formation of the SEI film) [321, 337]. Subsequently, the voltage gradually decreased, delivering a sloping discharge curve at about 0.15 V, with specific discharge capacity as high as 1459 mAh g^{-1}, while for the SWCNT/SnO_2 sample, the discharge capacity could reach up to 1851 mAh g^{-1}. In the SWCNT/SnO_2 sample, the position of the first voltage plateau is shifted to between 1.1 - 1.2 V, which corresponds to the formation of Sn metal in the Li_2O matrix [323, 334-336]. In the voltage range of 1.1 - 1.2 V, no wide plateau is present, and it is only observed that the drop in the potential changes rapidly in the region of 0.5 - 1.25 V, as shown in Fig. 5.5(d). Moreover, a flat plateau is observed at low potential (< 0.5 V), which is attributed to the formation of Li_xSn, as described in Equation (5.2). During the charge process, prominent voltage plateaus appear at about 0.5 V for the SWCNT/SnO_2 sample, which is attributed to the release of lithium ions when the Li_xSn decomposes (Eq. 5.2). All these data agree with the cathodic and anodic peak potentials in the cyclic voltammograms.

The discharge capacity versus the number of cycles for cells made from the SWCNT and SWCNT/SnO_2 paper is shown in Fig. 5.6(a). It can be seen that the discharge capacity is maintained above 187 mAh g^{-1} and 454 mAh g^{-1} beyond 100 cycles for SWCNT and SWCNT/SnO_2 paper, respectively. The results show that the discharge specific capacity of the SWCNT/SnO_2 paper is superior to that of the SWCNTs (187 mAh g^{-1}) because SnO_2 nanoparticles as the active second phase contribute to enhancing the capacity performance of the electrode during cycling. It is well known that the capacity loss in SnO_2 is caused by stress-induced material

failure arising from the volume changes in the charge and discharge cycling processes. The SWCNTs in the hybrid sample are useful, however, for keeping the SnO_2 nanoparticles in good electronic contact and conferring the ability to accommodate the volume changes. The excellent electron and ion transfer kinetics associated with CNTs also contributes to the superior electrochemical performance of the SWCNT/SnO_2 by lowering the internal resistance for both electrons and lithium ions, so as to facilitate the de-alloying reaction over the small surface area of the SnO_2 particles [328].

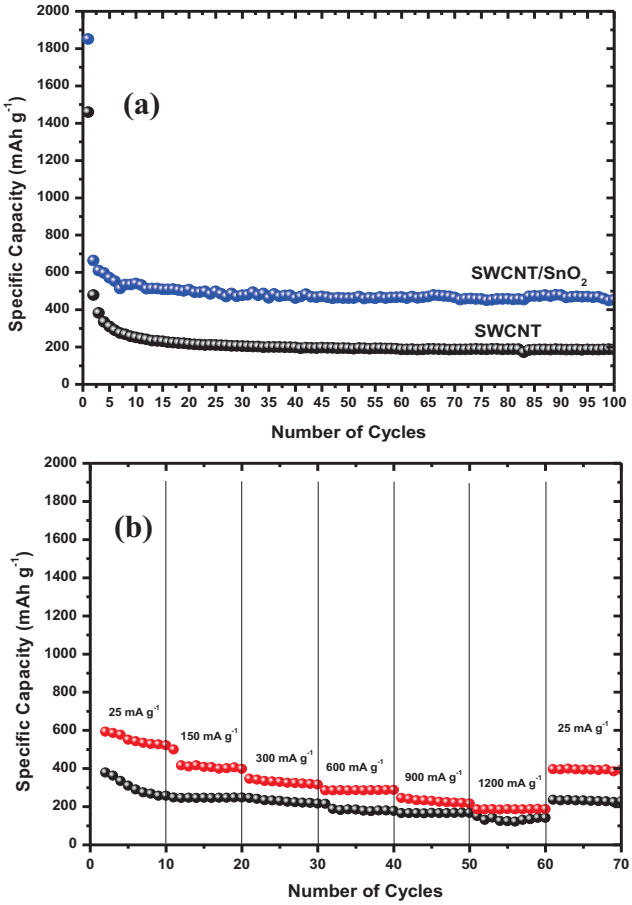

Figure 5.6 (a) Cycling stability of SWCNT and SWCNT/SnO_2 anode paper electrodes at constant current density of 25 mA g^{-1}; (b) high rate capability of the SWCNT/SnO_2 anode paper.

Even though the volume expansion still occurs, the electrode is not pulverized, as is clear from Fig. 5.6(b). On the other hand, the specially designed free-standing film materials, integrating the active materials and the current collector into the one flexible film, can prevent loss of the electrical contact between the active materials and the substrate, which normally occurs for the conventional electrode [338]. The high rate capability of the free-standing, binder-free SWCNT/SnO_2 electrode during cycling is demonstrated in Fig. 5.6(b). The flexible binder-free SWCNT/SnO_2 electrode shows slight decreases in the specific capacity as the current density is increased, unlike the SWCNT electrode, the response of which remains relatively stable, however, the SWCNT/SnO_2 electrode still shows larger capacity at each individual current density, about 186 mAh g^{-1} at a current density of 1,200 mA g^{-1}, compared to the SWCNT electrode. The reason would be the nature of the SnO_2 that was coated on and loaded into the surface of the SWCNTs, as shown in the TEM images (Fig. 5.4). The composite can alleviate the capacity loss but cannot prevent the capacity fading at high current density.

Therefore, in order to verify the electronic conductivity of the SWCNT/SnO_2 paper, electrochemical impedance spectroscopy (EIS) measurements were carried out on the SWCNT/SnO_2 sample using a sine wave of 10 mV amplitude over a frequency range of 100 kHz – 0.01 Hz. To achieve stable SEI formation and the percolation of electrolyte through the electrode materials, the impedance measurement was performed after running charge-discharge for 5 cycles and 100 cycles at a discharge potential of 0.5 V vs. Li/Li^+.

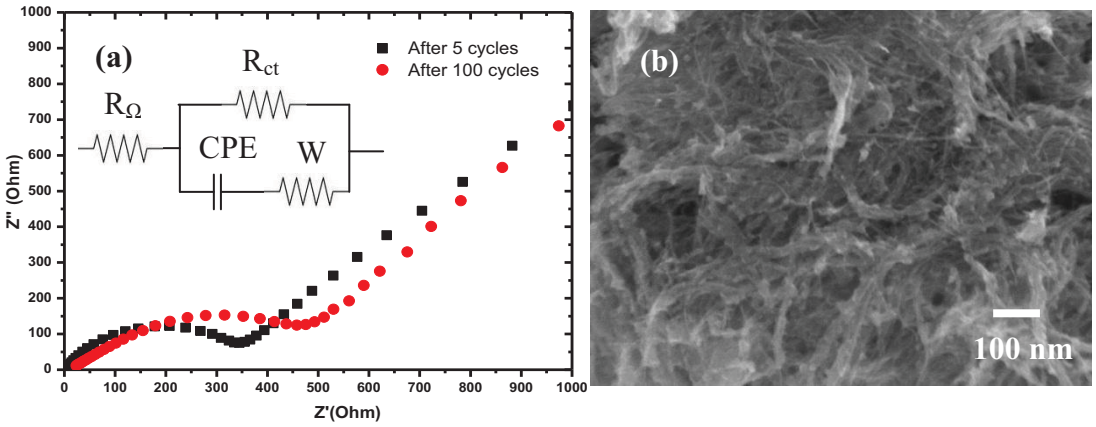

Figure 5.7 Nyquist plots of the cells containing the SWCNT/SnO_2 electrodes after 5 and after 100 charge-discharge cycles at a discharge potential of 0.5 V vs. Li/Li^+. The inset is the equivalent circuit model. (b) FE-SEM image of SWCNT/SnO_2 anode paper after 100 cycles.

Table 5.1 Impedance parameters calculated from equivalent circuit model.

Electrode Materials	Cycles	R_Ω (Ω)	R_{ct} (Ω)
SWCNT/SnO_2	5	1.2	393.98
	100	19.76	601.15

Fig. 5.7 shows the Nyquist plots obtained from the SWCNT/SnO_2 samples after the 5^{th} and 100^{th} cycle tests. An equivalent circuit model was constructed to analyze the

impedance spectra, as shown in the inset to Fig. 5.7(a). The intercept at the Z_{real} axis at high frequency corresponds to the ohmic resistance (R_Ω), which represents the total resistance of the electrolyte, separator, and electrical contacts. The depressed semicircle in the middle frequency range relates to the charge transfer resistance (R_{ct}). CPE is the constant phase-angle element, involving double layer capacitance. The inclined line at lower frequency represents the Warburg impedance (W), which is associated with Li-ion diffusion in the SnO_2 particles. Table 5.1 shows the parameters of the equivalent circuit for the SWCNT/SnO_2 sample after fitting the diameter of the semicircular curve. It is found that the size of the depressed semicircle in the middle frequency range for the SWCNT/SnO_2 sample after 5 cycles is smaller than for after 100 cycles, revealing lower charge transfer resistance (R_{ct} = 393.98 Ω) in the SWCNT/SnO_2 sample. This indicates that the electronic conductivity of the SWCNT/SnO_2 sample at initial cycling was enhanced due to the SWCNTs and the good dispersion of the tin particles at the surface of these SWCNTs, which protected the particles from agglomeration during the initial cycling process. After 100 cycles, however, the electronic conductivity of the SWCNT/SnO_2 sample appears slightly lower than in the initial cycles due to the formation of agglomerates on a small scale, decreasing the surface area of the interparticle contact of the tin particles at the surface of the SWCNTs [339-340], as is shown in the FE-SEM image of Fig. 5.7(b).

Bending-state electrochemical tests on the free-standing electrode were conducted using a flexible and bendable cell, as shown in Fig. 5.8(a). To understand the electrochemical behaviour of free-standing electrodes under bending, the flexible

and bendable cell was tested when it was bent inwards to 180° (Fig. 5.8(b)). The capacity of the bent cell is slightly lower compared with the cell that was not subjected to bending (Fig. 5.8(c)). In order to explore the reason, the conductivity of the cell before and after bending was measured by EIS, as shown in Fig. 5.8(d). The results show that the application of a tensile stress decreased the conductivity of the electrode [341]. After bending, the conductivity of the cell was 4.8×10^{-4} S·m^{-1}, which is slightly lower than that of the unbent cell (11.6×10^{-4} S·m^{-1}).

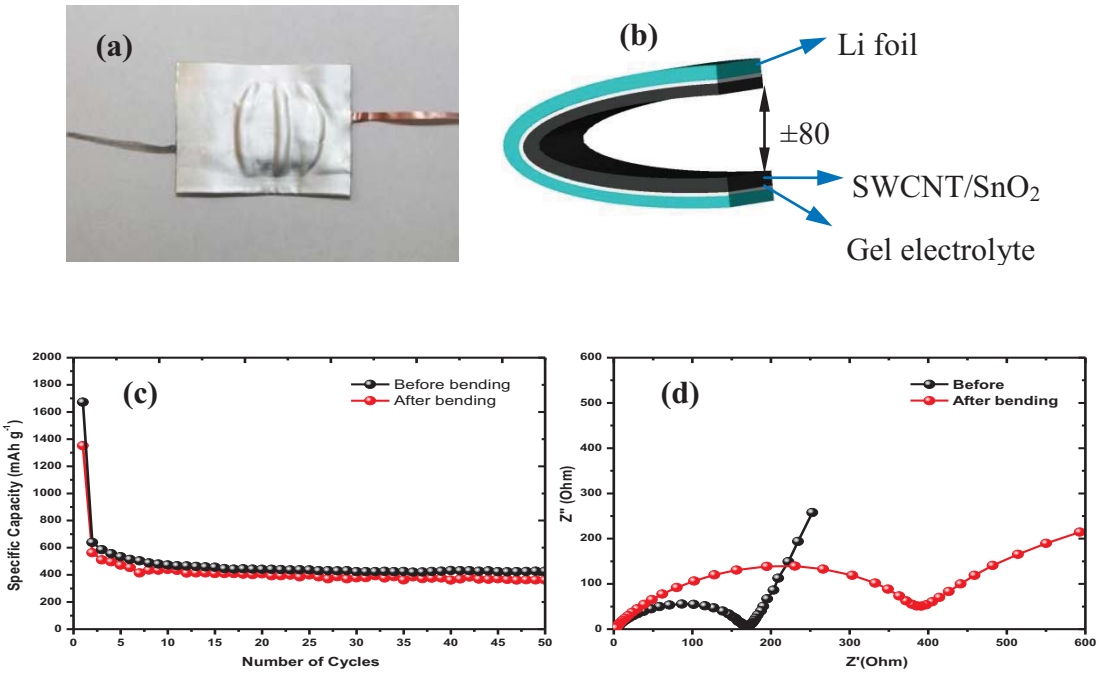

Figure 5.8 (a) Photograph of a flexible and bendable cell, (b) schematic of cell bent inwards at 180°, (c) cycling stability before and after inward bending of SWCNT/SnO_2 electrode at constant current density of 25 mA g^{-1}, and (d) Nyquist plots of the cells containing the SWCNT/SnO_2 electrodes before and after bending.

Although the conductivity of the bent cell decreased, the free-standing electrode still functions well. This suggests that the strain associated with the bending radius is not sufficient to physically crack the working electrode, and therefore, the structure of the free-standing electrode is not significantly altered by the bending test.

5.4 Conclusions

Free-standing SWCNT/SnO_2 anode paper was prepared by vacuum filtration of SWCNT/SnO_2 hybrid material, which was synthesized by the polyol method. In the SWCNT/SnO_2 paper, the CNTs form a 3D nanoporous network structure, with SnO_2 particles deposited onto the surface of the SWCNTs in selected sites. The SWCNT/SnO_2 paper shows high specific discharge capacity, as great as 454 mAh g^{-1} at a current density of 25 mA g^{-1}, and very stable cycling stability up to 100 cycles compared to the pristine SWCNT paper, due to the intrinsic nature of the combination of nanosized SnO_2 as an active second phase to provide high capacity and CNTs as flexible mechanical support with high electric conductivity. Bending the SWCNT/SnO_2 electrodes to extremely small radii of curvature has a minimal effect upon the electrochemical behaviour, reflecting only a small increase in their electrical resistance. Additionally, the electrochemical performance was not adversely impacted by the bending test. These results illustrate the robust nature of free-standing SWCNT/SnO_2 electrodes and their promise for flexible Li-ion batteries.

Chapter 6

Impact of Mechanical Bending on the Electrochemical Performance of Bendable Lithium Batteries with Paper-like Free-Standing V_2O_5-Polypyrrole Cathodes

6.1 Introduction

With recent advances in the technology of various types of flexible portable electronic equipment, such as roll-up displays and medical devices, there has been a strong market demand for small, thin, lightweight, and bendable batteries to power them. Furthermore, wearable electronics, such as wearable displays, embedded health monitoring devices, and wearable military devices also require lightweight and wearable batteries [6, 75, 252, 313]. Conventional lithium batteries, however, typically consist of a positive electrode and a negative electrode spaced by a separator, which is soaked with an electrolyte solution. Each electrode is formed from a metal substrate that is coated with a mixture of an active material, an electrical conductor, and a binder. This kind of electrode is not suitable for flexible or bendable batteries because a metal substrate is used to hold the active materials. The active material layers will be cracked or peeled off the substrate when they are bent frequently. To avoid these drawbacks, mechanically flexible, soft, and free-standing electrode materials are required [253, 256, 342-345].

There are a number of studies on preparing flexible electrodes for lithium ion battery application. Varta Microbattery has developed a new generation of thin

polymer batteries, PoLiFlex™, with a polymer electrolyte based on a polyvinylidene fluoride (PVDF)-copolymer binder matrix [78]. Using this technique, Dennler and co-workers have developed a thin (<1 mm), lightweight (<10 g) and flexible photovoltaic (PV) solar battery module [346].Carbon-based "bucky" paper also has been studied for the preparation of flexible anode materials [35, 342, 345]. Graphene, carbon nanotubes (CNTs), and their composites have all been proposed and investigated for use as anode materials, but the challenge has remained to find a suitable substrate-free cathode material for lithium ion batteries. Unlike carbon based anodes, conventional cathode materials (e.g., $LiFePO_4$ and $LiCoO_2$) are brittle ceramics that are difficult to form into a flexible, free-standing structure. Hence, a flexible and free-standing cathode material with excellent electrochemical performance has remained to be discovered.

Recently, two research groups at the University of Wollongong (Australia) and Tsinghua University (China) have reported flexible free-standing VO_2(B) and V_2O_5 nanowire films that were tested as cathode materials for lithium batteries [253, 347]. The free-standing electrode materials showed acceptable performance, however, the free-standing materials were tested using coin type cells under normal conditions without any bending. As the free-standing materials are designed for bendable or wearable batteries, it is important that the materials be tested under bending conditions. Therefore, in this Chapter, a soft bendable cell which consists of a free-standing V_2O_5-polypyrrole (PPy) cathode, a lithium foil anode, and gel polymer electrolyte is reported.

The V_2O_5-PPy composite was synthesized by coating PPy on V_2O_5 nanowires. Polypyrroles have been extensively studied as cathode materials for

rechargeable batteries because of their superior electroactivity, good electrical conductivity, and chemical stability [348-350]. PPy has also been used as an additive in electrode materials for battery application to improve the conductivity and to reduce the dissolution of active materials into the electrolyte [351-354]. Based on our previous experience with PPy, we have designed and prepared free-standing V_2O_5-PPy cathode materials based on the following ideas:

(i) A conductive PPy coating on the surface of V_2O_5 nanowires can improve the conductivity of the free-standing electrode. At the same time, PPy can also act as a binder, increasing the contact between the wires [355] and improving their mechanical properties.

(ii) The conducting polypyrrole serves not only as a conducting agent to improve the conductivity of free-standing electrode materials, but also as an electrochemically active material to contribute to the capacity. Therefore, using PPy as an additive is better than using some other inert additive, such as carbon nanotubes (CNTs).

(iii) PPy nanoparticles coated onto the surface of V_2O_5 powder may absorb V_2O_5 due to their porous surface morphology and reduce the dissolution of the V_2O_5 into the electrolyte. Consequently, the V_2O_5 utilization and durability under cycling were improved [356-357].

In practical utility, the bendable and flexible lithium batteries have to maintain both their electrochemical and their mechanical performance during daily operation. In this Chapter, we report the influence of mechanical bending on the electrochemical behaviour of bendable lithium batteries consisting of a free-standing V_2O_5-PPy cathode film, gel electrolyte, and a lithium foil anode.The electrochemical

performances of the novel bendable cells were tested under repeated bending. Our data indicated that novel bendable cells can be bent to small radii of curvature and still function well.

6.2 Experimental procedures

6.2.1 Synthesis of V_2O_5 nanowires and V_2O_5-PPy composite

The hydrothermal method [358-359] was adopted and modified in this Chapter to control the length of nanowires for the preparation of free-standing V_2O_5films. 0.360 g V_2O_5 powder (98%, Reidel De Haën) was dissolved in 30 ml deionized water and 5 ml 30 % H_2O_2 (Sigma Aldrich), and mixed under vigorous magnetic stirring at room temperature until a transparent orange solution was obtained. The resultant solution was then transferred to a 125 ml autoclave and kept in an oven at 200 °C for 24 hours. After naturally cooling to room temperature, the product was washed several times with distilled water.

The V_2O_5-PPy composite was prepared by adding 0.05 M tetrabutylammonium hexafluorophosphate and 0.06 M distilled pyrrole monomer into the solution containing 2 mg/ml V_2O_5 nanowires. The mixture was stirred until the gradual change of colour from light black to deep black indicated the formation of PPy. The reacted mixture was then kept under the same conditions for 24 h. The synthesized samples were centrifuged and rinsed several times with distilled water and ethanol.

6.2.2 Preparation of free-standing V_2O_5andV_2O_5-PPy films

To make a uniform film, a modified vacuum filtration technique was adopted [271], where a 300 ml filter funnel (Glasco) was used. In a typical procedure, 20 mg of V_2O_5-PPy material was dispersed into 1 wt% Triton X-100 surfactant (Sigma-Aldrich) in 50 ml distilled water. The suspension was then ultrasonically agitated using a probe sonicator for 1 minute. The as-prepared suspension was poured into the funnel and filtered through a porous polyvinylidene fluoride (PVDF) membrane (Millipore, 0.22 μm pore size, 47 mm in diameter) by positive pressure from a vacuum pump. The solvent passed through the pores of the membrane, but the V_2O_5-PPy material was trapped on the membrane surface, forming a mat. The resultant mat with its PVDF membrane was then washed twice using distilled water, followed by ethanol to remove any remaining solvent. The mat with the PVDF membrane still attached was dried in an oven for 2 hours and then was peeled off the membrane.

6.2.3 Preparation of gel polymer electrolyte and fabrication of bendable cell

Poly(vinylidenefluoride-co-hexafluorpropylene) (P(VDF-HFP)) was used as received from Sigma-Aldrich. *N*-methylpyrrolidinone (NMP) and nanoscale Al_2O_3 powders with an average particle size of 30 nm were obtained from Sigma-Aldrich. 1 M $LiPF_6$ solution in ethylene carbonate (EC)–dimethyl carbonate (DMC) was purchased from Merck Co. and used without any treatment. A porous film was prepared by the liquid–liquid extraction process [272]. A certain amount of P(VDF-HFP) was dissolved in NMP at 50 °C. Then, the nanoscale Al_2O_3 particles were added to the viscous solution and agitated with an ultrasonic stirrer. The resulting slurry was cast onto the surface of the free-standing V_2O_5-PPy electrode and dried

under vacuum at 80 °C for 8 h. After evaporation of the NMP, the electrode with gel electrolyte precursor was soaked in a 1 mol/L solution of $LiPF_6$/EC–DMC (volume 1:1) for 1 h. The surface of the electrode with gel electrolyte was wiped clean with filter paper, and then fabricated into flexible bendable cells with lithium foil as the counter electrode. Flexible and soft aluminium laminated pack materials (provided by DLG Battery Co., Ltd, Shanghai, P.R. China) were used to assemble the bendable cells. Fig. 6.1 contains a schematic diagram of a typical flexible and bendable cell for bending-state electrochemical testing.

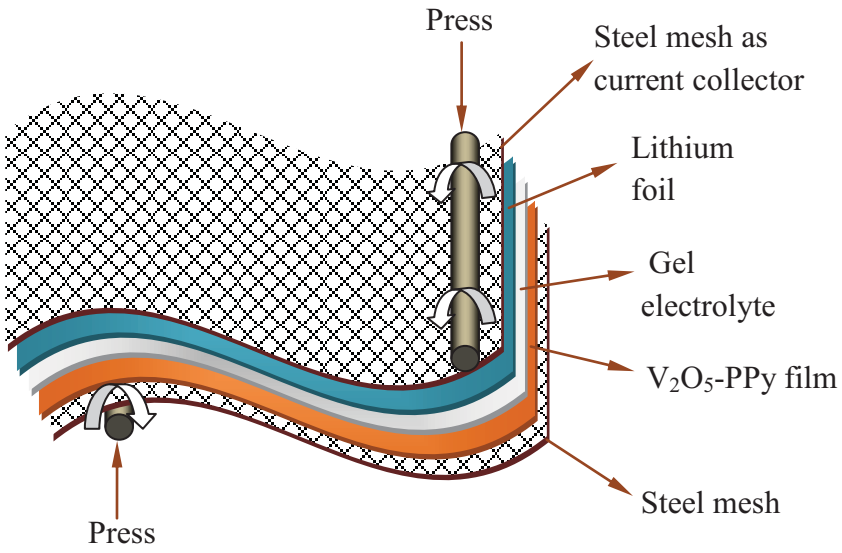

Figure 6.1 Schematic diagram of flexible cell for bending-state electrochemical testing.

6.2.4 Structure and morphology analysis, and mechanical property testing

X-ray diffraction (XRD) data were collected on a GBC MMA generator and diffractometer with Cu K_α radiation. For infrared (IR) spectroscopy, the samples

were mixed with KBr powder, placed in a sample holder, and measured using a Shimadazu IRPrestige-21 Fourier transform IR (FT-IR) spectrometer. KBr was used as the background file. All spectra were measured from 2000 to 400 cm^{-1}, and the number of scans was typically 10, with a resolution of 2 cm^{-1}. The amount of PPy in the sample was estimated using a thermogravimetric analysis/ differential scanning calorimetry (TGA/DSC) 1 Star^{e} System. The morphologies of the films were investigated by field emission scanning electron microscopy (FESEM, JEOL JSM-7500FA) and transmission electron microscopy (JEOL 2011, 200 kV). The mechanical properties of the free-standing films were investigated with a Shimadzu EZ-S Universal Testing Machine. Tensile tests were conducted under a fixed stretching speed of 1 mm min^{-1} for all specimens. The dimensions of specimens were 5 mm in width and 30 mm in length.

6.2.5 Electrochemical measurements

The free-standing electrodes were tested in coin-type cells to confirm the initial electrochemical performance. CR 2032 coin-type cells were assembled in an Ar-filled glove box (Mbraun, Unilab, Germany) by stacking a porous polypropylene separator containing liquid electrolyte between the V_2O_5-PPy free-standing film electrode and the lithium foil counter electrode. The electrolyte used was 1 M $LiPF_6$ in a 50:50 (v/v) mixture of ethylene carbonate (EC) and dimethyl carbonate (DMC), provided by MERCK KgaA, Germany. The bendable cells were also assembled in the glove box with free-standing V_2O_5-PPy cathode, lithium foil anode, and gel electrolyte. Charge-discharge tests were carried out with a battery testing device (Land Battery Tester) interfaced to a computer with software. The system is capable

of switching between charge and discharge automatically according to the pre-set cut-off potentials. The cells were cycled between 1.5 and 4.0 V with a constant current of 40 mA g^{-1}. Their change in conductivity after each repeated bending was examined by electrochemical impedance spectroscopy (EIS) measurements using a sine wave of 10 mV amplitude over a frequency range of 100 kHz – 0.01 Hz.

6.3 Results and discussion

Fig. 6.2(a) shows the X-ray diffraction (XRD) patterns of the V_2O_5 film, the V_2O_5-PPy film, and commercial V_2O_5. All the diffraction peaks can be indexed as orthorhombic V_2O_5 phase with the lattice parameters a = 11.54 Å, b = 3.571 Å, and c = 4.383 Å, in good agreement with the literature (JCPDS card no. 89-0612). No characteristic peaks of any impurities were detected in these patterns. Compared to the commercial V_2O_5, the relatively strong intensities of the (200) and (400) diffraction peaks of the V_2O_5 nanowires indicates that there is a preferred distribution of planes parallel to the *a*-direction. The formation of orthorhombic V_2O_5 single crystalline nanowires is likely related to the layered structure of $V_2O_5 \cdot nH_2O$ [360]. V_2O_5 dissolves in distilled water in the presence of H_2O_2 to form an orange solution of diperoxo anions, $VO(O_2)_2(OH_2)^-$. H_2O_2 in excess and peroxo groups are slowly oxidized, giving oxygen gas. Monoperoxo and dimer species are then progressively formed as peroxo groups are decomposed. An aqueous solution of VO_2^+ and $H_2V_{10}O_{28}^{4-}$ is finally obtained [361-362]. At the early stage of hydrothermal treatment of the aqueous solution of VO_2^+ and $H_2V_{10}O_{28}^{4-}$, $V_2O_5 \cdot nH_2O$ fibres with large diameters are obtained due to the condensation of vanadic acid via a homogeneous nucleation and solution growth process. As the reaction proceeds, crystalline V_2O_5 is formed via dehydration and recrystallization of $V_2O_5 \cdot nH_2O$, and

the fibrillar precipitates can be cleaved along their planes due to their large interplanar spacing, so V_2O_5 single-crystalline nanowires are formed.

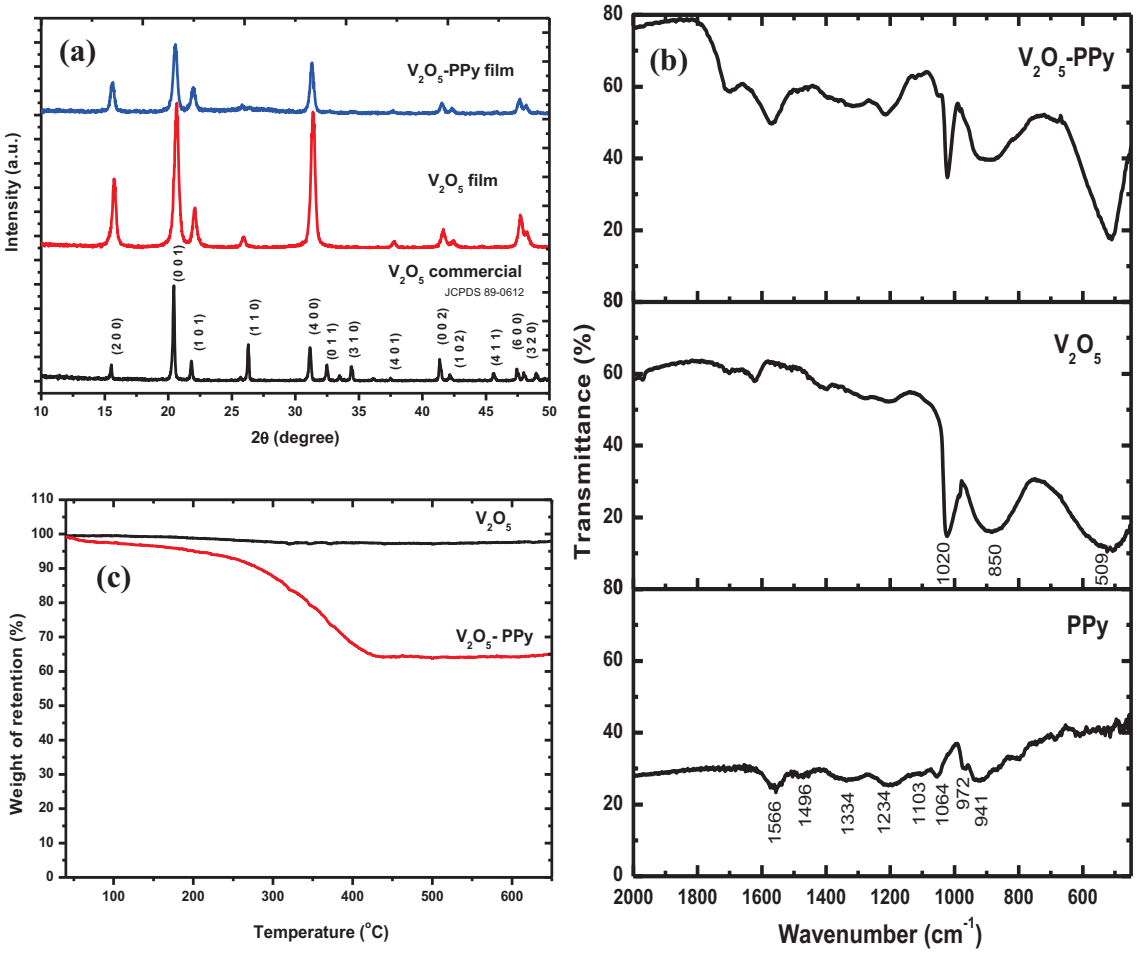

Figure 6.2 (a) XRD patterns of V_2O_5 film, V_2O_5-PPy film, and commercial V_2O_5; (b) FT-IR transmission spectra of V_2O_5-PPy, V_2O_5, and PPy; (c) TGA curves of V_2O_5 and V_2O_5-PPy film.

The FT-IR spectra of the pure PPy and the V_2O_5-PPy film are shown in Fig. 6.2(b). It is clear that the two spectra are similar to each other, indicating that the main polymer chains of the V_2O_5-PPy hybrid are similar to those of PPy. The features at 1566 and 1496 cm^{-1} are attributed to the antisymmetric and symmetric

pyrrole ring vibrations, respectively. The peaks at 1334 and 1064 cm^{-1} are ascribed to the in-plane C–H stretching vibration and in-plane N–H deformation, respectively. The bands at 1234 and 972 cm^{-1} reflect the C–N stretching vibration and the ═ C–H out-of-plane vibration, which implies the doped state of PPy [363-364]. The other peaks, centred at 1103 and 941 cm^{-1}, are assigned to the hydroxyl group peaks. For the V_2O_5-PPy hybrid, besides the above characteristic peaks belonging to PPy, the vibration modes of V_2O_5 were detected. The peaks at 1020, 850, and 509 cm^{-1} are attributed to the terminal oxygen symmetric stretching mode (v_s) of V=O and the bridge oxygen asymmetric and symmetric stretching modes (v_{as} and v_s) of V-O-V, respectively [364-366]. In addition, some minor spectroscopic differences and displacements were observed, which showed that there was physical interaction between polypyrrole and V_2O_5 in the hybrid material.

For quantifying the amount of PPy in the V_2O_5-PPy materials, TGA was carried out in air (Fig. 6.2(c)). The samples were heated from 30 to 650 ^oC at a rate of 10 ^oC min^{-1}. As can be seen from Fig. 6.2(c), the V_2O_5-PPy powders started to lose weight slowly in air with increasing temperature, and maximum weight loss was found to take place around 80 to 400 ^oC, while the bare V_2O_5 powders remained stable over the entire temperature range. As the V_2O_5 powders remained stable over this temperature range, any weight change is believed to correspond to the oxidation of PPy. Therefore, the change in weight before and after the oxidation of PPy directly translates into the amount of PPy in the V_2O_5-PPy film. By the use of this method, it was estimated that the amount of PPy in the V_2O_5-PPy film was approximately 35 wt%.

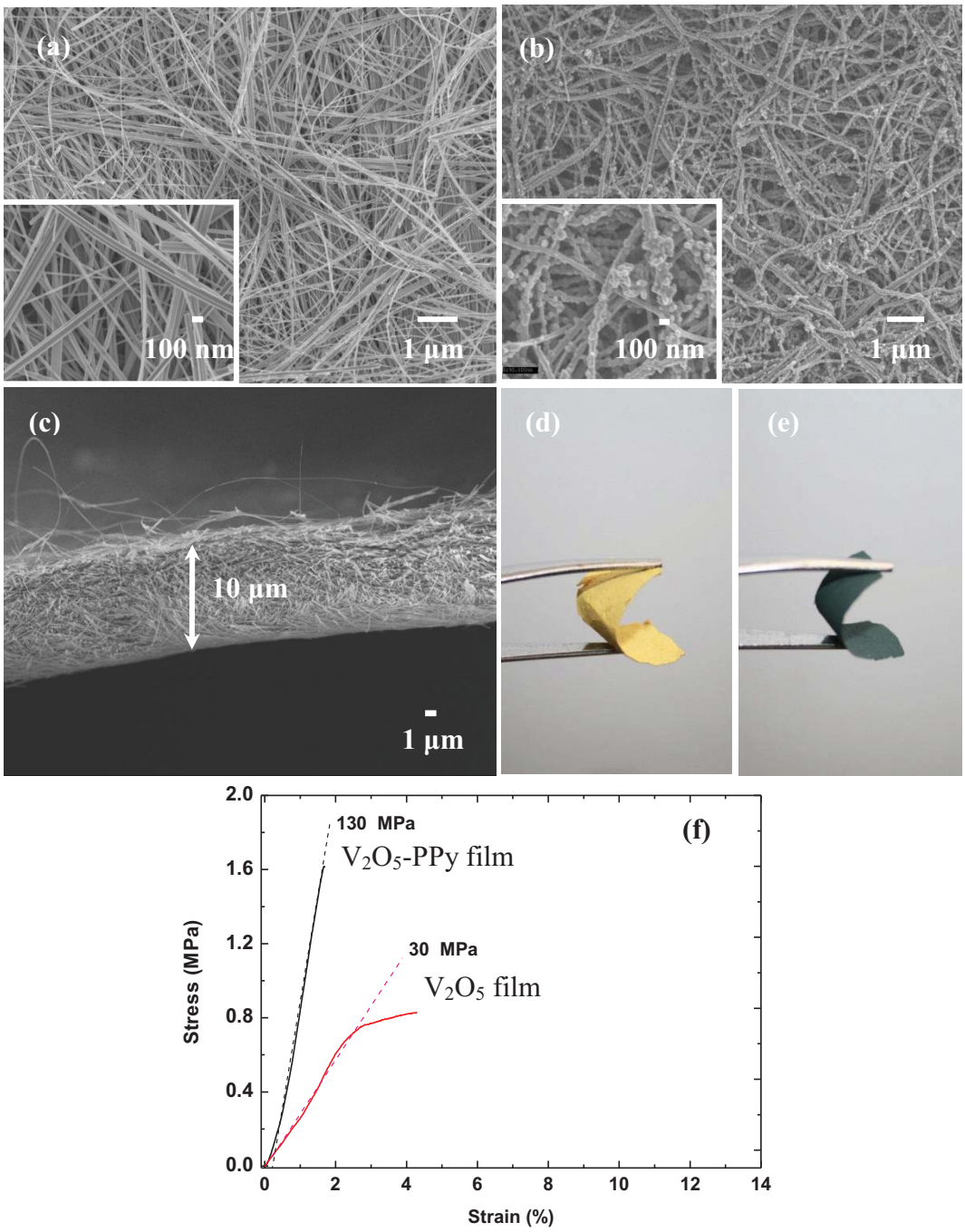

Figure 6.3 FESEM images: top view of free-standing V_2O_5 film (a) and V_2O_5-PPy film (b) with inset high magnification images; cross-sectional view at low magnification of free-standing V_2O_5-PPy film (c). Photographs demonstrating the flexibility of the V_2O_5 film (d) and the V_2O_5-PPy film (e). Stress and strain curves of V_2O_5 and V_2O_5-PPy film samples (f).

FESEM observations of the V_2O_5 and V_2O_5-PPy film are presented in Fig. 6.3. The FESEM image of the pristine V_2O_5 film (Fig. 6.3(a)) shows straight nanowires ~80-120 nm in diameter and several microns in length, resulting in an aspect ratio of ~10^2-10^3. Some of the V_2O_5 nanowires are isolated or grown-together in the form of bundles, as shown in the inset. On the other hand, the V_2O_5-PPy film (Fig. 6.3(b)) shows similar morphology to the V_2O_5 film, with the PPy uniformly deposited throughout entire lengths of nanowires in irregular or spherical shapes. The cross-sectional view of the V_2O_5-PPy film (Fig. 6.3(c)) shows that the V_2O_5-PPy film is composed of very dense web-like nanowires joined together in a well packed layer, with the thickness of the flexible electrode around 10 μm. The pristine V_2O_5 and V_2O_5-PPy free-standing films can be rolled up (Fig. 6.3(d) and (e)) or bent to any curvature, and then returned to their original shape, while still maintaining their useful properties. Fig. 6.3(f) shows the stress-strain curves of flexible V_2O_5 and V_2O_5-PPy film electrodes. The V_2O_5-PPy film (black curve) presents a significantly higher modulus than the pure V_2O_5 film (red curve), indicating that the V_2O_5-PPy could sustain much higher stress compared with V_2O_5 without the PPy coating. This suggests that the PPy coating does improve the mechanical strength and greatly enhances the stiffness of the V_2O_5-PPy, however, the toughness was decreased (as the area under the stress-strain curve for pure V_2O_5 is larger than that for V_2O_5-PPy).

Preliminary TEM investigations revealed additional information concerning the structural and morphological evolution of the samples, as shown in Fig. 6.4. The PPy layer, as revealed in low (Fig. 6.4(a)) and high (Fig. 6.4(b)) magnification images, fairly uniformly coats entire lengths of nanowires. Based on selected area electron diffraction (not shown), it was also clear that the V_2O_5 nanowires exhibit a

well-ordered multilayered structure. High-resolution TEM (HRTEM) imaging of an individual nanowire (Fig. 6.4(b) revealed lattice fringes, in good agreement with orthorhombic V_2O_5 (JCPDS card no. 89-0612). The contrast from the indicated (200) V_2O_5 fringes, is confirmed by the occurrence of spots in the associated fast Fourier transform (inset of Fig 6.4(b)). The fringe contrast is reduced because of the uniform PPy coating. The HRTEM contrast produced by the PPy coating itself (edge of coated nanowire, Fig 6.4(b)) is typical of an amorphous hydrocarbon coating.

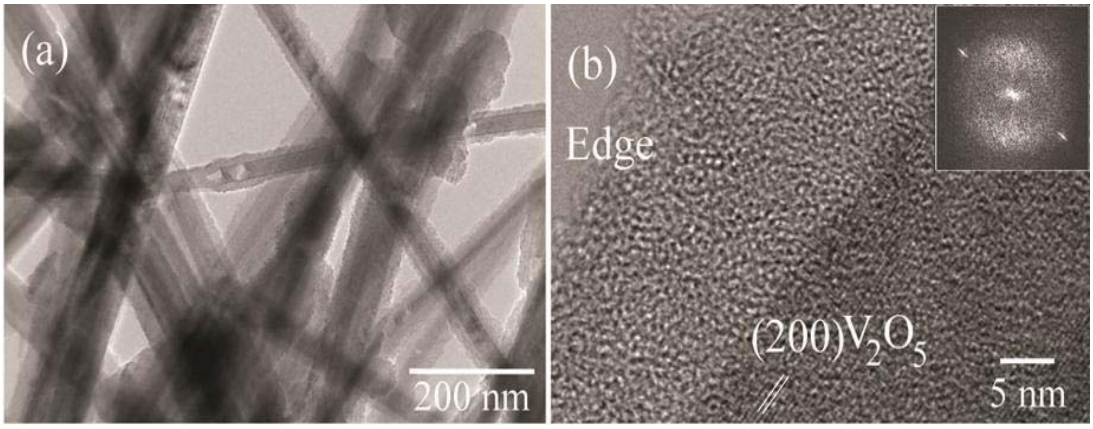

Figure 6.4 TEM images: (a) low magnification image of V_2O_5-PPy film, and (b) HRTEM image of the edge of an individual V_2O_5-PPy nanowire with inset fast Fourier transform

Fig. 6.5 shows selected cycles of charge-discharge curves for the pristine V_2O_5 film and V_2O_5-PPy film electrodes in coin cells at a current density of 40 mA g^{-1} between 1.5 and 4.0 V vs. Li/Li^+. The pristine V_2O_5 and V_2O_5-PPy film electrodes show three discharge plateaus for initial discharge, indicating a similar reaction mechanism for Li^+ ion intercalation into V_2O_5 [102, 367-368] (Fig. 6.5(a) and (b).The voltage plateaus appearing above 3.0 V correspond to the structural

modifications from V_2O_5 to $Li_xV_2O_5$ for up to one equivalent (x = 1) Li^+ insertion. The additional potential plateaus that appear at lower voltage levels around 2.5 V are attributed to the structural modifications related to Li^+ insertion of greater than one equivalent. Further discharge of the batteries leads to the last plateau at approximately 2.0 V, with an electrochemical insertion of up to three equivalents of Li^+ into the lattice and the ensuing formation of $Li_3V_2O_5$ (x = 3 for $Li_xV_2O_5$) during the first discharge process in the extended potential range [369]. The pristine V_2O_5 electrode film (Fig. 6.5(a)) shows a large initial discharge capacity of 430 mA h g^{-1}, but the first charge capacity is low, only 337 mAh g^{-1}, with a coulombic efficiency of around 78 %. The possible reason for such a high discharge capacity may be the larger specific surface area of the V_2O_5 nanowire film electrode. After 100 cycles, the pristine V_2O_5 paper shows a decreased discharge capacity of around 33 mAh g^{-1} and an average coulombic efficiency of 96 %. Fig. 6.5(b) shows typical charge and discharge curves of the V_2O_5-PPy film electrode. The V_2O_5-PPy electrode paper shows an initial discharge capacity of 313 mAh g^{-1}, with a coulombic efficiency of 90 %, which is slightly higher than that of the pristine V_2O_5 paper. The 100^{th} discharge capacity of the V_2O_5-PPy film electrode is 188 mAh g^{-1}, which is much better than that of the pristine V_2O_5 film. It can be observed that the V_2O_5-PPy film electrode has a higher specific capacity than the V_2O_5 film electrode throughout the whole initial discharge curve. Conductive PPy polymer in the V_2O_5-PPy film electrode evidently has aided Li^+ intercalation into the $Li_xV_2O_5$ lattice of the V_2O_5-PPy electrode, by improving both the accessibility of the Li^+ ions and the electrical conductivity [369]. Conductive polymers in theV_2O_5-PPy film electrode can connect isolated V_2O_5 nanowires and give rise to valid conductive networks in the electrodes.

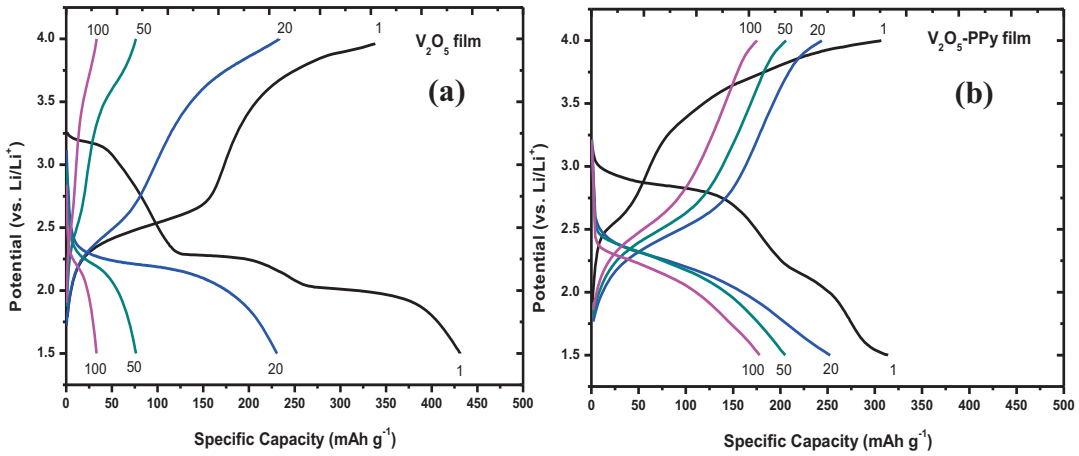

Figure 6.5 Typical charge-discharge voltage profiles for selected cycles of (a) V_2O_5 and (b) V_2O_5-PPy film electrodes at constant current density of 40 mA g^{-1}.

The cycling stabilities of the pristine V_2O_5 and the V_2O_5-PPy film electrodes are shown in Fig. 6.6. The discharge capacity of the V_2O_5 and V_2O_5-PPy film electrodes at the 100^{th} cycle are 33 and 187 mAh g^{-1}, respectively. The cell containing the V_2O_5-PPy film cathode exhibits higher capacity than the one containing the pristine V_2O_5 film cathode. The results show that electrically conductive and electrochemically active organic polymer (PPy) enhances the specific capacity by connecting isolated V_2O_5 nanowires, thus creating valid conductive networks for lithium ions and/or counter anions of the electrolyte for the electrode. This enables increased activation of isolated V_2O_5 nanowires and allows them to be employed for lithium intercalation/de-intercalation in the V_2O_5-PPy film electrode during the battery cycling.

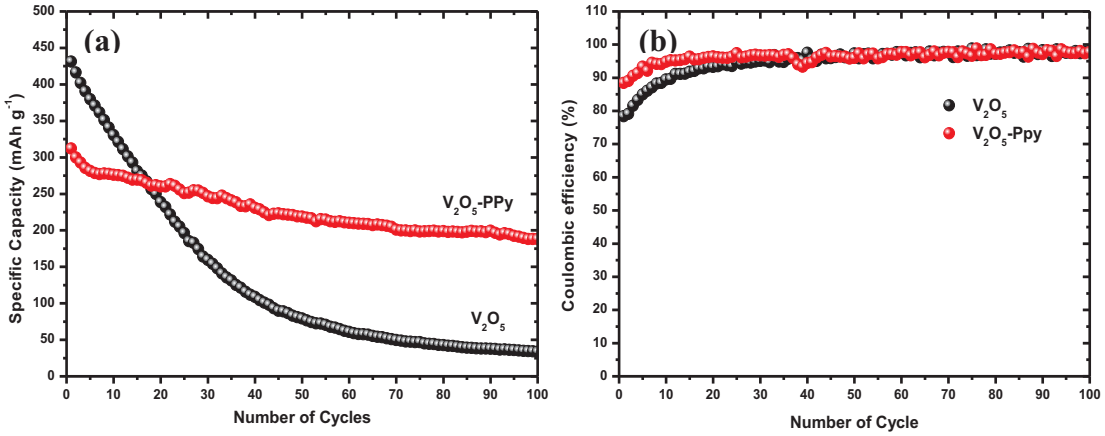

Figure 6.6 (a) Cycling stability and (b) coulombic efficiency of the V_2O_5 and V_2O_5-PPy electrodes at constant current density of 40 mA g^{-1}.

In order to explore the influence of the mechanical bending of flexible V_2O_5-PPy film electrodes on their electrochemical performance, flexible cells were repeatedly bent inward to an angle of 180°. Each flexible cell was bent for up to a total of 10 times, and its capacity and cycling performance were tested for several cycles. Fig. 6.7(a) shows the initial specific discharge capacity (300 mAh g^{-1}) of a cell. After the bending, the capacity is similar to that of the unbent coin cell (313 mAh g^{-1}).These results demonstrate that the electrochemical behaviour of the free-standing electrodes was only slightly influenced by mechanical stress. Further investigations were carried out to explore the influence of repeated bending of flexible V_2O_5-PPy film electrodes on their conductivity by electrochemical impedance spectroscopy (EIS) measurements.

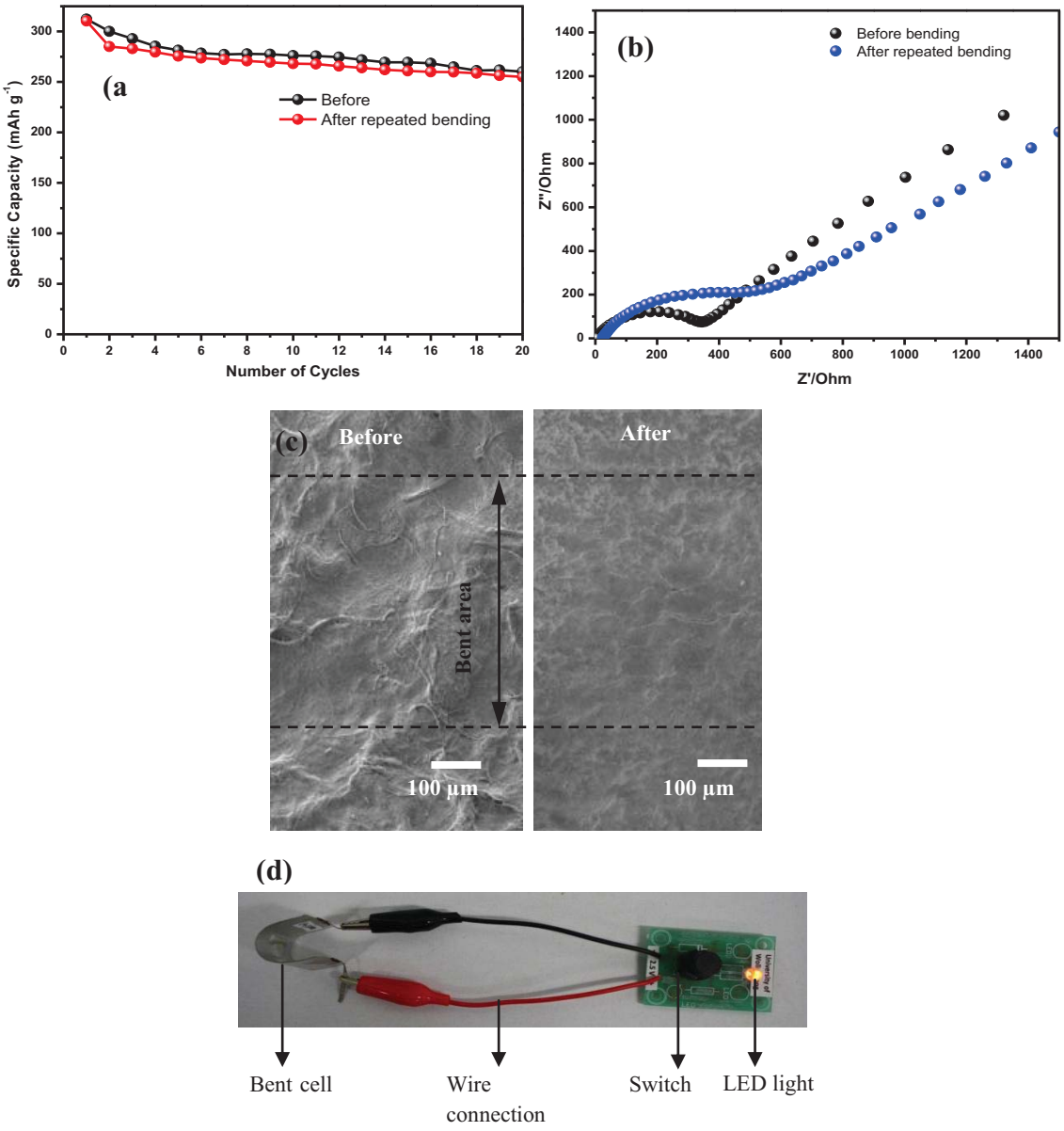

Figure 6.7 (a) Cycling stability of V_2O_5-PPy film electrode under repeated inward bending at constant current density of 40 mA g^{-1}; (b) Nyquist plots of cells containing the V_2O_5-PPy film electrodes before and after bending; (c) FESEM images of sample before and after repeated-bending tests; and (d) photograph of cell bent inwards at 180^o that was used to power a red LED. The LED glowed even when the battery device was bent, and the demonstration could be repeated over several cycles.

EIS tests were carried out before and after the repeated-bending test. Change in conductivity after repeated bending was examined by EIS measurements using a sine wave of 10 mV amplitude over a frequency range of 100 kHz – 0.01 Hz (Fig. 6.7(b)). The results show that the application of bending stress decreased the conductivity of the electrode. After the bending, the conductivity of the cell was 1.74×10^{-4} Sm^{-1}, which is slightly lower than that of the unbent cell (2.73×10^{-4} Sm^{-1}). SEM images of the free-standing V_2O_5-PPy before and after the bending are shown in Fig. 7(c). No cracks were detected in the electrode around the bent area after the bending test. This suggests that the electrode appears to be resistant to repeated bending. A marginal decrease in the conductivity of the bent cell could be due to loose contact between the Li foil anode and the V_2O_5-PPy film after repeated bending. To show the reliability of the flexible cell after the bending test, the cell was used to light up a red light-emitting diode (LED) as shown in Fig. 6.7(d).

6.4 Conclusions

In this Chapter, free-standing flexible V_2O_5-PPy film electrode has been prepared by the vacuum filtration method. Electrochemical measurements showed that the V_2O_5-PPy film delivered a significantly higher reversible capacity than the pristine V_2O_5 film and excellent cycling stability (187 mA h g^{-1} at a current density of 40 mA g^{-1} after 100 cycles), which is higher than that of the pristine film. The hybrid material, consisting of a layer-structured metal oxide and a conducting polymer, promotes a synergistic interaction between the inorganic and organic components. The V_2O_5-PPy film electrodes have higher specific capacities than the V_2O_5 electrode in Li batteries owing to the improved electronic conductivity and the

enhanced lithium-ion accessibility in the cathode. The conductive polymers in the V_2O_5-PPy film efficiently connect isolated V_2O_5 nanowires, resulting in the formation of conductive networks in the electrode. Bending the V_2O_5-PPy film electrodes to small radii of curvature has only a slight effect on the electrochemical behaviour in the bending test. The details of bending-state electrochemical testing of the free-standing electrode can provide useful information for further development of flexible and bendable batteries.

Chapter 7

Rapid synthesis of Free-Standing MoO_3/Graphene Films by The Microwave Hydrothermal Method as Cathode for Bendable Lithium Batteries

7.1 Introduction

The invention of rechargeable lithium ion batteries has actively changed the functionality of the modern life style [1], with such batteries attracting great interest as a promising energy source due to their advantages over traditional rechargeable systems, such as environmental friendliness, large energy density, and high output voltage. Many efforts have been made to meet the requirements for their application in electric vehicles and electronic devices [6]. Recently, there has been a strong interest in and high demand for ultra-thin, flexible, safe energy storage devices to meet the various design and power needs of modern electronic devices [252, 313]. To build such fully flexible and robust electrochemical devices, electrodes with specific electrochemical and mechanical properties need to be explored to fulfil these requirements. Traditional Li-storage material electrodes suffer from serious cracking and poor physical properties when they are frequently bent or loaded by impact bending, which is mainly due to weak bonding between the materials and the current collector. A thin free-standing electrode film with complete mechanical flexibility during operation could solve these problems. Nanostructured electrode materials, particularly one-dimensional (1D) nanowires/nanorods/nanobelts [67-

70], are considered to be the most promising avenue towards fabricating free-standing electrodes. The 1D nanowire, nanorod, or nanobelt morphology not only has a large electrode−electrolyte contact area and facile strain relaxation, but also efficient 1D electron transport pathways [67-68].

So far as free-standing cathode materials are concerned, there have been very few reports in the literature [200, 370-371]. Therefore, it is still a great challenge to explore an appropriate free-standing cathode material with high electrochemical performance for commercial application in bendable and wearable batteries. Among the known cathode materials for Li battery applications, molybdenum trioxide (MoO_3) is one of the most important energy storage candidates, with high discharge capacity around 300 mAh g^{-1} [188-192]. MoO_3 is also a promising material in gas sensors [193] and catalysts for selective partial oxidation in modern industry [194-195]. MoO_3 has three basic polymorphs, i.e., orthorhombic MoO_3, monoclinic MoO_3, and hexagonal MoO_3. As cathode for the Li battery, orthorhombic MoO_3 has been selected as a strong candidate due to its thermodynamically stable phase [190, 196]. The orthorhombic MoO_3 phase possesses a unique layered structure: each layer is composed of two sublayers, which are formed by corner-sharing [MoO_6] octahedra along the [001] and [100] directions, and the two sublayers are stacked together by sharing the edges of the octahedra along the [001] direction. The stacking of these layers along the [010] direction by the van der Waals interaction leads to the formation of MoO_3 with a two-dimensional structure, which allows guest atoms and ions (such as Li^+) to be introduced between the layers through intercalation [197]. In practical use for the Li battery, MoO_3 has poor ionic and electronic conductivity [198]. To improve the conductivity of MoO_3, carbon nanotubes [199-200], graphene

[76], or conducting polymer [201-202] could be the best choices of conductive fillers. Very recently, it was suggested that graphene, a new two-dimensional nanomaterial composed of sp^2-hybridized carbon, could be employed as an excellent candidate for the preparation of metal oxide − graphene nanocomposites due to its high conductivity, large surface area, flexibility, and chemical stability [372]. Metal oxide-graphene nanocomposites that have been prepared with different morphologies for specific applications include nanoparticle-graphene hybrids such as Fe_3O_4-graphene [373-375], NiO-graphene[376-377], SnO_2-graphene[378-380] and $LiFePO_4$-graphene[381-382] .

There are several reports on the hydrothermal synthesis of MoO_3 nanostructures to produce materials with high purity, homogeneity, good crystallinity, and unique properties [196, 383-385]. Microwave irradiation can be used as an alternative heat source for the hydrothermal process [386-387]. It leads to a rapid heating to attain the desired temperature in a short time and increases the reaction kinetics compared to the conventional hydrothermal method. In a microwave-assisted hydrothermal reaction, the heating rate is extremely rapid, due to the dielectric property of the medium or solvent [386-387]. Recently, Phuruangrat et al.[388] reported MoO_3 nanowires 50 nm in diameter and 10–12 μm in length that were synthesized by the microwave assisted hydrothermal method with cetyl trimethylammonium bromide (CTAB) as the surfactant-template.

Here, in this Chapter present a new method to synthesize high quality MoO_3 nanobelts from commercial bulk MoO_3 without a surfactant-template and combine them with graphene via a two-step microwave hydrothermal method for fabrication of highly flexible free-standing MoO_3/graphene films. The free-standing MoO_3

nanobelt/graphene films prepared by the above method followed by the vacuum filtration technique were investigated as a cathode material for bendable Lithium batteries and compared with MoO_3 nanobelt films prepared by a similar method but with no graphene.

7.2 Experimental

7.2.1 Preparation of MoO_3 nanobelt/graphene composite

The MoO_3 nanobelt/graphene composite was synthesized by a two-step microwave hydrothermal method. Graphene oxide (GO) was prepared from natural graphite powder (Fluka) by a modified Hummers' method with additional $KMnO_4$ [389]. In a typical synthesis, 20 mg of GO was dispersed in 100 mL deionized water and sonicated for 30 min to yield graphene oxide nanosheets. After sonication, 100 mg NaOH (Sigma–Aldrich) and $H_4N_2 \cdot H_2O$ (0.56 mL, Sigma–Aldrich) were added to the solution, followed by stirring for 10 min. After stirring, the mixture was transferred into a Teflon-lined microwave reactor (MicroSYNTH microwave system, Milestone), with the temperature controlled at 120 ^oC for 15 min. After cooling down to room temperature, the graphene product was filtered and washed with deionized water. 1 mmol MoO_3 powder (98%, Sigma-Aldrich) was dissolved in 20 ml deionized water, and 5 ml 30 % H_2O_2 (Sigma Aldrich) was then mixed in under vigorous magnetic stirring on a hot plate with the temperature set to 80 ^oC until a transparent yellow solution was obtained. Then, the graphene product was gently mixed with the MoO_3 solution for 10 min to yield a brown homogeneous suspension. The reaction solution was transferred to a 100 mL Teflon-lined autoclave and kept in a microwave oven (MicroSYNTH microwave system, Milestone) at 180 °C for 30

min. The power, time, and temperature of the reaction system were controlled by a Labterminal 800 Controller. After naturally cooling to room temperature, the product was washed several times with distilled water.

7.2.2 Preparation of free-standing MoO_3/graphene film

To make a uniform film, a modified vacuum filtration technique was adopted [271], where a 300 ml filter funnel (Glasco) was used. In a typical procedure, 2 mg/ml of MoO_3 /graphene material was dispersed into 50 ml of distilled water. Then, the as-prepared suspension was poured into the funnel and filtered through a porous polyvinylidene fluoride (PVDF) membrane (Millipore, 0.22 μm pore size, 47 mm in diameter) by positive pressure from a vacuum pump. Since the solvent passed through the pores of the membrane, the MoO_3/graphene material was trapped on the membrane surface, forming a mat. The resultant mat, together with the PVDF membrane, was then dried in an oven for 2 h, and the mat could finally be peeled off from the membrane.

7.2.3 Structure and morphology analysis

X-ray diffraction (XRD) data for phase analysis was obtained using a GBC MMA generator and diffractometer with Cu K_α radiation. Raman spectroscopy was conducted using a JOBIN YVON HR800 Confocal Raman system with 632.8 nm diode laser excitation on a 300 lines mm^{-1} grating at room temperature. This was performed in order to confirm the presence of graphene in the nanobelt products and to further investigate the MoO_3, and MoO_3/graphene films produced. The amount of graphene in the sample was estimated by thermogravimetric analysis (TGA) using a TGA/DSC 1 Star^e System. The morphologies of the films were investigated by field

emission scanning electron microscopy using a JEOL JSM-7500FA cold emission instrument. Transmission electron microscopy (TEM) and high resolution TEM was performed using JEOL 2011, 200 kV instrument. Samples for TEM were dispersed on Quantifoil holey carbon supports with analysis performed on regions over the holes.

7.2.4 Electrochemical measurements

To test the electrochemical performance of the MoO_3/graphene film as cathode, square model electrodes were cut off from the obtained free-standing film and then dried at 100 ^oC in a vacuum oven overnight. All electrochemical measurements were carried out by using CR 2032 coin-type cells (provided by DLG battery Co., Ltd, Shanghai, China). The coin-type cells were assembled in an Ar-filled glove box (Mbraun, Unilab, Germany) by stacking a porous polypropylene separator containing liquid electrolyte between the MoO_3/graphene film electrodes and the lithium foil counter electrode. The electrolyte used was 1 M $LiPF_6$ in a 50:50 (v/v) mixture of ethylene carbonate (EC) and dimethyl carbonate (DMC), provided by MERCK KgaA, Germany. Charge-discharge tests were carried out by using a battery testing device (Land Battery Tester) interfaced to a computer with software. The system is capable of switching between charge and discharge automatically, according to the pre-set cut-off potentials. The cells were cycled between 1.5 - 3.5 V with a constant current of 100 mA g^{-1}. Cyclic voltammetry (CV) was performed using a VMP3 Biologic electrochemistry workstation at a scan rate of 0.1 mV s^{-1}.

7.3 Results and discussion

MoO_3 nanobelts are synthesized by microwave hydrothermal treatment using hydrogen peroxide, which is found to be a rapid and facile method for the preparation of MoO_3 nanobelts. The X-ray diffraction (XRD) patterns of the samples are presented in Fig. 7.1(a).

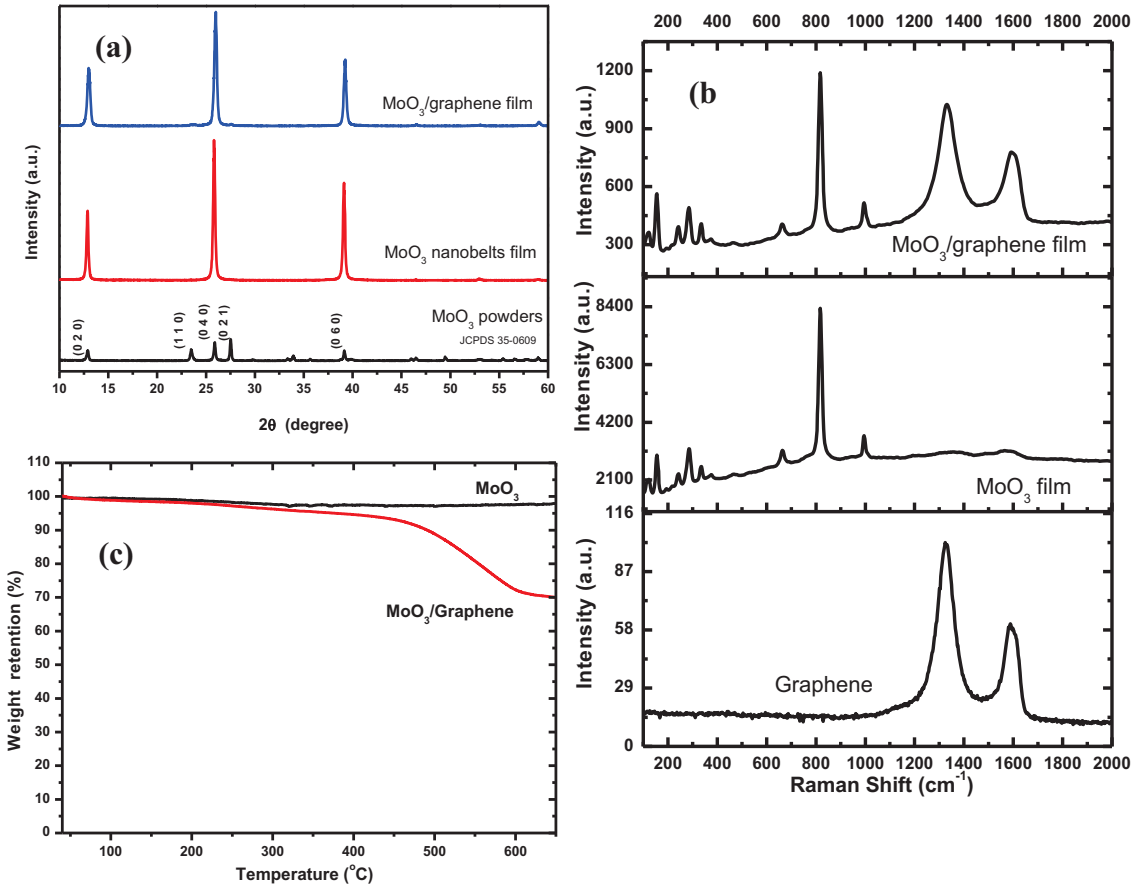

Figure 7.1 (a) XRD patterns of MoO_3 film, MoO_3/graphene film, and commercial MO_3 powders; (b) Raman spectra of MoO_3/graphene film, MoO_3, and graphene; (c) TGA curves of MoO_3 and MoO_3/graphene film.

All the diffraction peaks can be indexed as orthorhombic MoO_3 phase with the lattice parameters a = 3.96 Å, b = 13.86 Å, and c = 3.70 Å, in good agreement with the literature values (JCPDS card no. 35-0609). No characteristic peaks of impurities were detected in these patterns. The strong intensity of the (0 2 0), (0 4 0), and (0 6 0) diffraction peaks of the MoO_3 nanobelts indicate that there is a preferred orientation of the MoO_3 nanobelts [197, 390].The peak intensity of the pristine MoO_3 nanobelts is obviously stronger than that of the diffraction peaks for the powder samples. This can be mainly attributed to the morphology of the nanobelts, which is characterized by a strong crystallinity. The XRD patterns of the MoO_3/graphene hybrids show no evidence of diffraction peaks resulting from graphite oxide, indicating that the graphite oxide is reduced to graphene upon hydrothermal treatment. Due to the strong intensities of the diffraction peaks from the crystalline MoO_3 nanobelts, however, the characteristic broad diffraction peak with low intensity around 26°, corresponding to graphene, is not observed in the XRD pattern of the MoO_3/graphene composite.

Raman spectra of graphene, MoO_3, and MoO_3/graphene film are shown in Fig. 7.1(b). Two characteristic bands are observed in the Raman spectrum of graphene: the one centred at 1324 cm^{-1} (D band) is attributed to local defects/disorder, and the other at 1585 cm^{-1} (G band) can be assigned to the sp^2 graphitized structure [391], while the Raman spectrum of the MoO_3/graphene film reveals that the D and G bands appear at about 1328 and 1592 cm^{-1}, respectively. The Raman spectrum of the MoO_3/graphene film also shows three sharp characteristic bands of MoO_3. The Raman bands at 995 cm^{-1} and 817 cm^{-1} can be assigned to the asymmetrical and symmetrical stretching vibrations of the terminal

Mo=O bonds, while the band at 664 cm^{-1} is attributed to the asymmetrical stretching vibration of O–Mo–O bonds [392]. Peaks observed in the range of 100 – 400 cm^{-1} correspond to various bending modes of α-MoO_3 crystal.

For quantifying the amount of graphene in the MoO_3/graphene composite material, TGA is carried out in air (Fig. 7.1(c)). The samples are heated from 30 to 650 ^oC at a rate of 10 ^oC min^{-1}. No obvious mass loss is observed up to 650 °C for the as-prepared MoO_3, indicating that the bare MoO_3 remains stable over the entire temperature range. As the MoO_3 remains stable over this temperature range, any weight change is believed to correspond to the oxidation of graphene [393]. Therefore, the change in weight before and after the oxidation of graphene directly translates into the amount of graphene in the MoO_3/graphene film. By the use of this method, it is estimated that the amount of graphene is approximately 30 wt.%.

Field emission SEM (FESEM) observations of the MoO_3 nanobelts and the MoO_3/graphene film are presented in Fig. 7.2. The FESEM secondary electron image of the pristine MoO_3 nanobelt film (Fig. 7.2(a)) shows uniformly straight nanobelts ~200-800 nm in width and several micrometers in length. A side view of the MoO_3 film (Fig. 7.2(b)) indicates that the MoO_3 film is composed of a very densely packed layers, so that the thickness of the flexible electrode is around 50 μm. On the other hand, the MoO_3/graphene film (Fig.7. 2(c)) shows a similar morphology to that of the MoO_3, with the nanobelts lying on the stacked grapheme sheets. Photographs of as-prepared free-standing MoO_3/graphene films peeled off from PVDF membranes are shown in Fig. 7.2(d). The MoO_3/graphene paper is flexible, so that it can be bent to any curvature without breaking off and then returned to its original shape, while still maintaining its useful properties.

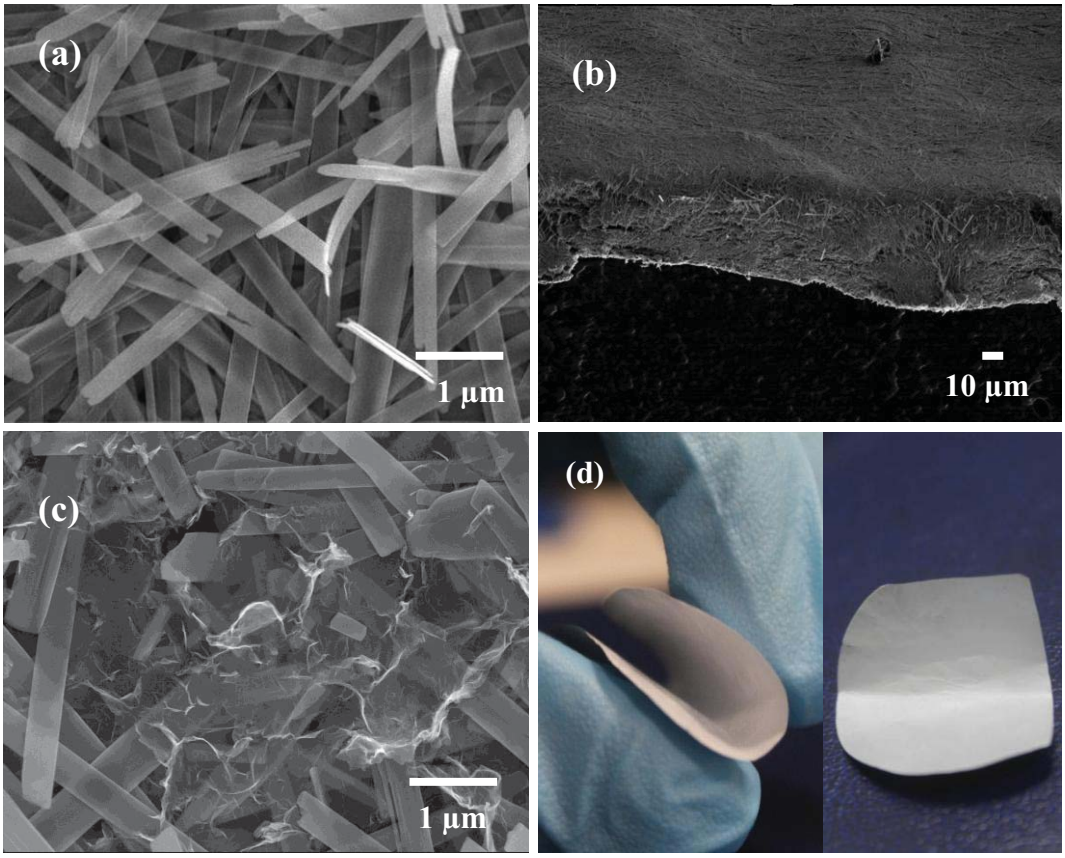

Figure 7.2 FESEM secondary electron and optical images: (a) top view of free-standing MoO_3 film, (b) and cross-sectional view at low magnification of free-standing MoO_3 film; (c) MoO_3/graphene film, and (d) Photographs demonstrating the flexibility of the MoO_3/graphene film.

TEM and HRTEM (Fig. 7.3) reveal further information about the morphology and structure of the MoO_3 /graphene films. Morphologies comprise either individual belts (Fig. 7.3(a)) or groups of thin belts lying on layers of graphene, as indicated in Fig. 7.3(b) and the associated high magnification inset.

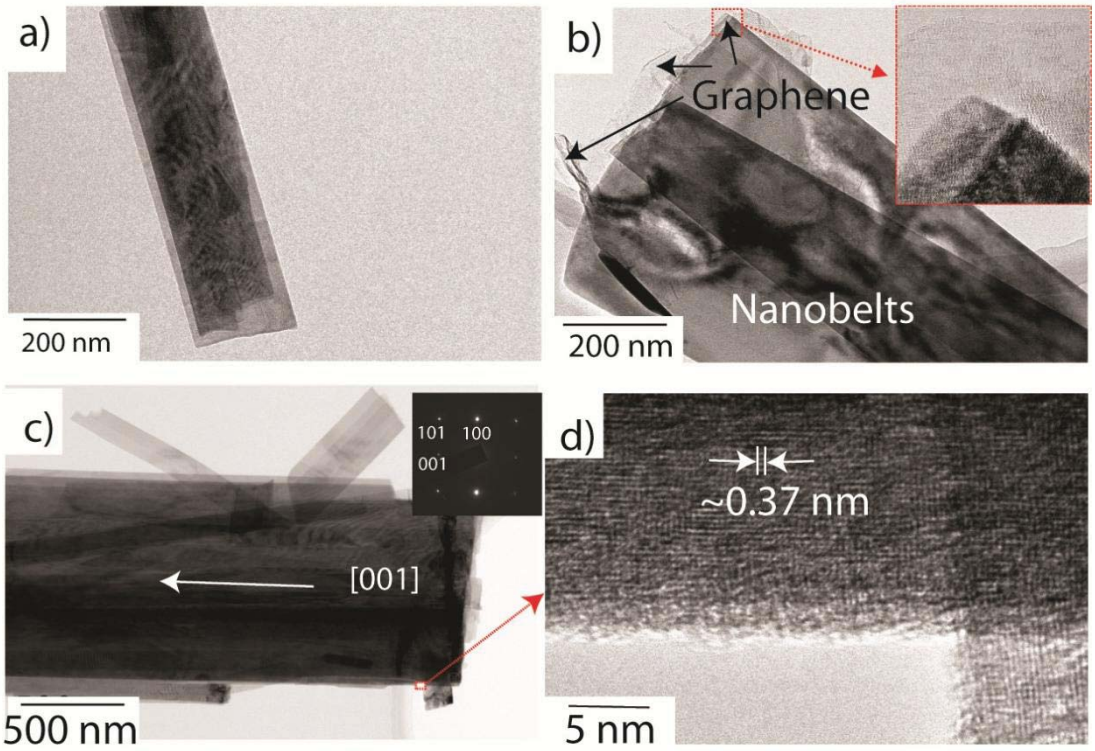

Figure 7.3 TEM and HRTEM images of MoO_3/graphene film: (a) low magnification image of of a single nanobelt, (b) MoO_3 nanobelts coated with graphene, as indicated by arrows and higher magnification inset image, (c) Bright field image of nanobelt and associated electron diffraction pattern (near [010] zone axis) indicating an [001] growth direction, and (d), HRTEM image of indicated region in (c) with 0.37 nm spacing consistent with (001)MoO_3.

Bright field imaging combined with selected area electron diffraction investigations (Fig. 7.3(c)) indicates that the MoO_3 growth direction is parallel to [001]. In this figure the zone axis is almost parallel to [010] MoO_3. High resolution imaging (Fig. 7.3(d)) of the area indicated in Fig. 7.3(c) also confirms the growth direction and

reveals a deformed MoO_3 lattice, structure typical of thin sheet materials and similar to that reveals in other HRTEM investigations of MoO_3 nanobelts [394].

The electrochemical behaviour of MoO_3 the nanobelts and MoO_3/graphene film is characterized by cyclic voltammograms (CV) at the scanning rate of 0.1 mV s^{-1} between 1.5 and 3.5 V, as shown in Fig. 7.4. The cathodic peaks located around 2.6 and 2.17 V are obtained from both samples during the negative scan from 3.5 to 1.5 V. These two reduction peaks correspond to two consecutive Li^+ intercalations into the film electrode. It is reported that the lithium ions can insert themselves not only into the interlayer spacing between the [MoO_6] octahedron layers but also into the [MoO_6] octahedron intralayers [395]. The cathodic peak at 2.6 V can be assigned to the irreversible lithium insertion into the crystal structure (probably into the [MoO_6] intralayers), which tends to trigger unrecoverable structural transformation of MoO_3 [395-396]. The anodic peak located at 2.53 V for both the MoO_3 film and the MoO_3/graphene film during the positive scan from 1.5 to 3.5 V corresponds to the reversible insertion of lithium ions into the interlayer spacings (van der Waals spacings) between the [MoO_6] octahedron layers [395]. The first anodic and cathodic peaks of the MoO_3 film are broader, while the MoO_3/graphene film exhibits sharper, more intense peaks. This strong hint indicates the good electrode kinetics of the MoO_3/graphene electrode.

The initial charge-discharge profiles for the MoO_3 and MoO_3/graphene composite electrodes at charge/discharge rates from 100 to 2000 mA g^{-1} are shown in Fig. 7.5(a–b).

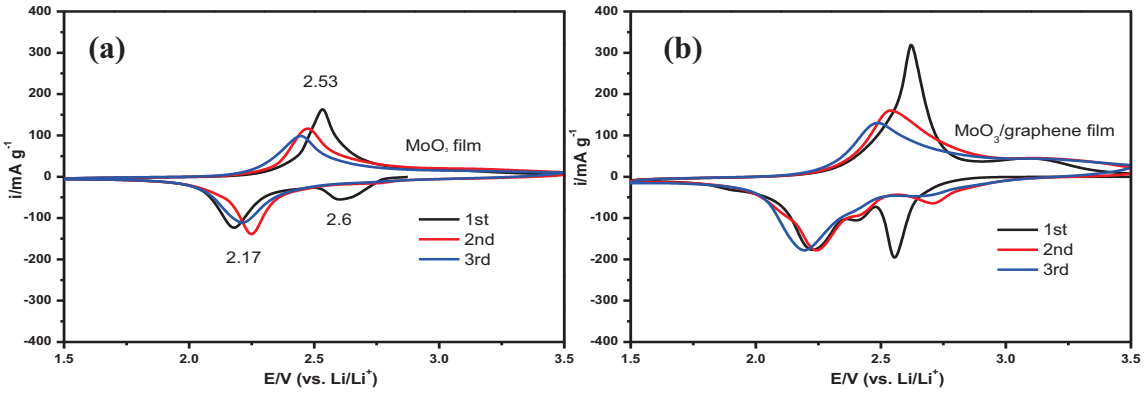

Figure 7.4 Typical CV profiles for the first 3 cycles of MoO_3 film (a) and MoO_3/graphene film (b) at scan rate of 0.1 mV s^{-1}.

For the MoO_3 and MoO_3/graphene samples, the discharge and the charge curves have two voltage plateaus due to Li^+ intercalation into the film electrode, which is consistent with the material prepared by hydrothermal treatment of a peroxomolybdic acid solution, as reported by Zhou et al. [197]. This also agrees with the results on cathodic and anodic peak potential in the cyclic voltammograms. Initial discharge capacities are measured to be 307 and 291 mAh g^{-1} at 100 mA g^{-1}, and 123 and 151 mAh g^{-1} at 2000 mA g^{-1} for the MoO_3 and MoO_3/graphene film electrodes, respectively. The discharge capacity decreases for all samples with increasing current density, and for the MoO_3 sample, the difference between the two plateaus becomes larger. The MoO_3 sample delivers sloping charge/discharge curves instead of a flat plateau (Fig. 7.5(a)) compared to the MoO_3/graphene sample (Fig. 7.5(b)), which still maintains a flat plateau in its charge/discharge curves even at the current density of 1000 mA g^{-1}. In addition, the MoO_3/graphene sample shows that the separation between the redox couple is small, and the CV curves for the second and third cycles

generally overlap, suggesting the good reversibility of lithium ion insertion/extraction in the van der Waals spacings of the MoO_3/graphene sample.

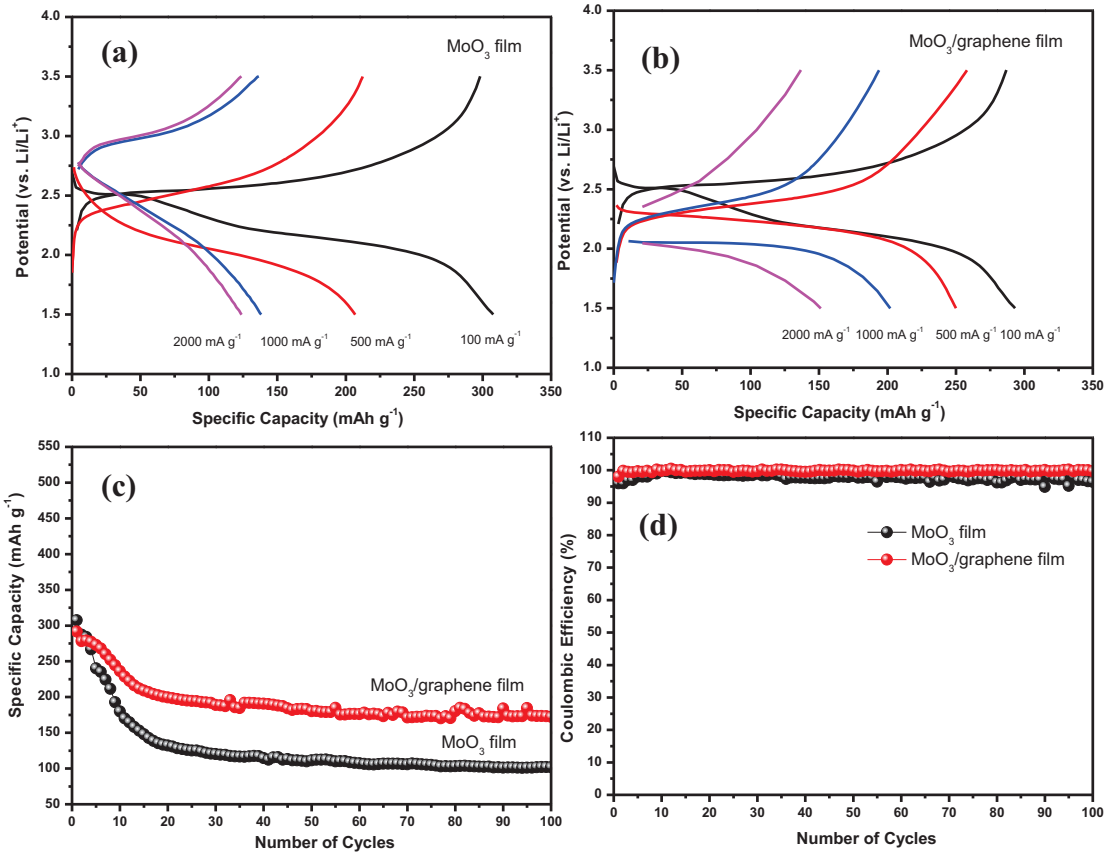

Figure 7.5 The initial galvanostatic charge-discharge profile of (a) MoO_3 film electrode, (b) MoO_3/graphene film electrode at different current densities from 100 to 2000 mA g^{-1} between 1.5 – 3.5 V; c) cycling performance beyond 100 cycles at 100 mA g^{-1}; d) coulombic efficiency.

The cycling performance of the MoO_3/graphene at 100 mA g^{-1} with that of the MoO_3 in the voltage range of 1.5–3.5 V is demonstrated in Fig. 7.5(c). The MoO_3/graphene electrode shows a higher capacity and better cycling performance. After 100 cycles, the discharge capacity for the MoO_3/graphene electrode is measured to be 172 mAh g^{-1} at 100 mA g^{-1} (59% of initial discharge capacity), with an initial coulombic efficiency of 98% (Fig. 7.5(d)). On the contrary, the discharge capacity for the MoO_3 electrode was only 101 mAh g^{-1} (32% of initial discharge capacity) at 100 mA g^{-1}, with an initial coulombic efficiency of 96%. The high capacity and good cycling performance delivered by the MoO_3/graphene electrode can be attributed to the graphene in the MoO_3/graphene film electrode, which evidently aids the Li^+ intercalation into the Li_xMoO_3 lattice of the MoO_3/graphene electrode, by improving both the accessibility for Li^+ ions and the electrical conductivity [202]. Graphene in the MoO_3/graphene film electrode can connect the isolated MoO_3 nanobelts and gives rise to valid conductive networks in the electrodes.

Electrochemical impedance spectroscopy (EIS) measurements are carried out in order to compare the conductivity of the prepared MoO_3 and MoO_3/graphene electrodes. To achieve stable solid electrolyte interphase (SEI) formation and the percolation of electrolyte through the electrode materials, the impedance measurements are performed after running charge-discharge for 5 cycles at a discharge potential of 2.5 V vs. Li/Li^+. The Nyquist plots of the two electrodes, as well as the fitting results using an equivalent circuit are depicted in Fig. 7.6(a). In this equivalent circuit (inset), R_Ω and R_{ct} are the ohmic resistance (total resistance of the electrolyte, separator, and electrical contacts) and charge-transfer resistance,

respectively. CPE is the constant phase-angle element, involving double layer capacitance, and W represents the Warburg impedance, reflecting the solid-state diffusion of Li ions into the bulk of the active materials, which is associated with the inclined line at low frequencies [397]. It can be seen clearly that the R_{ct} is much smaller for the MoO_3/graphene (R_{ct} = 216.5 Ω) electrode than for the MoO_3 (R_{ct} = 640.8 Ω) electrode after the 5th cycle, which indicates that the graphene coating could enable much easier charge transfer at the electrode/electrolyte interface and consequently, decrease the overall battery internal resistance. It seems that the electronic conductivity imparted by graphene to the MoO_3/graphene electrode material is much better than that of the electrode prepared by pressing a powder mixture with carbon black [197]. The graphene coating applied in the synthesis significantly enhances the conductivity of the MoO_3/graphene material, since the conductive graphene facilitates electronic conductive paths in the MoO_3 nanobelts, which is considered a key factor in improving the discharge capacity, rate capability, and cycle life of the MoO_3/graphene material. Besides the increased conductivity of the electrode due to graphene during charge and discharge cycling, the high performance of the MoO_3/graphene film is strongly related to the nanobelt morphology of the MoO_3 cathode material. MoO_3 nanobelts have a large surface area, which will reduce the actual effective current density on the active material and relieve the strain induced by the volume change during the electrochemical reaction. Moreover, due to the flexibility of the MoO_3 nanobelts, the morphology of the MoO_3 nanobelts can be preserved during the Li^+ insertion/extraction process, even after 100 cycles, as shown in Fig. 7.6(b).

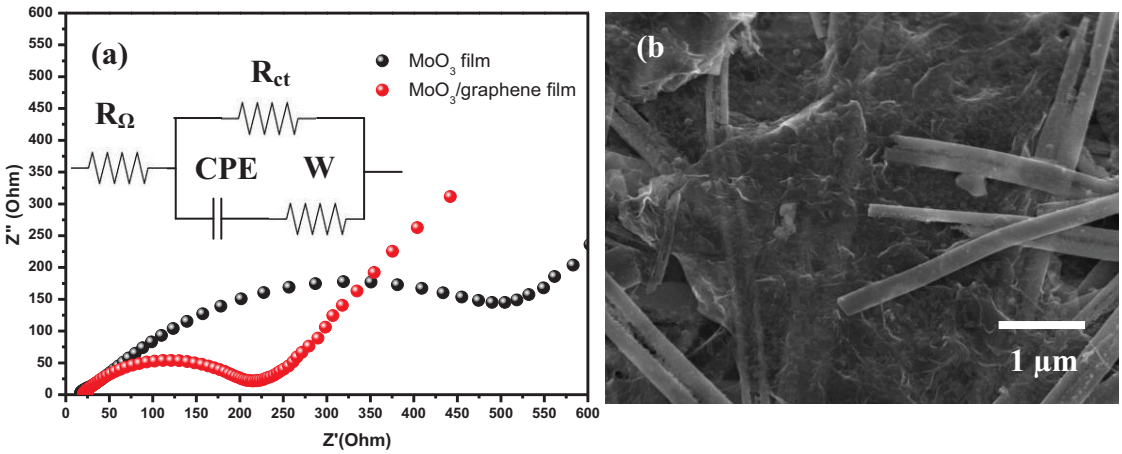

Figure 7.6 Nyquist plots for the MoO_3/graphene film electrode after running charge-discharge for 5 cycles at a discharge potential of 2.5 V vs. Li/Li^+ and fitting results using the equivalent circuit shown in the inset (a), and FESEM image of MoO_3/graphene film electrode after charge-discharge for 100 cycles (b).

7.4 Conclusions

In this Chapter, free-standing flexible MoO_3/graphene film electrode is prepared by a two-step, ultra-fast, microwave hydrothermal method and then followed by vacuum filtration technique. The hybrid material, consisting of a layer-structured metal oxide, MoO_3, and graphene results in a synergistic interaction between the inorganic and organic components. The charge-discharge measurements show that the MoO_3/graphene film delivers a significantly higher reversible capacity and excellent cycling stability (172 mAh g^{-1} at 100 mA g^{-1} after 100 cycles) compared to the pristine MoO_3 film. The results show that the MoO_3/graphene

designed in this Chapter can be used as a flexible cathode material for rechargeable bendable Li-ion batteries. The MoO_3/graphene film electrodes have higher specific capacities than the MoO_3 film electrode, since the conductive graphene facilitates electronic conductive paths in the MoO_3 nanobelts, and the good performance is also related to the nanobelt morphology of the MoO_3 cathode material.

Chapter 8

General Conclusions and Outlook

8.1 General Conclusions

All the results presented in this doctoral work are intended to broaden our knowledge in the field of advanced energy storage materials, especially self-supported nanostructures and composite film materials, their synthesis, fabrication, characterization, and application as electrode in flexible lithium-ion batteries. Synthesized nanostructures or composites for flexible electrode materials show several advantages. Nanostructured electrodes may not only introduce innovative reaction mechanisms, but also improve electrochemical properties, such as the specific energy storage capacity, accessibility of the electrolyte, and path lengths for both electronic and Li ion transport (permitting operation even with low electronic or low Li ion conductivity), enhancing the reactivity and cycling stability over the performance of their bulk counterparts. On the other hand, conductive composite materials not only have benefits in terms of decreasing the absolute volume changes and improving the mobility of the lithium ions, but also offer a conductive pathway along a whole interconnected wall in the structure, which is favourable for the transport of electrons to improve the high rate capability, promote liquid electrolyte diffusion into the bulk material, and act as a protective layer during the redox reaction. In term of free-standing electrode films, this type of electrode (not needing any current collector) has been demonstrated to be a very attractive candidate for

flexible, bendable, and binder-free electrode in the lithium-ion battery (LIB) system. This type of electrode will not only significantly improve the specific mass capacity of practical LIBs, but also lower the manufacturing costs. In addition, a conductive matrix such as carbon nanotubes and graphene film should be able to effectively accommodate huge volume changes, thereby significantly improving the cycling performance of high-capacity electrodes. In the following sections, a summary of the outcomes is given.

8.2 Anode Materials

The development of a flexible lithium battery in this thesis started with preparation of free-standing flexible anode materials. SnO_2-coated multiwall carbon nanotube **(**MWCNT) nanocomposites were synthesized by a facile hydrothermal method involving the use of hydrogen peroxide, but without any subsequent heat-treatment of precipitates at high temperatures, as first option for the flexible anode material. The FE-SEM images show that deposition of SnO_2 onto the surfaces of the MWCNTs takes place in some selected sites, while in the composite with higher content of SnO_2, more SnO_2 particles are deposited on these surfaces. In further development, free-standing SWCNT/SnO_2 anode paper was prepared by vacuum filtration of SWCNT/SnO_2 hybrid material, which was synthesized by the polyol method as the second alternative for a flexible anode material. In the SWCNT/SnO_2 paper, the CNTs form a 3D nanoporous network structure, with SnO_2 particles deposited onto the surface of the SWCNTs in selected sites. The SnO_2/MWCNT composites, when combined with carboxymethyl cellulose (CMC) as the binder, show excellent cyclic retention, with the high specific capacity of 473 mAh/g beyond 100 cycles, much greater than the free-standing SWCNT/SnO_2 paper which shows a

specific discharge capacity no greater than 454 mAh/g. The SnO_2/MWCNT composites, however, cannot be applied in the flexible lithium battery system due to the difficulty in inducing MWCNTs to form mats/thin films during the filtration process. SWCNTs behave totally differently from MWCNTs during film preparation by the filtration process. They can easily form a mat due to the high ratio of length to diameter. Moreover, SWCNTs, in the case of free-standing SWCNT/SnO_2 anode paper, have better mechanical properties than MWCNTs as matrix support. This is demonstrated by the bending tests of the SWCNT/SnO_2 electrodes to extremely small radii of curvature, which had a minimal effect upon the electrochemical behaviour. These results illustrate the robust nature of the SWCNTs in free-standing SWCNT/SnO_2 electrodes and their promise for flexible lithium batteries.

8.3 Cathode Materials

In addition to flexible anode material, flexible cathode materials also should be prepared to complete the all-flexible lithium battery system. In terms of candidate cathode materials for flexible lithium battery, highly flexible, free-standing V_2O_5-polypyrrole film electrode prepared by the vacuum filtration method was chosen as the first alternative for the flexible cathode material. The charge-discharge measurement results showed that free-standing V_2O_5-polypyrrole film electrode delivered a significantly higher reversible capacity, 187 mA h g^{-1} after 100 cycles, than the MoO_3/graphene film prepared by a two-step microwave hydrothermal method, which delivered a reversible capacity of 172 mAh g^{-1} under the same conditions. It is possible that the V_2O_5-polypyrrole hybrid material, consisting of a layer-structured metal oxide and a conducting polymer, promotes a synergistic interaction between the inorganic and organic components. Moreover, the

homogeneity of the PPy coating over the entire surface of V_2O_5 nanowires is believed to enhance the electronic conductivity of the electrode material through its effects on the electronic transfer paths during the charge-discharge process. Although free-standing V_2O_5-polypyrrole film electrode has better specific discharge capacity than the free-standing flexible MoO_3/graphene film electrode, the surface coating of V_2O_5 nanowires by PPy that is uniformly deposited throughout entire lengths of nanowires in irregular or spherical forms will greatly affect the strength of the electrode materials.

Based on the work presented in this thesis, SnO_2, V_2O_5, and MoO_3 have the potential to improve the electrochemical performance of flexible lithium batteries, in term of both high specific capacity and flexibility. In addition, for future development of flexible batteries, there could be promising results obtained from a flexible cell consisting of SWCNT/SnO_2 anode and V_2O_5/PPy cathode.

8.4 Outlook

All topics discussed in this thesis can be further extended in every aspect, because every new finding opens the door to additional scientific questions and technical improvements. The collected recommendations here should be considered as starting ideas for future development of the flexible lithium-ion battery system. In this thesis, the experimental work was mainly focused on the synthesis of self-supported nanostructured and composite materials and their application as electrode materials for use in flexible lithium-ion batteries. The synthesis methods presented here are also applicable to the preparation of other metal oxide nanostructured materials or composite materials.

The work on SnO_2-coated carbon nanotubes, both multi-wall carbon nanotubes and single-wall carbon nanotubes, needs to be further extended to other anode materials, such as silicon, tin, and Fe_2O_3, for improving their capacity and high rate capability. Pre-treatment of commercial carbon nanotubes in acid solution should be carried out to ensure that there are no impurities during experiments. The hydrothermal method is proven to be suitable for synthesizing nanostructured materials in various forms, while the polyol method produces only nanoparticles. Nevertheless, the polyol method is easy to perform and can be scaled up accordingly. Beside oxides, a variety of materials, including sulfides, phosphates, and elemental metals, can be produced under very similar experimental conditions.

The cycling stability of free-standing V_2O_5-PPy film electrode can be further improved via doping with other anions in the system. The influence of different dopants on the PPy could enhance the performance stability and rate capability of film electrode because the electrochemical properties of such polymers depend on the size and mobility of anion dopants.

Microwave irradiation has successfully been used in the synthesis of MoO_3 nanobelts via the hydrothermal method. Microwave-assisted synthesis methods have been proved to be particularly effective, as they can yield the product rapidly with controlled particle size and morphology. In the case of MoO_3 nanobelts, poor capacity retention in initial cycles could be avoided by reducing the widths of the nanobelts and completely coating them with graphene. Coating with other conductive materials such as conductive polymers could be another alternative to improve the overall and local electrical conductivity of the electrode, leading to improved electrochemical performance.

In the case of the design of flexible lithium ion batteries, the evolution of the lithium-ion battery from rigid structures to flexible forms has many potential advantages where flexible Li batteries could provide shape flexibility. In this technology, flexible electrode materials and gel polymer as electrolyte and separator would be key factors in this type of battery. For polyvinylidene fluoride (PVDF)-based gel polymer electrolytes, attention needs to be focused on fully understanding the interfacial reaction between the working electrode and lithium metal as the source of lithium-ions. Several factors in the fabrication of flexible cells, in particular the contact surfaces for all the components, have to be improved by using appropriate tools and equipment.

The disadvantages of nanomaterials due to their high surface area also need to be taken into account. The nanomaterials typically show low density and high reactivity in terms of side reactions, resulting in more irreversible capacity and causing safety issues associated with the size effect. In order to reduce the disadvantages of nanomaterials, surface modification and selection of the correct size of the particles need to be further investigated. In situ characterization tools are other possible ways to move forward to drive further breakthroughs in lithium-ion battery performance. Nevertheless, the author believes that the scientific challenges are being slowly overcome and that research is moving in the right direction with a well-defined goal, as proven in this thesis, so that the future for the next generations of flexible Li-ion batteries is likely to be brighter ahead.

References

[1] D. Liu, G. Cao, Energy & Environmental Science, 3 (2010) 1218-1237.

[2] D.A. Notter, M. Gauch, R. Widmer, P. Wäger, A. Stamp, R. Zah, H.-J.r. Althaus, Environmental Science & Technology, 44 (2010) 6550-6556.

[3] J. Read, Journal of The Electrochemical Society, 149 (2002) A1190-A1195.

[4] P.G. Bruce, S.A. Freunberger, L.J. Hardwick, J.M. Tarascon, Nature Materials, 11 (2012) 19-29.

[5] D. Capsoni, M. Bini, S. Ferrari, E. Quartarone, P. Mustarelli, Journal of Power Sources, 220 (2012) 253-263.

[6] H. Nishide, K. Oyaizu, Science, 319 (2008) 737-738.

[7] A.S. Arico, P. Bruce, B. Scrosati, J.-M. Tarascon, W. van Schalkwijk, Nat Mater, 4 (2005) 366-377.

[8] S.S. Zhang, Journal of Power Sources, 164 (2007) 351-364.

[9] J.Y. Song, Y.Y. Wang, C.C. Wan, Journal of Power Sources, 77 (1999) 183-197.

[10] S.B. Brummer, V.R. Koch, Materials for Advanced Batteries, Plenum, New York, 1980.

[11] M.B. Armand, J.M. Chabagno, M. Duclot, Fast Ion Transport in Solids, Elsevier, Amsterdam, 1979.

[12] S. Megahed, B. Scrosati, Interface, 4 (1995) 34.

[13] P. Discussion, J. Power Sources, 68 (1997) 173.

[14] K. Murata, Electrochimica Acta, 40 (1995) 2177-2184.

[15] G.P. Bierwagen, Electrochimica Acta, 37 (1992) 1471-1478.

[16] M. Winter, R.J. Brodd, Chemical Reviews, 104 (2004) 4245-4270.

[17] G.-y. Adachi, N. Imanaka, H. Aono, Advanced Materials, 8 (1996) 127-135.

[18] A. Oberlin, M. Endo, T. Koyama, Journal of Crystal Growth, 32 (1976) 335-349.

[19] S. Iijima, Nature, 354 (1991) 56-58.

[20] G. Che, B.B. Lakshmi, E.R. Fisher, C.R. Martin, Nature, 393 (1998) 346-349.

[21] E. Frackowiak, F. Béguin, Carbon, 40 (2002) 1775-1787.

[22] G.T. Wu, C.S. Wang, X.B. Zhang, H.S. Yang, Z.F. Qi, P.M. He, W.Z. Li, Journal of The Electrochemical Society, 146 (1999) 1696-1701.

[23] M. Endo, Y.A. Kim, Y. Fukai, T. Hayashi, M. Terrones, H. Terrones, M.S. Dresselhaus, Applied Physics Letters, 79 (2001) 1531-1533.

[24] W. Zheng, Y.W. Liu, X.G. Hu, C.F. Zhang, Electrochimica Acta, 51 (2006) 1330-1335.

[25] N. Du, H. Zhang, B.D. Chen, J.B. Wu, X.Y. Ma, Z.H. Liu, Y.Q. Zhang, D.R. Yang, X.H. Huang, J.P. Tu, Advanced Materials, 19 (2007) 4505-4509.

[26] Z. Wen, Q. Wang, Q. Zhang, J. Li, Advanced Functional Materials, 17 (2007) 2772-2778.

[27] M.-S. Park, S.A. Needham, G.-X. Wang, Y.-M. Kang, J.-S. Park, S.-X. Dou, H.-K. Liu, Chemistry of Materials, 19 (2007) 2406-2410.

[28] J. Zhao, A. Buldum, J. Han, J. Ping Lu, Physical Review Letters, 85 (2000) 1706-1709.

[29] V. Meunier, J. Kephart, C. Roland, J. Bernholc, Physical Review Letters, 88 (2002) 075506.

[30] W. Lu, D.D.L. Chung, Carbon, 39 (2001) 493-496.

[31] S.-H. Yoon, C.-W. Park, H. Yang, Y. Korai, I. Mochida, R.T.K. Baker, N.M. Rodriguez, Carbon, 42 (2004) 21-32.

[32] K. Lin, Y. Xu, G. He, X. Wang, Materials Chemistry and Physics, 99 (2006) 190-196.

[33] Y.A. Kim, M. Kojima, H. Muramatsu, S. Umemoto, T. Watanabe, K. Yoshida, K. Sato, T. Ikeda, T. Hayashi, M. Endo, M. Terrones, M.S. Dresselhaus, Small, 2 (2006) 667-676.

[34] A.S. Claye, J.E. Fischer, C.B. Huffman, A.G. Rinzler, R.E. Smalley, Journal of The Electrochemical Society, 147 (2000) 2845-2852.

[35] S.Y. Chew, S.H. Ng, J. Wang, P. Novák, F. Krumeich, S.L. Chou, J. Chen, H.K. Liu, Carbon, 47 (2009) 2976-2983.

[36] S. Megahed, B. Scrosati, Journal of Power Sources, 51 (1994) 79-104.

[37] B. Scrosati, Electrochimica Acta, 45 (2000) 2461-2466.

[38] M. Winter, J.O. Besenhard, M.E. Spahr, P. Novák, Advanced Materials, 10 (1998) 725-763.

[39] S.-J. Lee, J.-K. Lee, S.-H. Chung, H.-Y. Lee, S.-M. Lee, H.-K. Baik, Journal of Power Sources, 97–98 (2001) 191-193.

[40] Z. Li, D. Zhang, F. Yang, Journal of Materials Science, 44 (2009) 2435-2443.

[41] M.S. Whittingham, Journal of The Electrochemical Society, 123 (1976) 315-320.

[42] C.R. Walk, N. Margalit, Journal of Power Sources, 68 (1997) 723-725.

[43] A. Pan, J.-G. Zhang, Z. Nie, G. Cao, B.W. Arey, G. Li, S.-q. Liang, J. Liu, Journal of Materials Chemistry, 20 (2010) 9193-9199.

[44] C. Wu, Y. Xie, Energy & Environmental Science, 3 (2010) 1191-1206.

[45] F.W. Dampier, Journal of The Electrochemical Society, 121 (1974) 656-668.

[46] P.A. Christian, J.N. Carides, F.J. DiSalvo, J.V. Waszczak, Journal of The Electrochemical Society, 127 (1980) 2315-2319.

[47] L.A. Riley, S.-H. Lee, L. Gedvilias, A.C. Dillon, Journal of Power Sources, 195 (2010) 588-592.

[48] I. Juárez Ramírez, A. Martínez-De La Cruz, Journal of Solid State Electrochemistry, 7 (2003) 259-263.

[49] N. Kumagai, N. Tanno, the journal of electrchemical society, 134 (1987) 406C.

[50] Y.-S. Kim, H.-J. Ahn, H.-S. Shim, T.-Y. Seong, Solid State Ionics, 177 (2006) 1323-1326.

[51] G. Amatucci, J.-M. Tarascon, Journal of The Electrochemical Society, 149 (2002) K31-K46.

[52] D. Belov, M.-H. Yang, Solid State Ionics, 179 (2008) 1816-1821.

[53] D. Belov, M.-H. Yang, Journal of Solid State Electrochemistry, 12 (2008) 885-894.

[54] C.-H. Doh, D.-H. Kim, H.-S. Kim, H.-M. Shin, Y.-D. Jeong, S.-I. Moon, B.-S. Jin, S.W. Eom, H.-S. Kim, K.-W. Kim, D.-H. Oh, A. Veluchamy, Journal of Power Sources, 175 (2008) 881-885.

[55] I. Nakai, T. Nakagome, Electrochemical and Solid-State Letters, 1 (1998) 259-261.

[56] A. Hirano, R. Kanno, Y. Kawamoto, Y. Takeda, K. Yamaura, M. Takano, K. Ohyama, M. Ohashi, Y. Yamaguchi, Solid State Ionics, 78 (1995) 123-131.

[57] M.M. Thackeray, Y. Shao-Horn, A.J. Kahaian, K.D. Kepler, E. Skinner, J.T. Vaughey, S.A. Hackney, Electrochemical and Solid-State Letters, 1 (1998) 7-9.

[58] H. Huang, C.A. Vincent, P.G. Bruce, Journal of The Electrochemical Society, 146 (1999) 3649-3654.

[59] Y. Shin, A. Manthiram, Electrochemical and Solid-State Letters, 5 (2002) A55-A58.

[60] H. Huang, S.-C. Yin, L.F. Nazar, Electrochemical and Solid-State Letters, 4 (2001) A170-A172.

[61] J.M. Tarascon, M. Armand, Nature, 414 (2001) 359-367.

[62] J.B. Goodenough, Y. Kim, Chemistry of Materials, 22 (2009) 587-603.

[63] B. Garcia, S. Lavallée, G. Perron, C. Michot, M. Armand, Electrochimica Acta, 49 (2004) 4583-4588.

[64] Y. Wang, K. Zaghib, A. Guerfi, F.F.C. Bazito, R.M. Torresi, J.R. Dahn, Electrochimica Acta, 52 (2007) 6346-6352.

[65] E. Markevich, V. Baranchugov, D. Aurbach, Electrochemistry Communications, 8 (2006) 1331-1334.

[66] F.B. Dias, L. Plomp, J.B.J. Veldhuis, Journal of Power Sources, 88 (2000) 169-191.

[67] E. Hosono, T. Kudo, I. Honma, H. Matsuda, H. Zhou, Nano Letters, 9 (2009) 1045-1051.

[68] D.K. Kim, P. Muralidharan, H.-W. Lee, R. Ruffo, Y. Yang, C.K. Chan, H. Peng, R.A. Huggins, Y. Cui, Nano Letters, 8 (2008) 3948-3952.

[69] Y. Yang, C. Xie, R. Ruffo, H. Peng, D.K. Kim, Y. Cui, Nano Letters, 9 (2009) 4109-4114.

[70] C.K. Chan, H. Peng, R.D. Twesten, K. Jarausch, X.F. Zhang, Y. Cui, Nano Letters, 7 (2007) 490-495.

[71] L. Noerochim, J.-Z. Wang, D. Wexler, M.M. Rahman, J. Chen, H.-K. Liu, Journal of Materials Chemistry, 22 (2012) 11159-11165.

[72] L. Noerochim, J.-Z. Wang, S.-L. Chou, D. Wexler, H.-K. Liu, Carbon, (2012).

[73] J.-Z. Wang, S.-L. Chou, J. Chen, S.-Y. Chew, G.-X. Wang, K. Konstantinov, J. Wu, S.-X. Dou, H.K. Liu, Electrochem Comm, 10 (2008) 1781-1784.

[74] L. Noerochim, J.-Z. Wang, S.-L. Chou, D. Wexler, H.-K. Liu, Carbon, 50 (2012) 1289-1297.

[75] V.L. Pushparaj, M.M. Shaijumon, A. Kumar, S. Murugesan, L. Ci, R. Vajtai, R.J. Linhardt, O. Nalamasu, P.M. Ajayan, Proceedings of the National Academy of Sciences, 104 (2007) 13574-13577.

[76] H. Gwon, H.-S. Kim, K.U. Lee, D.-H. Seo, Y.C. Park, Y.-S. Lee, B.T. Ahn, K. Kang, Energy & Environmental Science, 4 (2011) 1277-1283.

[77] S.-L. Chou, Y. Zhao, J.-Z. Wang, Z.-X. Chen, H.-K. Liu, S.-X. Dou, The Journal of Physical Chemistry C, 114 (2010) 15862-15867.

[78] D. Ilic, P. Birke, K. Holl, T. Wöhrle, P. Haug, F. Birke-Salam, Journal of Power Sources, 129 (2004) 34-37.

[79] G.Z. Cao, Nanostructures and Nanomaterials, Synthesis, properties and applications, Imperial college press, London, 2004.

[80] P.G. Bruce, Solid State Ionics, 179 (2008) 752-760.

[81] G. Centi, S. Perathoner, Catalysis Today, 150 (2010) 151-162.

[82] C.-M. Park, Y.-U. Kim, H. Kim, H.-J. Sohn, Journal of Power Sources, 158 (2006) 1451-1455.

[83] S. Yoon, A. Manthiram, Chemistry of Materials, 21 (2009) 3898-3904.

[84] H.-Y. Lee, S.-M. Lee, Electrochemistry Communications, 6 (2004) 465-469.

[85] M.-S. Park, S. Rajendran, Y.-M. Kang, K.-S. Han, Y.-S. Han, J.-Y. Lee, Journal of Power Sources, 158 (2006) 650-653.

[86] J. Saint, M. Morcrette, D. Larcher, L. Laffont, S. Beattie, J.P. Pérès, D. Talaga, M. Couzi, J.M. Tarascon, Advanced Functional Materials, 17 (2007) 1765-1774.

[87] H. Kim, J. Cho, Journal of Materials Chemistry, 18 (2008) 771-775.

[88] X.W. Lou, Y. Wang, C. Yuan, J.Y. Lee, L.A. Archer, Advanced Materials, 18 (2006) 2325-2329.

[89] Y. Wang, G. Cao, Chemistry of Materials, 18 (2006) 2787-2804.

[90] H. Zhao, C. Jiang, X. He, J. Ren, C. Wan, Journal of Membrane Science, 310 (2008) 1-6.

[91] B. Scrosati, Solid state electrochemistry, Cambridge University Press, London, UK, 1995.

[92] P. Novák, K. Müller, K.S.V. Santhanam, O. Haas, Chemical Reviews, 97 (1997) 207-282.

[93] M. Armand, J.M. Tarascon, Nature, 451 (2008) 652-657.

[94] P. Van den Bossche, F. Vergels, J. Van Mierlo, J. Matheys, W. Van Autenboer, Journal of Power Sources, 162 (2006) 913-919.

[95] A.L. Robinson, Science, 184 (1974) 554-555.

[96] M.S. Whittingham, Science, 192 (1976) 1126-1127.

[97] M.S. Whittingham, U.S. Patent 4009052 and U.K. Patent 1468416, (1973).

[98] G.L. Holleck, J.R. Driscoll, Electrochimica Acta, 22 (1977) 647-655.

[99] A. Patil, V. Patil, D. Wook Shin, J.W. Choi, D.S. Paik, S.J. Yoon, Materials Research Bulletin, 43 (2008) 1913-1942.

[100] F.W. Dampier, Journal of The Electrochemical Society, 121 (1974) 656-660.

[101] P.G. Dickens, S.J. French, A.T. Hight, M.F. Pye, Materials Research Bulletin, 14 (1979) 1295-1299.

[102] C. Delmas, H. Cognac-Auradou, J.M. Cocciantelli, M. Ménétrier, J.P. Doumerc, Solid State Ionics, 69 (1994) 257-264.

[103] K. Mizushima, P.C. Jones, P.J. Wiseman, J.B. Goodenough, Materials Research Bulletin, 15 (1980) 783-789.

[104] M.M. Thackeray, W.I.F. David, P.G. Bruce, J.B. Goodenough, Materials Research Bulletin, 18 (1983) 461-472.

[105] J.O. Besenhard, Carbon, 14 (1976) 111-115.

[106] R. Yazami, P. Touzain, Journal of Power Sources, 9 (1983) 365-371.

[107] A. Kasei, US. Patent, 4668595, (1987).

[108] T. Nagaura, K. Tozawa, Progress in batteries and solar cells, 9 (1990) 209.

[109] C.-H. Doh, D.-H. Kim, J.-H. Lee, D.-J. Lee, B.-S. Jin, H.-S. Kim, S.-I. Moon, Y. Hwang, A. Veluchamy, Bull. Korean Chem. Soc., 30 (2009) 783-786.

[110] D. Lisbona, T. Snee, Process Safety and Environmental Protection, 89 (2011) 434-442.

[111] P.G. Balakrishnan, R. Ramesh, T. Prem Kumar, Journal of Power Sources, 155 (2006) 401-414.

[112] M. Armand, J.M. Chabagno, M.J. Duclot, fast ion transport in solids electrodes and electrolyte, North -Holland, Amsterdam, 1979.

[113] M.B. Armand, Journal of Power Sources, 14 (1985) 11-12.

[114] J.M. Tarascon, A.S. Gozdz, C. Schmutz, F. Shokoohi, P.C. Warren, Solid State Ionics, 86–88, Part 1 (1996) 49-54.

[115] R. Liu, J. Duay, S.B. Lee, Chemical Communications, 47 (2011) 1384-1404.

[116] Y. Nishi, Journal of Power Sources, 100 (2001) 101-106.

[117] M. Wakihara, Materials Science and Engineering: R: Reports, 33 (2001) 109-134.

[118] E. Peled, J. Electrochem. Soc., 126 (1979) 207.

[119] D. Aurbach, M.D. Levi, E. Levi, A. Schechter, J. Phys. Chem. B, 101 (1997) 2195.

[120] S.H. Kang, D.P. Abraham, A. Xiao, B.L. Lucht, J. Power Sources, 175 (2008) 526.

[121] J.O. Besenhard, M. Winter, J. Yang, W. Biberacher, J. Power Sources, 54 (1995) 228.

[122] H. Bryngelsson, M. Stjerndahl, T. Gustafsson, K. Edström, J. Power Sources, 174 (2007) 970.

[123] K. Edström, M. Herstedt, D.P. Abraham, J. Power Sources, 153 (2006) 380.

[124] Y. Ein-Eli, B. Markovsky, D. Aurbach, Y. Carmeli, H. Yamin, S. Luski, Electrochim. Acta, 39 (1994) 2559.

[125] C. Liebenow, M.W. Wagner, K. Lühder, P. Lobitz, J.O. Besenhard, J. Power Sources, 54 (1995) 369.

[126] D. Aurbach, J. Power Sources, 89 (2000) 206.

[127] T. Yoshida, M. Takahashi, S. Morikawa, C. Ihara, H. Katsukawa, T. Shiratsuchi, J. Yamaki, J. Electrochem. Soc., 153 (2006) A576.

[128] D. Alliata, R. Kotz, P. Novak, H. Siegenthaler, Electrochem. Commun., 2 (2000) 436.

[129] A. Zaban, D. Aurbach, J. Power Sources, 54 (1995) 289.

[130] E. Peled, D. Golodnitsky, G. Ardel, J. Electrochem. Soc., 144 (1997) L208.

[131] A.M. Andersson, K. Edstrom, J. Electrochem. Soc., 148 (2001) A1100.

[132] K. Zaghib, G. Nadeau, K. Kinoshita, J. Electrochem. Soc., 147 (2000) 2110.

[133] R. Yazami, Y.F. Reynier, Electrochim. Acta, 47 (2002) 1217.

[134] P. Novák, J.C. Panitz, F. Joho, M. Lanz, R. Imhof, M. Coluccia, J. Power Sources, 90 (2000) 52.

[135] A.V. Churikov, Electrochim. Acta, 46 (2001) 2415.

[136] G. Park, H. Nakamura, Y. Lee, M. Yoshio, J. Power Sources, 189 (2009) 602.

[137] D. Aurbach, E. Zinigrad, Y. Cohen, H. Teller, Solid State Ionics, 148 (2002) 405.

[138] H. Zabel, S.A. Solin, Springer-Verlag, New York, (1992).

[139] J. Yamaura, Y. Ozaki, A. Morita, A. Ohta, Journal of Power Sources, 43 (1993) 233-239.

[140] R. Fong, U.v. Sacken, J.R. Dahn, Journal of The Electrochemical Society, 137 (1990) 2009-2013.

[141] D. Aurbach, Y. Ein-Eli, B. Markovsky, A. Zaban, S. Luski, Y. Carmeli, H. Yamin, Journal of The Electrochemical Society, 142 (1995) 2882-2890.

[142] H. Azuma, H. Imoto, S.i. Yamada, K. Sekai, Journal of Power Sources, 81–82 (1999) 1-7.

[143] J.R. Dahn, A.K. Sleigh, H. Shi, J.N. Reimers, Q. Zhong, B.M. Way, Electrochimica Acta, 38 (1993) 1179-1191.

[144] F. Béguin, F. Chevallier, C. Vix-Guterl, S. Saadallah, V. Bertagna, J.N. Rouzaud, E. Frackowiak, Carbon, 43 (2005) 2160-2167.

[145] K. Sato, M. Noguchi, A. Demachi, N. Oki, M. Endo, Science, 264 (1994) 556-558.

[146] H.-Q. Xiang, S.-B. Fang, Y.-Y. Jiang, Journal of The Electrochemical Society, 144 (1997) L187-L190.

[147] A. Mabuchi, K. Tokumitsu, H. Fujimoto, T. Kasuh, Journal of The Electrochemical Society, 142 (1995) 1041-1046.

[148] M.S. Mauter, M. Elimelech, Environmental Science & Technology, 42 (2008) 5843-5859.

[149] E.H.L. Falcao, F. Wudl, Journal of Chemical Technology & Biotechnology, 82 (2007) 524-531.

[150] M. Dresselhaus, M. Endo, Relation of Carbon Nanotubes to Other Carbon Materials

Carbon Nanotubes, in: M. Dresselhaus, G. Dresselhaus, P. Avouris (Eds.), Springer Berlin / Heidelberg, 2001, pp. 11-28.

[151] K.S. Novoselov, A.K. Geim, S.V. Morozov, D. Jiang, Y. Zhang, S.V. Dubonos, I.V. Grigorieva, A.A. Firsov, Science, 306 (2004) 666-669.

[152] Y. Zhang, Y.-W. Tan, H.L. Stormer, P. Kim, Nature, 438 (2005) 201-204.

[153] J.R. Dahn, T. Zheng, Y. Liu, J.S. Xue, Science, 270 (1995) 590-593.

[154] Y. Liu, J.S. Xue, T. Zheng, J.R. Dahn, Carbon, 34 (1996) 193-200.

[155] A.N. Dey, Journal of The Electrochemical Society, 118 (1971) 1547-1549.

[156] J.O. Besenhard, J. Yang, M. Winter, Journal of Power Sources, 68 (1997) 87-90.

[157] W.J. Weydanz, M. Wohlfahrt-Mehrens, R.A. Huggins, Journal of Power Sources, 81–82 (1999) 237-242.

[158] M.N. Obrovac, L. Christensen, Electrochemical and Solid-State Letters, 7 (2004) A93-A96.

[159] J. Wolfenstine, Journal of Power Sources, 79 (1999) 111-113.

[160] C.K. Chan, H. Peng, G. Liu, K. McIlwrath, X.F. Zhang, R.A. Huggins, Y. Cui, Nat Nano, 3 (2008) 31-35.

[161] H. Ma, F. Cheng, J.Y. Chen, J.Z. Zhao, C.S. Li, Z.L. Tao, J. Liang, Advanced Materials, 19 (2007) 4067-4070.

[162] S. Cahen, R. Janot, L. Laffont-Dantras, J.M. Tarascon, Journal of The Electrochemical Society, 155 (2008) A512-A519.

[163] S.-H. Ng, J. Wang, D. Wexler, K. Konstantinov, Z.-P. Guo, H.-K. Liu, Angewandte Chemie International Edition, 45 (2006) 6896-6899.

[164] J. Yang, M. Winter, J.O. Besenhard, Solid State Ionics, 90 (1996) 281-287.

[165] M. Wachtler, J.O. Besenhard, M. Winter, Journal of Power Sources, 94 (2001) 189-193.

[166] H. Li, L. Shi, Q. Wang, L. Chen, X. Huang, Solid State Ionics, 148 (2002) 247-258.

[167] H. Zhao, D.H.L. Ng, Z. Lu, N. Ma, Journal of Alloys and Compounds, 395 (2005) 192-200.

[168] X.-Z. Liao, Z.-F. Ma, J.-H. Hu, Y.-Z. Sun, X. Yuan, Electrochemistry Communications, 5 (2003) 657-661.

[169] Q.F. Dong, C.Z. Wu, M.G. Jin, Z.C. Huang, M.S. Zheng, J.K. You, Z.G. Lin, Solid State Ionics, 167 (2004) 49-54.

[170] D.G. Kim, H. Kim, H.J. Sohn, T. Kang, Journal of Power Sources, 104 (2002) 221-225.

[171] D. Larcher, L.Y. Beaulieu, D.D. MacNeil, J.R. Dahn, Journal of The Electrochemical Society, 147 (2000) 1658-1662.

[172] C.F. Holmes, Journal of Power Sources, 97–98 (2001) 739-741.

[173] J. Yang, Y. Takeda, N. Imanishi, T. Ichikawa, O. Yamamoto, Journal of Power Sources, 79 (1999) 220-224.

[174] P. Poizot, S. Laruelle, S. Grugeon, L. Dupont, J.M. Tarascon, Nature, 407 (2000) 496-499.

[175] S. Grugeon, S. Laruelle, R. Herrera-Urbina, L. Dupont, P. Poizot, J.-M. Tarascon, Journal of The Electrochemical Society, 148 (2001) A285-A292.

[176] M.S. Whittingham, Chemical Reviews, 104 (2004) 4271-4302.

[177] C.R. Sides, C.R. Martin, Advanced Materials, 17 (2005) 125-128.

[178] M.E. Spahr, P. Stoschitzki-Bitterli, R. Nesper, O. Haas, P. Novak, Journal of The Electrochemical Society, 146 (1999) 2780-2783.

[179] S.T. Lutta, H. Dong, P.Y. Zavalij, M.S. Whittingham, Materials Research Bulletin, 40 (2005) 383-393.

[180] H.X. Li, L.F. Jiao, H.T. Yuan, M. Zhang, J. Guo, L.Q. Wang, M. Zhao, Y.M. Wang, Electrochemistry Communications, 8 (2006) 1693-1698.

[181] L. Benxia, X. Yang, R. Guoxin, J. Meng, X. Yi, Nanotechnology, 17 (2006) 2560.

[182] S. Shi, M. Cao, X. He, H. Xie, Crystal Growth & Design, 7 (2007) 1893-1897.

[183] A.-M. Cao, J.-S. Hu, H.-P. Liang, L.-J. Wan, Angewandte Chemie International Edition, 44 (2005) 4391-4395.

[184] C.J. Patrissi, C.R. Martin, Journal of The Electrochemical Society, 146 (1999) 3176-3180.

[185] X. Li, W. Li, H. Ma, J. Chen, Journal of The Electrochemical Society, 154 (2007) A39-A42.

[186] T. Zhai, H. Liu, H. Li, X. Fang, M. Liao, L. Li, H. Zhou, Y. Koide, Y. Bando, D. Golberg, Advanced Materials, 22 (2010) 2547-2552.

[187] F. Coustier, J. Hill, B.B. Owens, S. Passerini, W.H. Smyrl, Journal of The Electrochemical Society, 146 (1999) 1355-1360.

[188] L.Q. Mai, B. Hu, W. Chen, Y.Y. Qi, C.S. Lao, R.S. Yang, Y. Dai, Z.L. Wang, Advanced Materials, 19 (2007) 3712-3716.

[189] S.-H. Lee, Y.-H. Kim, R. Deshpande, P.A. Parilla, E. Whitney, D.T. Gillaspie, K.M. Jones, A.H. Mahan, S. Zhang, A.C. Dillon, Advanced Materials, 20 (2008) 3627-3632.

[190] N.A. Chernova, M. Roppolo, A.C. Dillon, M.S. Whittingham, Journal of Materials Chemistry, 19 (2009) 2526-2552.

[191] L. Zheng, Y. Xu, D. Jin, Y. Xie, Journal of Materials Chemistry, 20 (2010) 7135-7143.

[192] T. Brezesinski, J. Wang, S.H. Tolbert, B. Dunn, Nat Mater, 9 (2010) 146-151.

[193] E. Comini, L. Yubao, Y. Brando, G. Sberveglieri, Chemical Physics Letters, 407 (2005) 368-371.

[194] M. Sadakane, N. Watanabe, T. Katou, Y. Nodasaka, W. Ueda, Angewandte Chemie International Edition, 46 (2007) 1493-1496.

[195] H. Tsuji, Y. Koyasu, Journal of the American Chemical Society, 124 (2002) 5608-5609.

[196] X.W. Lou, H.C. Zeng, Chemistry of Materials, 14 (2002) 4781-4789.

[197] L. Zhou, L. Yang, P. Yuan, J. Zou, Y. Wu, C. Yu, The Journal of Physical Chemistry C, 114 (2010) 21868-21872.

[198] T. Tao, A.M. Glushenkov, C. Zhang, H. Zhang, D. Zhou, Z. Guo, H.K. Liu, Q. Chen, H. Hu, Y. Chen, Journal of Materials Chemistry, 21 (2011) 9350-9355.

[199] M.M. Rahman, J.-Z. Wang, N.H. Idris, Z. Chen, H. Liu, Electrochimica Acta, 56 (2010) 693-699.

[200] K.H. Seng, J. Liu, Z.P. Guo, Z.X. Chen, D. Jia, H.K. Liu, Electrochemistry Communications, 13 (2011) 383-386.

[201] L. Cui, J. Li, X.-g. Zhang, Materials Letters, 63 (2009) 683-686.

[202] Y. Kim, J.-S. Kim, M.-T. Thieu, H.-C. Dinh, I.-H. Yeo, W.I. Cho, S.-i. Mho, Bull. Korean Chem. Soc., 31 (2010) 3109.

[203] K. Kobayashi, K. Kosuge, S. Kachi, Materials Research Bulletin, 4 (1969) 95-106.

[204] C.L. Liao, M.T. Wu, J.H. Yen, I.C. Leu, K.Z. Fung, Journal of Alloys and Compounds, 414 (2006) 302-309.

[205] J. Yamaki, M. Makidera, T. Kawamura, M. Egashira, S. Okada, Journal of Power Sources, 153 (2006) 245-250.

[206] P. Liu, S.-H. Lee, Y. Yan, C. Edwin Tracy, J.A. Turner, Journal of Power Sources, 158 (2006) 659-662.

[207] Y. Wang, G. Cao, Advanced Materials, 20 (2008) 2251-2269.

[208] T. Ohzuku, A. Ueda, Solid State Ionics, 69 (1994) 201-211.

[209] M.S. Whittingham, Chem. Rev., 104 (2004) 4271-4302.

[210] J.R. Dahn, U. von Sacken, C.A. Michal, Solid State Ionics, 44 (1990) 87-97.

[211] A.R. Armstrong, P.G. Bruce, Nature, 381 (1996) 499-500.

[212] F. Capitaine, P. Gravereau, C. Delmas, Solid State Ionics, 89 (1996) 197-202.

[213] S.-Y. Chung, J.T. Bloking, Y.-M. Chiang, Nat Mater, 1 (2002) 123-128.

[214] K.S. Park, S.B. Schougaard, J.B. Goodenough, Advanced Materials, 19 (2007) 848-851.

[215] A.K. Padhi, K.S. Nanjundaswamy, J.B. Goodenough, Journal of The Electrochemical Society, 144 (1997) 1188-1194.

[216] C. Delacourt, L. Laffont, R. Bouchet, C. Wurm, J.-B. Leriche, M. Morcrette, J.-M. Tarascon, C. Masquelier, Journal of The Electrochemical Society, 152 (2005) A913-A921.

[217] C. Delacourt, P. Poizot, M. Morcrette, J.M. Tarascon, C. Masquelier, Chemistry of Materials, 16 (2003) 93-99.

[218] T. Shiratsuchi, S. Okada, T. Doi, J.-i. Yamaki, Electrochimica Acta, 54 (2009) 3145-3151.

[219] A.V. Murugan, T. Muraliganth, A. Manthiram, Journal of The Electrochemical Society, 156 (2009) A79-A83.

[220] R.C. Agrawal, G.P. Pandey, Journal of Physics D: Applied Physics, 41 (2008) 223001.

[221] M.J. Reddy, S. Sreepathi Rao, E. Laxminarsaiah, U.V. Subba Rao, Journal of Materials Science Letters, 14 (1995) 1129-1131.

[222] Y. Ito, K. Syakushiro, M. Hiratani, K. Miyauchi, T. Kudo, Solid State Ionics, 18–19, Part 1 (1986) 277-281.

[223] Z. Ogumi, Y. Uchimoto, Z. Takehara, Journal of The Electrochemical Society, 136 (1989) 625-630.

[224] A. Kumar, M. Deka, Nanofiber reinforced composite polymer electrolyte membranes, Intech, Croatia, 2010.

[225] I.S. Elashmawi, N.A. Hakeem, Polymer Engineering & Science, 48 (2008) 895-901.

[226] A.M.M. Ali, M.Z.A. Yahya, H. Bahron, R.H.Y. Subban, M.K. Harun, I. Atan, Materials Letters, 61 (2007) 2026-2029.

[227] Y.-J. Wang, D. Kim, Electrochimica Acta, 52 (2007) 3181-3189.

[228] M. Nookala, B. Kumar, S. Rodrigues, Journal of Power Sources, 111 (2002) 165-172.

[229] Z.-Y. Cui, Y.-Y. Xu, L.-P. Zhu, J.-Y. Wang, Z.-Y. Xi, B.-K. Zhu, Journal of Membrane Science, 325 (2008) 957-963.

[230] Y. Wang, X. Ma, Q. Zhang, N. Tian, Journal of Membrane Science, 349 (2010) 279-286.

[231] K.-H. Lee, J.-K. Park, W.-J. Kim, Electrochimica Acta, 45 (2000) 1301-1306.

[232] B. Scrosati, F. Croce, L. Persi, Journal of The Electrochemical Society, 147 (2000) 1718-1721.

[233] K.M. Kim, N.-G. Park, K.S. Ryu, S.H. Chang, Polymer, 43 (2002) 3951-3957.

[234] M. Watanabe, M. Itoh, K. Sanui, N. Ogata, Macromolecules, 20 (1987) 569-573.

[235] M. Mucha, Reactive and Functional Polymers, 38 (1998) 19-25.

[236] J.A. Galloway, K.J. Koester, B.J. Paasch, C.W. Macosko, Polymer, 45 (2004) 423-428.

[237] P.A.R.D. Jayathilaka, M.A.K.L. Dissanayake, I. Albinsson, B.E. Mellander, Solid State Ionics, 156 (2003) 179-195.

[238] A. Martinelli, M.A. Navarra, A. Matic, S. Panero, P. Jacobsson, L. Börjesson, B. Scrosati, Electrochimica Acta, 50 (2005) 3992-3997.

[239] S. Ramesh, A.K. Arof, Journal of Power Sources, 99 (2001) 41-47.

[240] N.-S. Choi, J.-K. Park, Electrochimica Acta, 46 (2001) 1453-1459.

[241] G. Girish Kumar, S. Sampath, Solid State Ionics, 176 (2005) 773-780.

[242] S. Ahmad, S. Ahmad, S.A. Agnihotry, Journal of Power Sources, 140 (2005) 151-156.

[243] H.-S. Kim, P. Periasamy, S.-I. Moon, Journal of Power Sources, 141 (2005) 293-297.

[244] D. Saikia, A. Kumar, European Polymer Journal, 41 (2005) 563-568.

[245] Z. Li, J. Wei, F. Shan, J. Yang, X. Wang, Journal of Polymer Science Part B: Polymer Physics, 46 (2008) 751-758.

[246] H.S. Choe, J. Giaccai, M. Alamgir, K.M. Abraham, Electrochimica Acta, 40 (1995) 2289-2293.

[247] M. Watanabe, M. Kanba, H. Matsuda, K. Tsunemi, K. Mizoguchi, E. Tsuchida, I. Shinohara, Die Makromolekulare Chemie, Rapid Communications, 2 (1981) 741-744.

[248] C.-Y. Chiang, Y.J. Shen, M.J. Reddy, P.P. Chu, Journal of Power Sources, 123 (2003) 222-229.

[249] T. Gozdz, J.M. Tarascon, C. Schmutz, P.C. Warren, O.S. Gebizlioglu, F.K. Shokoohi, in: Rechargeable lithium and lithium-ion (RCT) batteries symposium of the 186th electrochemical society meeting, Miami, Florida, 1994.

[250] J.M. Tarascon, M. Armand, Nature, 414 (2001) 359.

[251] Y. Liu, S. Gorgutsa, C. Santato, M. Skorobogatiy, Journal of The Electrochemical Society, 159 (2012) A349-A356.

[252] L. Hu, H. Wu, F. La Mantia, Y. Yang, Y. Cui, ACS Nano, 4 (2010) 5843-5848.

[253] K.H. Seng, J. Liu, Z.P. Guo, Z.X. Chen, D. Jia, H.K. Liu, Electrochem. Comm, 13 (2011) 383-386.

[254] L.-F. Cui, L. Hu, J.W. Choi, Y. Cui, ACS Nano, 4 (2010) 3671-3678.

[255] H. Gwon, H.-S. Kim, K.U. Lee, D.-H. Seo, Y.C. Park, Y.-S. Lee, B.T. Ahn, K. Kang, Energy Environ Sci, 4 (2011) 1277-1283.

[256] J.-Z. Wang, C. Zhong, S.-L. Chou, H.-K. Liu, Electrochem. Comm., 12 (2010) 1467-1470.

[257] B. Liu, J. Zhang, X. Wang, G. Chen, D. Chen, C. Zhou, G. Shen, Nano Letters, 12 (2012) 3005-3011.

[258] S.L. Chou, M. Ionescu, J.Z. Wang, B. Winton, H.K. Liu, Nanosci. Nanotechnol. Lett., 4 (2012) 169-172.

[259] A.L.M. Reddy, P.M. Ajayan, Small (Weinheim an der Bergstrasse, Germany), 7 (2011) 1709-1713.

[260] G. Zhou, D.-W. Wang, P.-X. Hou, W. Li, N. Li, C. Liu, F. Li, H.-M. Cheng, Journal of Materials Chemistry, 22 (2012) 17942-17946.

[261] X. Jia, Z. Chen, A. Suwarnasarn, L. Rice, X. Wang, H. Sohn, Q. Zhang, B.M. Wu, F. Wei, Y. Lu, Energy & Environmental Science, 5 (2012) 6845-6849.

[262] X. Jia, C. Yan, Z. Chen, R. Wang, Q. Zhang, L. Guo, F. Wei, Y. Lu, Chemical Communications, 47 (2011) 9669-9671.

[263] A. de la Hoz, A. Diaz-Ortiz, A. Moreno, Chemical Society Reviews, 34 (2005) 164-178.

[264] A. Shokuhfar, S.M. Kazemzadeh, M.R. Vaezi, A. Hassanjani-Roshan, Jornal of nano research, 11 (2010) 39-43.

[265] R. Gedye, F. Smith, K. Westaway, H. Ali, L. Baldisera, L. Laberge, J. Rousell, Tetrahedron Letters, 27 (1986) 279-282.

[266] S.H. Ng, D.I. dos Santos, S.Y. Chew, D. Wexler, J. Wang, S.X. Dou, H.K. Liu, Electrochem Comm, 9 (2007) 915-919.

[267] C. Feldmann, Advanced Functional Materials, 13 (2003) 101-107.

[268] H. Chong, in, 2004.

[269] H. Czichos, T. Saiyo, L. Smith, Handbook of materials measurements methods, Springer, 2006.

[270] J.R. Davis, Tensile testing, ASM International, 2004.

[271] W.A. De Heer, W.S. Bacsa, A. Chatelain, T. Gerfin, R. Humphrey-Baker, L. Forro, D. Ugarte, Science, 268 (1995) 845-847.

[272] Z. Li, G. Su, D. Gao, X. Wang, X. Li, Electrochim. Acta, 49 (2004) 4633-4639.

[273] M. Winter, R.J. Brodd, Chem. Rev., 104 (2004) 4245-4269.

[274] J.R. Dahn, T. Zheng, Y. Liu, J. Xue, Science, 270 (1995) 590.

[275] Y. Idota, T. Kubota, A. Matsufuji, Y. Maekawa, T. Miyasaka, Science, 276 (1997) 1395 - 1397.

[276] H. Li, Q. Wang, L. Shi, L. Chen, X. Huang, Chem. Mater., 14 (2002) 103.

[277] Da Deng, Min Gyu Kim, J.Y. Lee, J. Cho, Energy Environ. Sci., 2 (2009) 818–837.

[278] M. Winter, J.O. Besenhard, Electrochim. Acta, 45 (1999) 31.

[279] S. Han, B. Jang, T. Kim, S.M. Oh, T. Hyeon, Adv. Funct. Mater., 15 (2005) 1845.

[280] X.W. Lou, Y. Wang, C.L. Yuan, J.Y. Lee, L.A. Archer, Adv. Mater., 18 (2006) 2325.

[281] S.L. Chou, J.Z. Wang, H.K. Liu, S.X. Dou, Electrochem. Commun., 11 (2009) 242.

[282] Y. Wang, H.C. Zeng, J.Y. Lee, Adv. Mater. , 18 (2006) 645.

[283] Y. Wang, J.Y. Lee, H.C. Zeng, Chem. Mater., 17 (2005) 3899.

[284] N.C. Li, C.R. Martin, B. Scrosati, Electrochem. Solid-State Lett., 3 (2000) 316.

[285] M.S. Park, G.X. Wang, Y.M. Kang, D. Wexler, S.X. Dou, H.K. Liu, Angew. Chem. Int. Ed., 46 (2007) 750.

[286] Z. Ying, Q. Wan, H. Cao, Z.T. Song, S.L. Feng, Appl. Phys. Lett., 87 (2005) 113108.

[287] N. Zhao, G. Wang, Y. Huang, B. Wang, B. Yao, Y. Wu, Chemistry of Materials, 20 (2008) 2612-2614.

[288] Y.L. Zhang, Y. Liu, M.L. Liu, Chem. Mater., 18 (2006) 4643.

[289] Y. Wang, J.Y. Lee, J. Phys. Chem. B 108 (2004) 17832.

[290] L. Yuan, Z.P. Guo, K. Konstantinov, J.Z. Wang, H.K. Liu, Electrochim. Acta, 51 (2006) 3680.

[291] S.L. Chou, J.Z. Wang, C. Zhong, M.M. Rahman, H.K. Liu, S.X. Dou, Electrochimica Acta, 54 (2009) 7519-7524.

[292] Z. Hao-Xu, F. Chen, Z. Yong-Chao, J. Kai-Li, L. Qun-Qing, F. Shou-Shan, Advanced Materials, 21 (2009) 2299-2304.

[293] B.J. Landi, M.J. Ganter, C.D. Cress, R.A. DiLeo, R.P. Raffaelle, Energy Environ. Sci., 2 (2009) 638.

[294] R.S. Ruoff, D. Qian, W.K. Liu, Comptes Rendus Physique, 4 (2003) 993-1008.

[295] W.Q. Han, A. Zettl, Nano Lett. 3 (2003), p. 681., 3 (2003) 681.

[296] Y.B. Fu, R.B. Ma, Y. Shu, Z. Cao, X.H. Ma, Mater. Lett., 63 (2009) 1946.

[297] Q. Kuang, S.F. Li, Z.X. Xie, S.C. Lin, X.H. Zhang, S.Y. Xie, R.B. Huang, L.S. Zheng, Carbon, 44 (2006) 1166.

[298] G.M. An, X.R. Zhang, Z.J. Miao, S.D. Miao, K.L. Ding, Z.M. Liu, Nanotechnology, 18 (2007) 435707.

[299] G. Du, C. Zhong, P. Zhang, Z. Guo, Z. Chen, H. Liu, Electrochimica Acta 55 (2010) 2582.

[300] C. Xu, J. Sun, L. Gao, The Journal of Physical Chemistry C, 113 (2009) 20509-20513.

[301] N. Du, H. Zhang, B.D. Chen, X.Y. Ma, X.H. Huang, J.P. Tu, D.R. Yang, Materials Research Bulletin, 44 (2009) 211-215.

[302] C.-L. Zhu, M.-l. Zhang, Y.-J. Qiao, P. Gao, Y.-J. Chen, Materials Research Bulletin, 45 (2010) 437-441.

[303] Z.Y. Wang, G. Chen, D.G. Xia, J. Power Sources, 184 (2008) 432.

[304] N. Li, C.R. Martin, J. Electrochem. Soc., 148 (2001) A164.

[305] M. Wachtler, J.O. Besenhard, M. Winter, J. Power Sources, 94 (2001) 189-193.

[306] I.A. Courtney, W.R. McKinnon, J.R. Dahn, J. Electrochem. Soc. , 146 (1999) 59-68.

[307] Y. Wang, F. Su, J.Y. Lee, X.S. Zhao, Chemistry of Materials, 18 (2006) 1347-1353.

[308] J. Zhou, H. Song, X. Chen, L. Zhi, S. Yang, J. Huo, W. Yang, Chemistry of Materials, 21 (2009) 2935-2940.

[309] S. Laruelle, S. Grugeon, P. Poizot, M. Dollé, L. Dupont, J.-M. Tarascon, Journal of The Electrochemical Society, 149 (2002) A627-A634.

[310] M.S. Park, S.A. Needham, G.X. Wang, Y.M. Kang, J.S. Park, S.X. Dou, H.K. Liu, Chem. Mater., 19 (2007) 2406.

[311] R.A.M. Hikmet, J Power Sources, 92 (2001) 212-220.

[312] R.S. Morris, B.G. Dixon, T. Gennett, R. Raffaelle, M.J. Heben, J Power Sources, 138 (2004) 277-280.

[313] K.T. Nam, D.-W. Kim, P.J. Yoo, C.-Y. Chiang, N. Meethong, P.T. Hammond, Y.-M. Chiang, A.M. Belcher, Science, 312 (2006) 885-888.

[314] T. Suga, H. Konishi, H. Nishide, Chem Comm, (2007) 1730-1732.

[315] V.L. Pushparaj, M.M. Shaijumon, A. Kumar, S. Murugesan, L. Ci, R. Vajtai, R.J. Linhardt, O. Nalamasu, P.M. Ajayan, Proceed National Academy Sci, 104 (2007) 13574-13577.

[316] M.-F. Yu, B.S. Files, S. Arepalli, R.S. Ruoff, Phys Rev Lett, 84 (2000) 5552.

[317] F. Li, H.M. Cheng, S. Bai, G. Su, M.S. Dresselhaus, Appl Phys Lett, 77 (2000) 3161-3163.

[318] S.H. Ng, J. Wang, Z.P. Guo, J. Chen, G.X. Wang, H.K. Liu, Electrochim Acta, 51 (2005) 23-28.

[319] A. Hirsch, Angew Chemie Inter Edition, 41 (2002) 1853-1859.

[320] J. Zhao, A. Buldum, J. Han, J. Ping Lu, Phys Rev Lett, 85 (2000) 1706.

[321] B. Gao, A. Kleinhammes, X.P. Tang, C. Bower, L. Fleming, Y. Wu, O. Zhou, Chem Phy Lett, 307 (1999) 153-157.

[322] Da Deng, Min Gyu Kim, J.Y. Lee, J. Cho, Energy Environ Sci, 2 (2009) 818–837.

[323] I.A. Courtney, J.R. Dahn, J Electrochem Soc, 144 (1997) 2943-2948.

[324] T. Brousse, R. Retoux, U. Herterich, D.M. Schleich, J Electrochem Soc, 145 (1998) 1-4.

[325] Z. Wen, Q. Wang, Q. Zhang, J. Li, Adv Funct Mater, 17 (2007) 2772-2778.

[326] R. Demir-Cakan, Y.-S. Hu, M. Antonietti, J. Maier, M.-M. Titirici, Chem Mater, 20 (2008) 1227-1229.

[327] Y. Yu, C.H. Chen, Y. Shi, Adv Mater, 19 (2007) 993-997.

[328] L. Noerochim, J.-Z. Wang, S.-L. Chou, H.-J. Li, H.-K. Liu, Electrochim Acta, 56 (2010) 314-320.

[329] M.-S. Park, S.A. Needham, G.-X. Wang, Y.-M. Kang, J.-S. Park, S.-X. Dou, H.-K. Liu, Chem Mater, 19 (2007) 2406-2410.

[330] H.X. Zhang, C. Feng, Y.C. Zhai, K.L. Jiang, Q.Q. Li, S.S. Fan, Adv Mater, 21 (2009) 2299-2304.

[331] Z. Li, G. Su, D. Gao, X. Wang, X. Li, Electrochimica Acta, 49 (2004) 4633-4639.

[332] R. Fong, U. von Sacken, J.R. Dahn, J Electrochem Soc, 137 (1990) 2009-2013.

[333] I.A. Courtney, J.R. Dahn, Journal of The Electrochemical Society, 144 (1997) 2943-2948.

[334] L. Yuan, Z.P. Guo, K. Konstantinov, J.Z. Wang, H.K. Liu, Electrochim Acta, 51 (2006) 3680-3684.

[335] Y. Wang, F. Su, J.Y. Lee, X.S. Zhao, Chem Mater, 18 (2006) 1347-1353.

[336] Y.-J. Chen, C.-L. Zhu, X.-Y. Xue, X.-L. Shi, M.-S. Cao, Appl Phy Lett, 92 (2008) 223101-223103.

[337] J.Y. Eom, H.S. Kwon, J. Mater Res, 23 (2008) 2458.

[338] J. Graetz, C.C. Ahn, R. Yazami, B. Fultz, Electrochem Solid-State Lett, 6 (2003) A194-A197.

[339] J. Fan, P.S. Fedkiw, J Power Sources, 72 (1998) 165-173.

[340] S.H. Ng, J. Wang, K. Konstantinov, D. Wexler, J. Chen, H.K. Liu, J Electrochem Soc, 153 (2006) A787-A793.

[341] J. Cai, K. Cizek, B. Long, K. McAferty, C.G. Campbell, D.R. Allee, B.D. Vogt, J. La Belle, J. Wang, Sensors and Actuators B: Chem, 137 (2009) 379-385.

[342] S.H. Ng, J. Wang, Z.P. Guo, J. Chen, G.X. Wang, H.K. Liu, Electrochim. Acta, 51 (2005) 23-28.

[343] J. Chen, Y. Liu, A.I. Minett, C. Lynam, J. Wang, G.G. Wallace, Chem. Mater., 19 (2007) 3595-3597.

[344] J.-Z. Wang, S.-L. Chou, J. Chen, S.-Y. Chew, G.-X. Wang, K. Konstantinov, J. Wu, S.-X. Dou, H.K. Liu, Electrochem. Comm., 10 (2008) 1781-1784.

[345] C. Wang, D. Li, C.O. Too, G.G. Wallace, Chem. Mater., 21 (2009) 2604-2606.

[346] G. Dennler, S. Bereznev, D. Fichou, K. Holl, D. Ilic, R. Koeppe, M. Krebs, A. Labouret, C. Lungenschmied, A. Marchenko, D. Meissner, E. Mellikov, J. Méot, A. Meyer, T. Meyer, H. Neugebauer, A. Öpik, N.S. Sariciftci, S. Taillemite, T. Wöhrle, Solar Energy, 81 (2007) 947-957.

[347] J. Huang, X. Wang, J. Liu, X. Sun, L. Wang, X. He, Int. J. Electrochem. Sci., 6 (2011) 1709-1719.

[348] P. Novák, K. Müller, K.S.V. Santhanam, O. Haas, Chem. Rev., 97 (1997) 207-282.

[349] T.F. Otero, I. Cantero, J. Power Sources, 81-82 (1999) 838-841.

[350] J.-Z. Wang, S.-L. Chou, H. Liu, G.X. Wang, C. Zhong, S. Yen Chew, H. Kun Liu, Mater. Lett., 63 (2009) 2352-2354.

[351] A. Du Pasquier, F. Orsini, A.S. Gozdz, J.M. Tarascon, J. Power Sources, 81-82 (1999) 607-611.

[352] J. Wang, J. Chen, K. Konstantinov, L. Zhao, S.H. Ng, G.X. Wang, Z.P. Guo, H.K. Liu, Electrochim. Acta, 51 (2006) 4634-4638.

[353] S.Y. Chew, C. Feng, S.H. Ng, J. Wang, Z. Guo, H. Liu, J. Electrochem. Soc., 154 (2007) A633-A637.

[354] L. Yuan, J. Wang, S.Y. Chew, J. Chen, Z.P. Guo, L. Zhao, K. Konstantinov, H.K. Liu, J. Power Sources, 174 (2007) 1183-1187.

[355] S.Y. Chew, Z.P. Guo, J.Z. Wang, J. Chen, P. Munroe, S.H. Ng, L. Zhao, H.K. Liu, Electrochem. Comm., 9 (2007) 941-946.

[356] A. Dobley, K. Ngala, S. Yang, P.Y. Zavalij, M.S. Whittingham, Chem. Mater., 13 (2001) 4382-4386.

[357] S.-L. Chou, J.-Z. Wang, J.-Z. Sun, D. Wexler, M. Forsyth, H.-K. Liu, D.R. MacFarlane, S.-X. Dou, Chem. Mater., 20 (2008) 7044-7051.

[358] T. Zhai, H. Liu, H. Li, X. Fang, M. Liao, L. Li, H. Zhou, Y. Koide, Y. Bando, D. Golberg, Adv. Mater., 22 (2010) 2547-2552.

[359] G. Li, S. Pang, L. Jiang, Z. Guo, Z. Zhang, J. Phys. Chem. B, 110 (2006) 9383-9386.

[360] V. Petkov, P.N. Trikalitis, E.S. Bozin, S.J.L. Billinge, T. Vogt, M.G. Kanatzidis, J. Am. Chem. Soc., 124 (2002) 10157-10162.

[361] B. Alonso, J. Livage, J. Solid State Chem., 148 (1999) 16-19.

[362] C.J. Fontenot, J.W. Wiench, M. Pruski, G.L. Schrader, J. Phys. Chem. B, 104 (2000) 11622-11631.

[363] H.S. Kim, D.H. Park, Y.B. Lee, D.-C. Kim, H.-J. Kim, J. Kim, J. Joo, Synth. Metals, 157 (2007) 910-913.

[364] D.W. Murphy, P.A. Christian, F.J. DiSalvo, J.V. Waszczak, Inorganic Chemistry, 18 (1979) 2800-2803.

[365] Cuentas-Gallegos, A. Karina, Gómez-Romero, Pedro, J. Power Sources, 161 (2006) 580-586.

[366] I. Boyano, M. Bengoechea, I. de Meatza, O. Miguel, I. Cantero, E. Ochoteco, J. Rodríguez, M. Lira-Cantú, P. Gómez-Romero, Journal of Power Sources, 166 (2007) 471-477.

[367] C. Delmas, S. Brèthes, M. Ménétrier, J. Power Sources, 34 (1991) 113-118.

[368] K. West, B. Zachau-Christiansen, T. Jacobsen, S. Skaarup, Sol. State Ionics, 76 (1995) 15-21.

[369] Y. Kim, J.-S. Kim, M.-T. Thieu, H.-C. Dinh, I.-H. Yeo, W.I. Cho, S.-i. Mho, Bull Korean Chem. Soc., 31 (2010) 3109.

[370] S.-L. Chou, J.-Z. Wang, J.-Z. Sun, D. Wexler, M. Forsyth, H.-K. Liu, D.R. MacFarlane, S.-X. Dou, Chemistry of Materials, 20 (2008) 7044-7051.

[371] J.-Z. Wang, S.-L. Chou, H. Liu, G.X. Wang, C. Zhong, S. Yen Chew, H. Kun Liu, Materials Letters, 63 (2009) 2352-2354.

[372] S. Park, R.S. Ruoff, Nature nanotechnology, 4 (2009) 217-224.

[373] J. Liang, Y. Xu, D. Sui, L. Zhang, Y. Huang, Y. Ma, F. Li, Y. Chen, The Journal of Physical Chemistry C, 114 (2010) 17465-17471.

[374] G. Zhou, D.-W. Wang, F. Li, L. Zhang, N. Li, Z.-S. Wu, L. Wen, G.Q. Lu, H.-M. Cheng, Chemistry of Materials, 22 (2010) 5306-5313.

[375] J.-Z. Wang, C. Zhong, D. Wexler, N.H. Idris, Z.-X. Wang, L.-Q. Chen, H.-K. Liu, Chemistry – A European Journal, 17 (2011) 661-667.

[376] I.R.M. Kottegoda, N.H. Idris, L. Lu, J.-Z. Wang, H.-K. Liu, Electrochimica Acta, 56 (2011) 5815-5822.

[377] Y.J. Mai, S.J. Shi, D. Zhang, Y. Lu, C.D. Gu, J.P. Tu, Journal of Power Sources, 204 (2012) 155-161.

[378] X. Wang, X. Zhou, K. Yao, J. Zhang, Z. Liu, Carbon, 49 (2011) 133-139.

[379] C. Zhu, Y. Fang, D. Wen, S. Dong, Journal of Materials Chemistry, 21 (2011) 16911-16917.

[380] C. Zhong, J. Wang, Z. Chen, H. Liu, The Journal of Physical Chemistry C, 115 (2011) 25115-25120.

[381] Y. Shi, S.-L. Chou, J.-Z. Wang, D. Wexler, H.-J. Li, H.-K. Liu, Y. Wu, Journal of Materials Chemistry, (2012).

[382] X. Zhou, F. Wang, Y. Zhu, Z. Liu, Journal of Materials Chemistry, 21 (2011) 3353-3358.

[383] R.-Q. Song, A.-W. Xu, B. Deng, Y.-P. Fang, The Journal of Physical Chemistry B, 109 (2005) 22758-22766.

[384] L. Zheng, Y. Xu, D. Jin, Y. Xie, Chemistry of Materials, 21 (2009) 5681-5690.

[385] T. Xia, Q. Li, X. Liu, J. Meng, X. Cao, The Journal of Physical Chemistry B, 110 (2006) 2006-2012.

[386] P. Zhang, S. Yin, T. Sato, Applied Catalysis B: Environmental, 89 (2009) 118-122.

[387] J.-H. Lee, C.-K. Kim, S. Katoh, R. Murakami, Journal of Alloys and Compounds, 325 (2001) 276-280.

[388] A. Phuruangrat, D.J. Ham, S. Thongtem, J.S. Lee, Electrochemistry Communications, 11 (2009) 1740-1743.

[389] D.C. Marcano, D.V. Kosynkin, J.M. Berlin, A. Sinitskii, Z. Sun, A. Slesarev, L.B. Alemany, W. Lu, J.M. Tour, ACS Nano, 4 (2010) 4806-4814.

[390] C.V. Subba Reddy, Z.R. Deng, Q.Y. Zhu, Y. Dai, J. Zhou, W. Chen, S.I. Mho, Applied Physics A: Materials Science & Processing, 89 (2007) 995-999.

[391] A.C. Ferrari, J. Robertson, Physical Review B, 61 (2000) 14095-14107.

[392] X. Yang, H. Ding, D. Zhang, X. Yan, C. Lu, J. Qin, R. Zhang, H. Tang, H. Song, Crystal Research and Technology, 46 (2011) 1195-1201.

[393] S. Park, J. An, J.R. Potts, A. Velamakanni, S. Murali, R.S. Ruoff, Carbon, 49 (2011) 3019-3023.

[394] Y.L. Xie, F.C. Cheong, Y.W. Zhu, B. Varghese, R. Tamang, A.A. Bettiol, C.H. Sow, The Journal of Physical Chemistry C, 114 (2009) 120-124.

[395] W. Li, F. Cheng, Z. Tao, J. Chen, The Journal of Physical Chemistry B, 110 (2005) 119-124.

[396] J.S. Chen, Y.L. Cheah, S. Madhavi, X.W. Lou, The Journal of Physical Chemistry C, 114 (2010) 8675-8678.

[397] G.T.-K. Fey, C.-Z. Lu, T.P. Kumar, Journal of Power Sources, 115 (2003) 332-345.

Appendix A: Publication list during PhD study

[1] **Noerochim L**, Wang J-Z, Chou S-L, Li H-J, Liu H-K. SnO_2-coated multiwall carbon nanotube composite anode materials for rechargeable lithium-ion batteries. Electrochimica Acta. 2010;56(1):314-320. (IF:3.83)

[2] **Noerochim L**, Wang J-Z, Chou S-L, Wexler D, Liu H-K. Free-standing single-walled carbon nanotube/SnO_2 anode paper for flexible lithium-ion batteries. Carbon. 2012;50(3):1289-1297.(IF:5.37)

[3] **Noerochim L**, Wang J-Z, Wexler D, Rahman MM, Chen J, Liu H-K. Impact of mechanical bending on the electrochemical performance of bendable lithium batteries with paper-like free-standing V_2O_5-polypyrrole cathodes. Journal of Materials Chemistry. 2012;22(22):11159-11165. (IF:5.96)

[4] **Noerochim L**, Wang J-Z, Wexler D, Chao Z, Liu H-K. Rapid synthesis of free-standing MoO3/Graphene films by the microwave hydrothermal method as cathode for bendable lithium batteries. Journal of Power Sources. 2013;228(0):198-205. (IF:4.95)

Appendix B: Received awards during PhD study

1. Matching Scholarship and International Postgraduate Tuition Award (2009-2012) for pursuing a PhD through the Australian Research Council (ARC) Centre of Excellence for Electromaterials Science, University of Wollongong, Australia
2. Excellent research top-up award 2012, ISEM, University of Wollongong, Australia
3. ISEM merit award 2012, University of Wollongong, Australia